Solid–Solid Phase Transitions in Colloidal Matter

by

Xiyu Chrisy Du

A dissertation submitted in partial fulfillment
of the requirements for the degree of
Doctor of Philosophy
(Physics)
in The University of Michigan
2018

Doctoral Committee:

Professor Sharon C. Glotzer, Co-Chair
Professor Greg van Anders, Co-Chair
Professor Nicholas A. Kotov
Professor Xiaoming Mao
Professor Robert M. Ziff

Xiyu Chrisy Du

xiyudu@umich.edu

ORCID iD: 0000-0002-1881-7102

DEDICATION

To my parents, who have supported me immensely to go study in a different country.

ACKNOWLEDGEMENTS

I would like to express gratitude to everyone who has supported me for the past six years. Without you, this dissertation would not be possible.

I would like to thank my two advisors Sharon C. Glotzer and Greg van Anders first and foremost. Sharon welcomed me into her lab when I doubted whether I should keep doing research. She has provided me with immense support, both academically and emotionally in the past four years. Without her, I would not be where I am now. Greg had provided me much day-to-day support and taught me much about the art of formulating a research question and scientific writing.

I would like to thank Richmond S. Newman, who was a senior graduate student in the lab when I joined. He had provided me much support and time during the start of my project. Without him, I could not have gotten preliminary result as fast.

I would like to thank Karen Coulter, who is the project manager in the lab. Not only she has solved so many different logistical problems for me as an international student, she has also provided me with wonderful advice about research and emotional support.

I would like to thank everyone who is or has been a member of the Glotzer Group, especially Julia Dshemuchadse, Joshua Anderson, Matthew Spellings, Erin Teich, Rose Cersonsky, and Eric Harper. Julia has been a wonderful friend to me ever since she joined the lab. She has helped me immensely with every step of my graduate career, especially during the postdoc application process. Josh and Matthew have

TABLE OF CONTENTS

LIST OF FIGURES

ABSTRACT

Phase transitions are ubiquitous in nature, and observed throughout everyday life from the melting of ice to the magnetization of iron. In particular, solid–solid phase transitions are important in many areas such as metallurgy, geosciences, and the design of reconfigurable materials. Following the recent initiative of using nano building blocks to design next generation materials, we answer fundamental questions about solid–solid phase transitions in colloidal matter and guide the design of materials that can change phase. Using the "Digital Alchemy" framework, we extend thermodynamic ensembles to include particle shape as a thermodynamic variable. This framework enables us to study the effect of altering particle shape in solid–solid phase transitions.

We first study the thermodynamic order of two different solid–solid phase transitions (face-centered cubic (FCC)↔body-centered cubic (BCC) and BCC↔simple cubic (SC)) in hard-particle systems upon an instantaneous change in particle shape. By calculating the Landau free energy, we are able to determine the thermodynamic order of these two phase transitions. We find FCC↔BCC is first order while BCC↔SC is second order. This work is followed up by a more detailed investigation of the FCC↔BCC transition to explore whether it can be second order.

We next study the design of pressure-induced solid–solid phase transitions. Here, we incorporate varying particle shape as a part of the Monte Carlo process to find the optimal shape for a given phase transition. We successfully designed pressure driven FCC→BCC and BCC→SC transitions using three different particle shape constraints.

We also study the kinetic transition pathway between solid phases. Our results show that there are similarities of the pathways of an entropic system and an atomistic system. This demonstrates that we can use entropic systems as a toy model to understand better how the transformations happen in an atomistic system.

Results from this dissertation give insight into the fundamental nature of the most common, yet poorly understood phase transitions in nature, and provide new minimal models for understanding solid–solid transitions in atomic systems. Our findings also provide guidance for the next generation of materials design.

CHAPTER I

Introduction

1.1 Solid–Solid Transitions in Nature

Phase transitions are ubiquitous in nature and are relevant for various phenomena, from Early Universe Physics [32, 47, 78] to a pack of coffee suddenly becoming soft once one breaks the vacuum seal. In all of those cases, a system with a large number of particles suddenly qualitatively changes its macroscopic behavior as some external parameter is smoothly adjusted. Liquid–solid and liquid–gas transitions as well as magnetic transitions [30] have been studied for a long time and are well understood. Solid–solid phase transitions are of particular importance in metallurgy [63] for they determine the properties of industrial materials [77], and in geophysics due to internal stress in Earth's crust [40, 9]. The second half of the 20th century showed that many phase transitions [37] found in different areas of physics can be described with relatively few classes and methods. However, detailed procedures for the study of solid–solid transitions have eluded us. For example, Bain [6] proposed one possible pathway of FCC$\leftrightarrow$BCC transition in 1924; however, it is by far not the only pathway for this transition to happen [72, 71]. Even till today, researchers are still proposing new or combined pathways for this transition [25], which is of importance in metallurgy, as it is the transition between two different kind of iron phases.

Most solid–solid phase transitions occur under extreme conditions (*i.e.* extreme temperature, timescale, pressure or length-scale), which makes this class of transitions very hard to study. However, recent developments in colloidal materials have provided us very good model systems to study such transitions both experimentally and theoretically [11].

1.2 Complexity of Self-Assembly in Colloidal Matter

In colloidal systems, particles are typically hundreds of nanometers to one or two microns in diameter [48]. At this length scale, there is no need to consider quantum effects of particle-particle interactions present at the atomic level. The particles–suspended in solution–exhibit Brownian motion and, yet, like atoms, obey the law of statistical thermodynamics. Moreover, with the current advances of colloidal materials synthesis, we can easily tailor the interactions of colloidal particles along different alchemical axes [29, 84], where one of the axes is to make particles with different polyhedral geometries [95, 66, 93, 34]. By using Colloidal Metal-Organic Frameworks [76], researchers are able to control the facet growth to synthesize particles of different polyhedral shape, such as octahedra [83], rhombic dodecahedra [12], truncated cubes [90], truncated rhombic dodecahedra [60], etc. These particles can be modeled using hard-particle interaction, one of the simplest interactions, which simply prohibits particle overlaps. Contrary to the intuitive simplicity, such interaction still gives rise to nontrivial phenomena [17, 13, 56, 1, 66, 14, 34, 2, 27, 53, 84]. For example, with proper density, tetrahedra can self assemble into a dodecagonal quasicrystal [33]. Many other common structures in atomistic systems can also find their analogues in hard particle systems, such as one of the high pressure lithium phase (truncated tetrahedron) [13], diamond (truncated tetrahedron) [13], β-Manganese

(dodecahedron) [14], γ-Brass (truncated dodecahedron) [14], and β-Tungsten (para-bidiminished rhombicosidodecahedron) [14] structure.

1.3   Solid–Solid Phase Transitions in Colloidal Matter

Pioneering work has been done by both simulation and experiments regarding solid–solid phase transitions in colloidal matter. There are multiple experiments that have observed the FCC↔BCC phase transition occur in real time and detailed work has been done to study the multiple pathways of this transition in a soft sphere system [92, 95, 61, 64, 54, 67, 50]. Simulation work [61] has been done on the same system aiming to understand why certain pathways are preferred compared to others. Moreover, interaction shifting via DNA programming has been used to construct colloidal solid–solid transitions, including showing that a single solid mother phase can be reprogrammed to yield multiple daughter phases through diffusionless transitions [10, 96].

In all the works mentioned above, the phase transitions are driven by traditional thermodynamic variables such as temperature and pressure. Here, I use a recently developed statistical thermodynamic ("alchemical") framework [86] that regards particle shape as a thermodynamic variable and study solid–solid phase transitions that are driven by changing particle shape. Since there is no interaction in my system, I am able to single out the contribution of entropy in my transitions. Using computational methods such as hard-particle Monte Carlo and umbrella sampling (Chapter II), I study the thermodynamic (Chapter III, Chapter IV) and kinetic properties (Chapter V) of this class of solid–solid phase transitions, and then invert the problem to design a solid–solid phase transition on demand (Chapter VI).

CHAPTER II

Methods

2.1 Hard Particle Monte Carlo

We can use the hard particle assumption to model the colloidal particles of interest in this dissertation. For this model, we have pair-wise interactions between particles i and j where

$$(2.1) \qquad U(i,j) = \begin{cases} 0 & \text{particles } i, j \text{ have no overlap} \\ \infty & \text{particles } i, j \text{ have an overlap.} \end{cases}$$

This model accurately represents a purely entropic system, where we can understand how entropy plays a role in phase transitions.

The algorithm to perform Hard Particle Monte Carlo is straightforward due to the simplicity of the hard particle potential. Using the traditional Metropolis criterion [52], where the probability of accepting the next step is determined by the Boltzmann factor $\exp(-\Delta U / k_{\mathrm{B}} T)$, we can derive the accept/reject criteria for Hard Particle Monte Carlo given that the system energy is either 0 or ∞ given how many overlaps there are. With $\Delta U = 0$ always, we always accept a trial move unless there is any overlap.

2.2   Order Parameters

Order parameters are used to describe the mesoscopic states of a system. It can be as simple as the density or volume of a system if you want to tell ice and water apart or it can be the magnetic moment if you want to know whether a magnet is above or below the Curie temperature. In my case, I want to have a numerical measure of the crystal structure of my system and the order parameter needs to satisfy a set of constraints:

1. It can be calculated based on particle positions.

2. It can distinguish between various different crystal structures.

3. It is not very sensitive to thermal noise.

2.2.1   Local Bond Order Parameters

Most commonly, people have been using the local bond order parameter Steinhardt *et. al.* [79] developed to detect the cubic crystal structures, FCC, BCC, and SC. The basic idea for this order parameter is that it associates a set of spherical harmonics Y_{lm} with every fictitious bond connecting one particle to its nearest neighbors. Here a "bond" refers to a vector from a particle to a neighboring particle. The mathematical formalism of this order parameter is as follows.

$$(2.2) \qquad\qquad Q_{lm}(\vec{r}) \equiv Y_{lm}(\theta(\vec{r}), \phi(\vec{r})),$$

where $\vec{r}$ is the vector that indicates the bond and $Y_{lm}(\theta, \phi)$ are spherical harmonics. The spherical harmonics function is defined as

$$(2.3) \qquad\qquad Y_{lm}(\theta, \phi) = \sqrt{\frac{2l+1}{4\pi} \frac{(l-m)!}{(l+m)!}} P_l^m(\cos\theta) e^{im\phi},$$

where

$$(2.4) \qquad\qquad P_l^m(x) = \frac{(-1)^m}{2^l l!} (1-x^2)^{m/2} \frac{d^{l+m}}{dx^{l+m}} (x^2-1)^l.$$

To determine the local environment, we need to consider the average value

$$(2.5) \qquad \overline{Q}_{lm} \equiv \langle Q_{lm}(\vec{r}) \rangle \qquad \text{nearest neighbor average}$$

over all nearest neighbors within some r_{cut}, which is often the cutoff radius of the first neighbor shell. Since $\overline{Q}_{lm}$ for a given l can change drastically when changing the orientation, one should use the rotationally invariant combination, which is

$$(2.6) \qquad Q_l \equiv \left[\frac{4\pi}{2l+1} \sum_{m=-1}^{l} |\overline{Q}_{lm}|^2 \right]^{1/2}.$$

Since Q_l is heavily built on spherical harmonics, it is a measure of symmetry of the system. This means that Q_l is very efficient at distinguishing any crystal structures from the liquid phase or two different crystal structures that have vastly different symmetry groups. However, for structures such as FCC, BCC, and SC, which have similar Q_l values, it is problematic to use this definition of Q_l as our order parameter. Fig. 2.1 shows the Q_4 distribution for three different structures: BCC, hexagonally close-packed (HCP), and FCC at the same density ($\eta = 0.55$) with thermal noise applied. In Fig. 2.1A and B, a hard radial distance cutoff is applied, while in Fig. 2.1C and D, a fixed number of nearest neighbors is considered. In Fig. 2.1A and C each structure is applied with a structural specific distance cutoff or number of nearest neighbors, while Fig. 2.1B and D, the same criterion is applied to all three structures, which is more realistic during a simulation. We can see that while Fig. 2.1A and C do show some separation between the three structures, Fig. 2.1B and D completely fails to distinguish them.

2.2.2 Averaged Local Bond Order Parameter

Based on the original Local Bond Order Parameter, Lechner and Dellago [44] have introduced a second neighbor averaged Q_l that reduces noise, and can successfully

distinguish between FCC, BCC, and SC. In this modified version, after $\overline{Q}_{lm}$ is calculated, the values are again averaged over all particles and their neighbors, which gives

$$(2.7) \qquad \mathrm{Ave}\overline{Q}_{lm} \equiv \langle \overline{Q}_{lm}(\vec{r}) \rangle. \qquad \text{nearest neighbor+1 average}$$

The final average Q_l has the form

$$(2.8) \qquad \overline{Q}_l \equiv \left[\frac{4\pi}{2l+1} \sum_{m=-l}^{l} |\mathrm{Ave}\overline{Q}_{lm}|^2 \right]^{1/2}.$$

In Fig. 2.2, it shows the $\overline{Q}_4$ distribution for three different structures: BCC, HCP, and FCC at the same density ($\eta = 0.55$) with some thermal noise. In Fig. 2.2A and B, a hard radial distance cutoff is applied, while in Fig. 2.2C and D, a fixed number of nearest neighbors is considered. In Fig. 2.1A and C each structure is applied with a structural specific distance cutoff or number of nearest neighbors, while Fig. 2.2B and D, the same criterion is applied to all three structures, which is more realistic during a simulation. We can see that Fig. 2.2A and C show very nice separation between the three structures compare to the original local bond order parameter Q_4. Moreover, by using a single criteria for either the radial cutoff or number of nearest neighbors, $\overline{Q}_4$ still sufficiently distinguishes these three structures.

After these parameter tests, we use the $\overline{Q}_4$ order parameter with fixed number of nearest neighbors as our order parameter to distinguish all the relevant phases in simulations in this dissertation. This order parameter shows enough robustness regards to thermal noise.

2.3 Umbrella Sampling

To calculate the free energy of a system along some order parameter coordinate, the most straightforward method is to measure the probability distribution of the

system along this order parameter coordinate. Once we have the probability distribution, we can calculate the free energy using

$$(2.9) \qquad\qquad A = -k_\mathrm{B} T \log Z,$$

where Z denotes the partition function of the system, which can be calculated from the probability distribution. However, this method assumes ergodicity across the whole order parameter space, which indicates a relative flat free energy landscape. Generally, systems of interest do not have such free energy landscapes and we will need more advanced methods to sample the order parameter coordinate.

The basic idea of umbrella sampling is to divide the order parameter space into different state points (windows) and apply a biased potential to the system that favors the target state point. After the system is pushed to the target state point, we can start collecting statistics to obtain the biased distribution near the target state point. Using the biased distribution with the known bias, we can recover the unbiased free energy. Following [82], we discuss the mathematical formalism of umbrella sampling. In the following derivation, superscript "b" denotes biased quantities, while superscript "u" denotes unbiased quantities, and $w_i(\xi)$ is the bias potential of window i, which depends solely on the chosen order parameter ξ. The total internal energy of the system in window i will then be

$$(2.10) \qquad\qquad E^b(r) = E^u(r) + w_i(\xi).$$

To obtain the unbiased free energy $A_i(\xi)$, we need the unbiased distribution along the order parameter ξ, which is

$$(2.11) \qquad\qquad P_i^u(\xi) = \frac{\int \exp[-\beta E^u(r)]\delta[\xi'(r) - \xi]d^N r}{\int \exp[-\beta E^u(r)]d^N r}.$$

Here $\beta = 1/(k_\mathrm{B}T)$, where k_B is the Boltzmann constant and T is temperature. During an umbrella sampling simulation, we obtains the biased distribution P_i^b as a

function of ξ. Assuming the system is ergodic, we have

$$(2.12) \qquad P_i^b(\xi) = \frac{\int \exp\{-\beta[E^u(r) + w_i(\xi)]\}\delta[\xi'(r) - \xi]d^N r}{\int \exp\{-\beta[E^u(r) + w_i(\xi)]\}d^N r}.$$

Since the bias potential only depends on ξ and the integration in the numerator is over all degrees of freedom but ξ, we have

$$(2.13) \qquad P_i^b(\xi) = \exp[-\beta w_i(\xi)] \times \frac{\int \exp[-\beta E^u(r)]\delta[\xi'(r) - \xi]d^N r}{\int \exp\{-\beta[E^u(r) + w_i(\xi'(r))]\}d^N r}$$

Combining Eq. 2.11 and Eq. 2.13, we get

$$
\begin{aligned}
P_i^u(\xi) &= P_i^b(\xi) \exp[\beta w_i(\xi)] \times \frac{\int \exp\{-\beta[E^u(r) + w_i(\xi(r))]\}d^N r}{\int \exp[-\beta E^u(r)]d^N r} \\
&= P_i^b(\xi) \exp[\beta w_i(\xi)] \times \frac{\int \exp[-\beta E^u(r)] \exp\{-\beta w_i[\xi(r)]\}d^N r}{\int \exp[-\beta E^u(r)]d^N r} \\
(2.14) \qquad &= P_i^b(\xi) \exp[\beta w_i(\xi)]\langle \exp[-\beta w_i(\xi)]\rangle.
\end{aligned}
$$

Using the definition of free energy, we obtain

$$(2.15) \qquad A_i(\xi) = -\left(\frac{1}{\beta}\right) \ln P_i^b(\xi) - w_i(\xi) + F_i.$$

F_i does not depend on ξ and has the following form:

$$(2.16) \qquad F_i = -\left(\frac{1}{\beta}\right) \ln\langle \exp[-\beta w_i(\xi)]\rangle.$$

This result is exact up to numerical sampling errors, which depends on the choice of the bias potential $w_i(\xi)$. In our studies, we chose a standard harmonic potential:

$$(2.17) \qquad w_i(\xi) = \frac{1}{2}k(\xi - \xi^i)^2.$$

We used $\overline{Q}_4$ to be our order parameter ξ and chose a range of $\overline{Q}_4 \in [0.055, 0.179]$, which evenly divides into 32 windows.

2.4 Digital Alchemy for Two Systems

Digital Alchemy [86] is a thermodynamic framework where we can extend the traditional thermodynamic ensemble to include alchemical variables. For our purpose, we will focus on the inclusion of particle shape. Following the derivation in [86], we can write the generalized partition function to include particle shape as the following:

$$(2.18) \qquad Z = \sum e^{-\beta(H - \sum_i \mu_i N \alpha_i - \lambda \Lambda)}.$$

Here, β is the inverse temperature, μ_i are so-called alchemical potentials that are thermodynamically conjugate to the alchemical parameters α_i, which in this case describe particle shape, N is the number of particles in the system, Λ is the potential energy function for an Einstein crystal of the target structure, λ is the spring constant of the Einstein crystal, and the sum is taken over particle coordinates and orientations and over the space of particle shapes. The term $\lambda \Lambda$ provides a design constraint, and can be neglected if no target phase is sought.

For our purpose, we want to extend this framework for two systems. Following the same construct, we can define two systems with Hamiltonians H_1 and H_2,

$$(2.19) \qquad H_1(\{\alpha_i\}) = \frac{p_1{}^2}{2m_1} + \frac{1}{2}L_1^T I_{1\{\alpha_i\}}^{-1} L_1 + U_{1\{\alpha_i\}}(q_1, Q_1),$$

$$(2.20) \qquad H_2(\{\alpha_i\}) = \frac{p_2{}^2}{2m_2} + \frac{1}{2}L_2^T I_{2\{\alpha_i\}}^{-1} L_2 + U_{2\{\alpha_i\}}(q_2, Q_2),$$

where p_1 and p_2 are momenta, L_1 and L_2 are angular momenta, I_1 and I_2 are moment of inertia tensors, and U_1 and U_2 are the interaction potentials that depend on the particle positions q_1 and q_2 and orientations Q_1 and Q_2 in the two systems, respectively. We have suppressed particle indices in Eq. 2.19 and Eq. 2.20.

Using the same assumptions as in the original study [86], we can write down the

Shannon/Jaynes entropy [74, 36] for the coupled system as

$$S = - \sum_{\sigma_1,\sigma_2} \left[\pi_{\sigma_1,\sigma_2} \ln(\pi_{\sigma_1,\sigma_2}) - \beta_1 \left(\sum \pi_{\sigma_1,\sigma_2} H_1(\pi_{\sigma_1}) - E_1 \right) \right.$$

$$- \beta_2 \left(\sum \pi_{\sigma_1,\sigma_2} H_2(\pi_{\sigma_2}) - E_2 \right) + (\beta_1 + \beta_2) \sum_i \mu_i (N_1 + N_2)$$

$$(2.21) \qquad \left. \sum \left(\pi_{\sigma_1,\sigma_2} \alpha_i(\sigma_1, \sigma_2) - \langle \alpha_i \rangle \right) \right],$$

where we have set $k_{\mathrm{B}} = 1$, π_{σ_1,σ_2} is the probability of finding states σ_1 and σ_2 in system 1 and system 2, respectively, β_1, β_2, and μ_i are Lagrange multipliers enforcing the thermal averages, and N_1 and N_2 are the numbers of particles in both systems, respectively. To determine the partition function, we maximize Eq. 2.21 with respect to π_{σ_1,σ_2}. This gives us

$$(2.22) \qquad \pi_{\sigma_1,\sigma_2} = \frac{1}{\mathcal{Z}} e^{-\beta_1 H_1(\sigma_1) - \beta_2 H_2(\sigma_2) + (\beta_1+\beta_2) \sum_i \mu_i (N_1+N_2)\alpha_i}.$$

Fixing the normalization $\sum_{\sigma_1,\sigma_2} \pi_{\sigma_1,\sigma_2} = 1$ yields the coupled partition function

$$(2.23) \qquad \mathcal{Z} = \sum_{\sigma_1,\sigma_2} e^{-\beta_1 H_1(\sigma_1) - \beta_2 H_2(\sigma_2) + (\beta_1+\beta_2) \sum_i \mu_i (N_1+N_2)\alpha_i}.$$
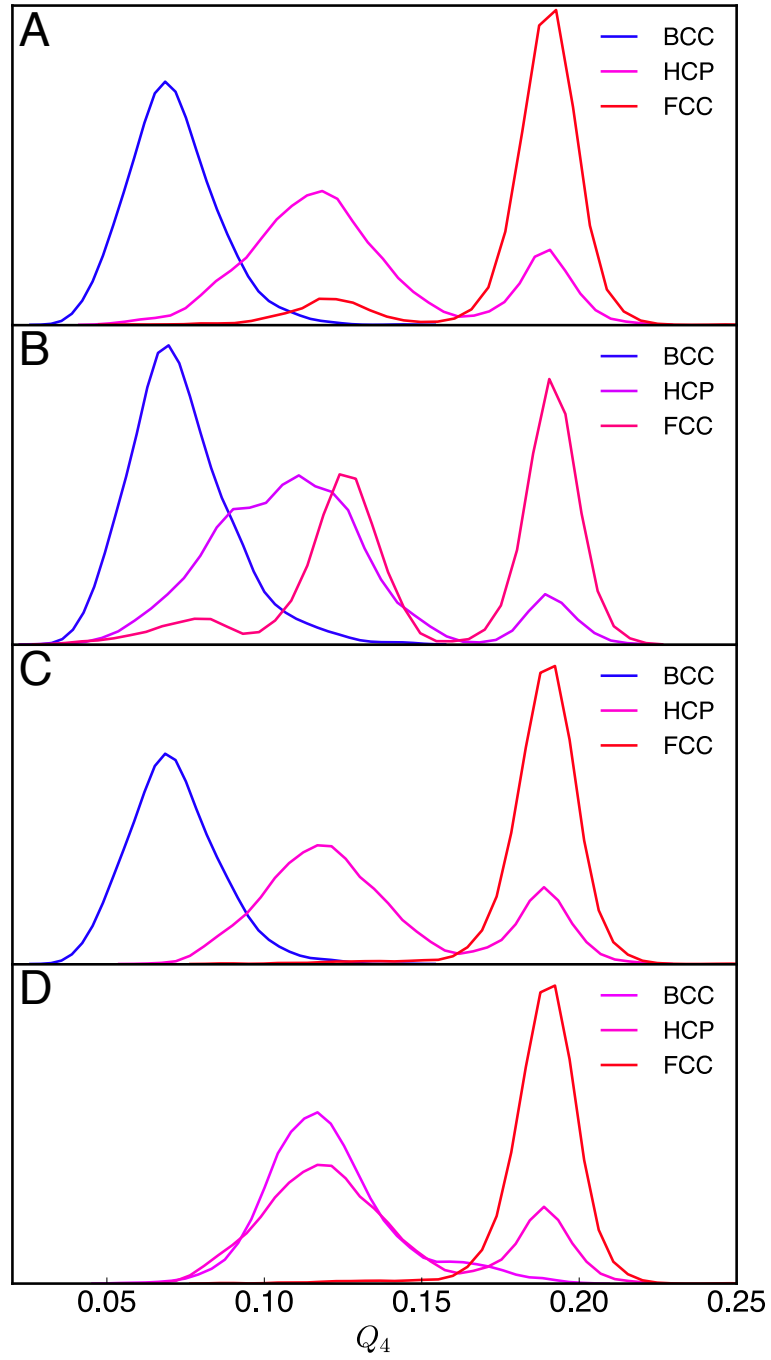
Figure 2.1: Q_4 distribution for BCC, HCP, and FCC. (A) Three different radial cutoffs ($\{1.9, 1.7, 1.7\}$) are applied to the three structures. (B) One radial cutoff (1.8) is applied to the three structures. (C) Three different numbers of nearest neighbor values ($\{14, 12, 12\}$) are applied to the three structures. (D) One nearest neighbor value (12) is applied to the three structures.
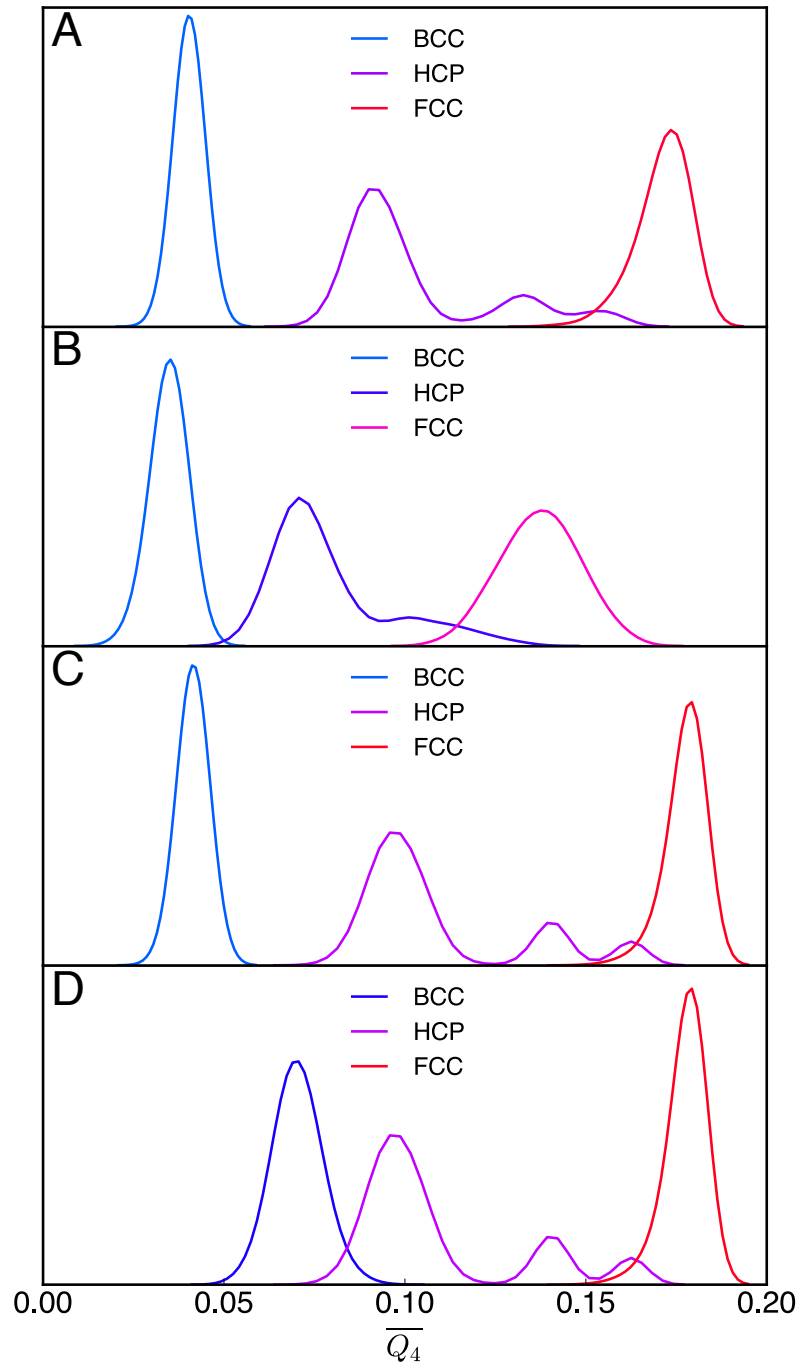
Figure 2.2: $\overline{Q_4}$ distribution for BCC, HCP, and FCC. (A) Three different radial cutoffs ($\{1.9, 1.7, 1.7\}$) are applied to the three structures. (B) One radial cutoff (1.8) is applied to the three structures. (C) Three different numbers of nearest neighbor values ($\{14, 12, 12\}$) are applied to the three structures. (D) One nearest neighbor values (12) is applied to the three structures.

CHAPTER III

Shape Driven Solid–Solid Phase Transitions in Colloids

In this work we study the thermodynamic properties of shape-driven solid–solid phase transitions. We introduce a family of minimal model systems that exhibits solid–solid phase transitions driven by changes in the shape of the colloidal particles. We carry out a detailed investigation of the thermodynamics of a series of isochoric, diffusionless solid–solid phase transitions within a single shape family and find both first and second order phase transitions.

The contents of this chapter are taken from, "Shape-driven Solid–Solid Transitions in Colloids". Chrisy Xiyu Du, Greg van Anders, Richmond S. Newman, and Sharon C. Glotzer, *Proceedings of the National Academy of Sciences* 114.20 (2017): E3892-E3899 [21]. I performed all the simulations and analysis in this paper. All authors contributed to the discussion of results and manuscript writing.

3.1 Model and Simulation Details

In our study, we use a previously studied family of shapes [11], spheric triangle invariant 332 family (Δ_{332}) of hard polyhedra (Fig. 3.1) that have the same point group symmetry and self assemble crystals with small unit cells (1-SC, 2-BCC, and 4-FCC) in adjacent regions of shape space. Δ_{332} is formed by subjecting cubes to two distinct sets of tetrahedral truncations and includes the cube, tetrahedron, and octahedron.
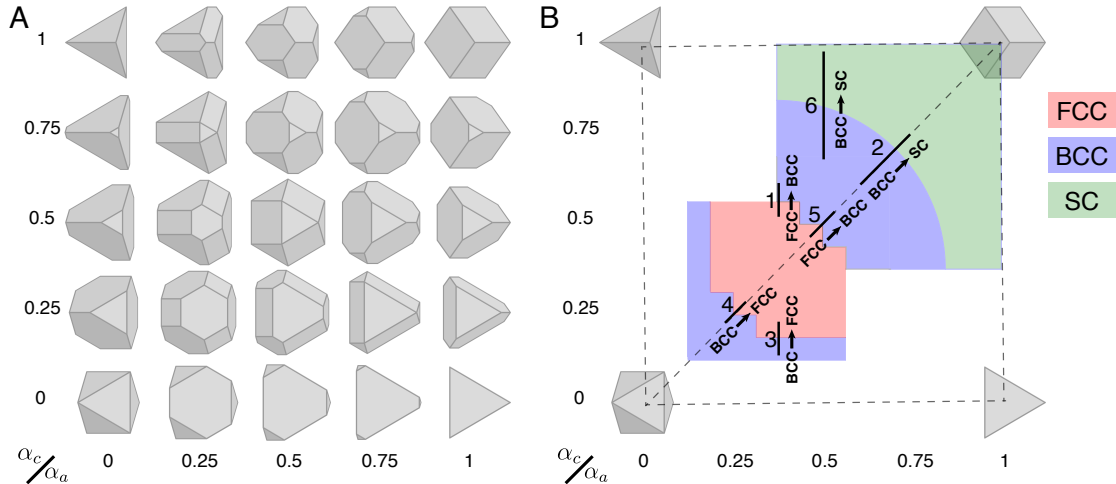
Figure 3.1: (A) Spheric triangle invariant (Δ_{332}) polyhedra form a continuous two-parameter (α_a, α_c) family of symmetric convex shapes that are bounded by the octahedron $[(\alpha_a, \alpha_c) = (0,0)]$, tetrahedron $[(0,1)$ and $(1,0)]$, and cube $(1,1)$. (B) We show six lines indicating regions of shape space in which there is a change in the equilibrium structure at a packing density of $\eta = 0.55$. The lines are annotated with the relevant structural transition and direction. The colors indicate the self-assembled structures, where FCC is red, BCC is blue, and SC is green. The self-assembled phases indicated are an approximated representation from the actual self-assembled phases. Phases in the white region are not of interest in this study. Reproduced from publication [21].

These shapes as well as intermediate shapes in Δ_{332} have been synthesized at the colloidal scale [95, 66, 93, 34]. Simulations of hard colloidal polyhedra in Δ_{332} have shown them to have rich self-assembly behavior (Fig. 3.2 shows three examples) with both wide and narrow regions of thermodynamic stability for a number of different bulk structures [27, 41]. We denote shapes according to the conventions (α_a, α_c), where $0 \leq \alpha_{a,c} \leq 1$ defines the boundaries of shape space in this shape family. With these conventions, $(0,0)$ is an octahedron, $(0,1)$ and $(1,0)$ are tetrahedra (which is self-dual), and $(1,1)$ is a cube (dual to the octahedron). We use conventions in which all particles have unit volume. This is consistent with experimental colloidal systems, where shape variability is typically small, so we can assume all the particles in our system to have the same shape and size.

We investigate shape change-induced solid–solid transitions in Δ_{332} in the regions
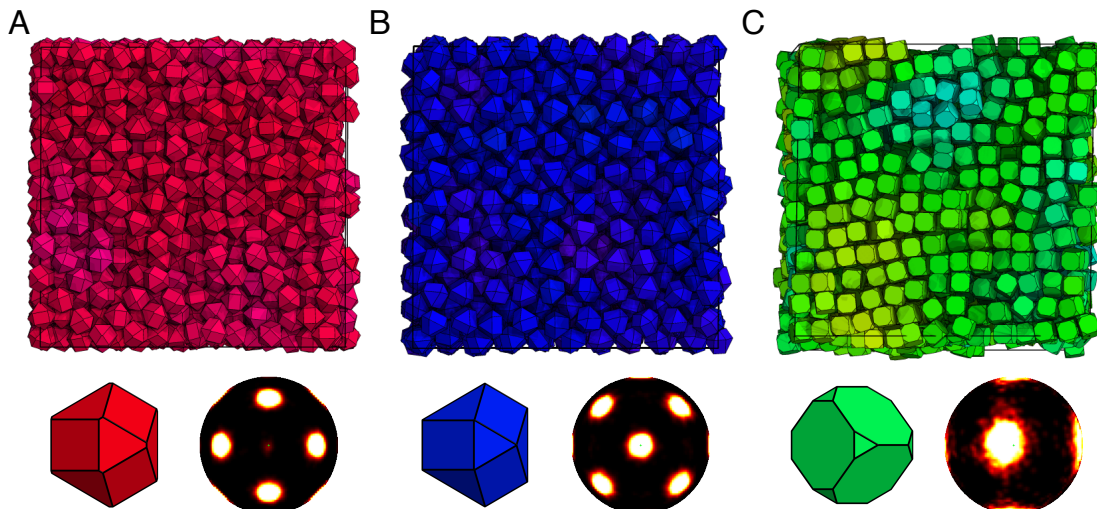
Figure 3.2: Sample self-assembled colloidal crystals formed by shapes in the Δ_{332} triangle-invariant family of hard polyhedra, with images showing particle shape and bond order diagram. (A) An FCC crystal self-assembled from shape $(\alpha_a, \alpha_c) = (0.4, 0.525)$. (B) A BCC crystal self-assembled from shape $(\alpha_a, \alpha_c) = (0.4, 0.59)$. (C) An SC crystal self-assembled from shape $(\alpha_a, \alpha_c) = (0.76, 0.76)$. Note the similarity of shapes in A and B; even small shape differences can affect the bulk self-assembly of hard polyhedra. Shapes in A and B are both on line 1 in Fig. 3.1, and the shape in C is on line 2 in Fig. 3.1. Reproduced from publication [21].

indicated in Fig. 3.1, focusing on BCC, FCC, and SC structures. FCC and BCC as well as SC can be found in neighboring regions of Δ_{332}. We study FCC↔BCC and BCC↔SC transitions, and the regions of investigation indicated in Fig. 3.1 are all known boundaries between the phases of interest in Δ_{332}.

We study the thermodynamics of solid–solid transitions using both the **Ehrenfest** and **Landau** approaches (see, e.g. [30]). All Monte Carlo (MC) simulations and computations were done at fixed packing fraction $\eta = 0.55$, which is sufficiently dense to observe the spontaneous assembly of each of the target phases [27, 41] and sufficiently dilute so as to avoid the complicated infinite pressure behavior of this family of shapes [27, 11]. All simulations were preformed with HPMC [5] in HOOMD-Blue [4], and we use units in which $k_{\mathrm{B}}T = 1$.

3.1.1 Ehrenfest Approach

To estimate the location of phase boundaries, we use the notion of generalized "alchemical" structure-property relationships [86] (see Ch. II for detailed derivations). For this specific system, the generalized partition function is

$$(3.1) \qquad \mathcal{Z}(N, V, T, \mu_a, \mu_c) \equiv e^{-\beta\phi} = \int d\alpha_a d\alpha_c [dp][dq] e^{-\beta(H - \mu_a N\alpha_a - \mu_c N\alpha_c)},$$

where the integral is taken over shape space as well as the ordinary (translational and rotational) phase space of the particles and where $\beta = 1/k_{\mathrm{B}}T$ and $\mu_{a,c}$ are thermodynamically conjugate to the shape variables $\alpha_{a,c}$ and referred to as "alchemical potentials" [86]. We can make a Legendre transformation of the free energy ϕ from the $NVT\mu_a\mu_c$ ensemble to the free energy $F = \phi + \mu_a N\alpha_a + \mu_c N\alpha_c$ of the $NVT\alpha_a\alpha_c$ ensemble, from which we can extract the constitutive relation

$$(3.2) \qquad P(\alpha_a, \alpha_c) = -\left(\frac{\partial F}{\partial V}\right)_{N,T,\alpha_a,\alpha_c}.$$

A thermodynamic phase transition, by the standard approach of Ehrenfest (see e.g. [30]), is indicated if a thermodynamic quantity [e.g., $P(\alpha_a, \alpha_c)$] or any of its derivatives is discontinuous. A discontinuity of $P(\alpha_a, \alpha_c)$ signals a thermodynamic phase transition in shape space because of the explicit shape dependence in this relation. Accordingly, we searched for discontinuities by initializing systems with different building blocks (examples are in Fig. 3.3A and C) in perfect BCC ($N = 2000$), FCC ($N = 2048$), or SC ($N = 2197$) structures and computed $P(\alpha_a, \alpha_c)$ (Fig. 3.3B and D) after 1.5×10^7 MC steps to ensure that systems reach equilibrium or metastable equilibrium using standard techniques [23].

3.1.2 Landau Approach

Having located discontinuities in $P(\alpha_a, \alpha_c)$ and its derivatives, we computed the free energy as a function of order parameter(i.e., the Landau free energy) (see e.g.

[30]) for a series of fixed particle shapes near the solid–solid transition using umbrella sampling [82]. To quantify the system crystal structure, we used a neighbor-averaged [44] version of the standard local bond order parameters [79]. To achieve good order parametric separation of our crystal phases of interest, we used the second neighbor-averaged $l = 4$ parameter $\overline{Q}_4$, which distinguishes BCC from FCC, SC, and HCP phases in our systems as shown in Figs. 3.5B and 3.9B. To confirm the validity of $\overline{Q}_4$ as an order parameter for monitoring the FCC$\leftrightarrow$BCC transitions, we plot thermal averages of $\overline{Q}_4$ computed in BCC, HCP, and FCC in Fig. 3.5B. Data indicates that BCC structure has a peak near $\overline{Q}_4 = 0.06$, that HCP has a peak near $\overline{Q}_4 = 0.09$ and a second smaller peak around $\overline{Q}_4 = 0.13$ because of mixed HCP-FCC stacking, and that FCC has a peak near $\overline{Q}_4 = 0.17$. The peaks are well-separated, and therefor, $\overline{Q}_4$ is a good distinguishing measure of a crystal structure. Umbrella sampling simulations used 5×10^4 samples in 32 equally spaces windows in $\overline{Q}_4$ across each transition with a biased harmonic potential of spring constant $k = 3.5 \times 10^4$. [k is parametrically large because it scales like the inverse square of the resolution of the order parameter, $\delta \overline{Q}_4$. For our structures of interest, $\overline{Q}_4$ falls in the range of $0.05 - 0.2$, so that we need to be able to resolve order parameter intervals of $\delta \overline{Q}_4 \approx 0.005$. The value $k = 3.5 \times 10^4$ that we found to be consistent with efficient sampling is consistent with a naive estimate $k \approx (\delta \overline{Q}_4)^{-2}$.] We study FCC$\leftrightarrow$BCC transitions in four distinct regions of shape space, in each case using six polyhedra with shapes near the solid–solid transition; all systems contained $N = 500$ particles (Fig. 3.5A). For BCC$\leftrightarrow$SC transitions, we studied two distinct regions of shape space, in both cases using different polyhedra in systems of $N = 432$ particles (Fig. 3.9A). In all cases, five independent replicates were used to generate umbrella samples. Umbrella samples were used to reconstruct free energy curves using the weighted histogram analysis method [43], and errors

were estimated using jackknife resampling [22].

3.2 Results

We first present thermodynamic findings of FCC↔BCC and BCC↔SC transitions. Then we will briefly talk about the dynamics of these two transitions.

3.2.1 Thermodynamic Properties

FCC↔BCC Transitions

We investigated the thermodynamics of shape change-driven FCC↔BCC solid–solid phase transitions in four distinct regions of shape space (indicated by lines 1 and 3-5 in Fig. 3.1). In each region, at the FCC↔BCC cross-over, we find that the $P(\alpha_a, \alpha_c)$ constitutive relation exhibits a discontinuous first derivative (Fig. 3.3B, 3.4B), indicating a phase transition that is either first or second order in the Ehrenfest classification [30]. Additional investigation via umbrella sampling yields the Landau free energy near the putative solid–solid transition for six different shapes depicted in Fig. 3.5A, 3.6A, 3.7A, 3.8A. Note that the similarity in particle shapes makes them difficult to distinguish by eye but is most clearly indicated by the relative size of the square face. Particles are colored from blue (BCC) to red (FCC) according to the structures that they spontaneously self-assemble. More blue (more red) shapes are more likely to form BCC (FCC). Shapes colored purple exhibit an almost equal probability to form either BCC or FCC. We computed the Landau free energy using the order parameter $\overline{Q}_4$ defined above. In Fig. 3.5, 3.6, 3.7, 3.8 C and D, we plot Landau free energies obtained from umbrella sampling after averaging from five independent replica runs on both sides of the solid–solid phase transition. Calculations at $\alpha_c > (<)\alpha_c^*$ ($\alpha_{a,c} > (<)\alpha_{a,c}^*$) (i.e., above(below) the FCC↔BCC transition) (Fig. 3.5C, 3.6C, 3.7C, 3.8C) show that, sufficiently far

into the BCC phase, there is no metastable FCC free energy basin; however, as α_c ($\alpha_{a,c}$) approaches α_c^* ($\alpha_{a,c}^*$), a metastable FCC basin appears. At $\alpha_c < (>)\alpha_c^*$ ($\alpha_{a,c} < (>)\alpha_{a,c}^*$) (Fig. 3.5D, 3.6D, 3.7D, 3.8D), umbrella sampling calculations show that FCC becomes the stable free energy basin and that the BCC basin disappears, but a metastable basin develops that corresponds to mixed FCC and HCP stacking. Together with the results from four distinct regions, we show that shape change-driven FCC↔BCC solid–solid phase transitions in Δ_{332} are first-order thermodynamic phase transitions.

BCC↔SC Transitions

We investigated the thermodynamics of BCC↔SC solid–solid phase transitions in two distinct regions of shape space (lines 2 and 6 in Fig. 3.1). In Fig. 3.3D, 3.4D, we plot the $P(\alpha_a, \alpha_c)$ constitutive relation with $\alpha_a = \alpha_c \equiv \alpha$ for region 2 and fixed $\alpha_a = 0.5$ for region 6, which shows a discontinuity in pressure near $\alpha \approx 0.6$ and $\alpha_c \approx 0.68$ consistent with a phase transition that is, at most, second order in the Ehrenfest classification. A close-up view of these data for line 2 is presented in Fig. 3.11B. Fig. 3.11A shows $\overline{Q}_4$ order parameter measurements that suggest a discontinuous first derivative with respect to α, which is also consistent with a continuous (i.e., second or higher order) thermodynamic phase transition. Corroborating evidence is provided by computing the Landau free energy as a function of the order parameter $\overline{Q}_4$ near the putative solid–solid transition via umbrella sampling for a range of shapes indicated in Fig. 3.9A and Fig. 3.10A. Particles are colored from blue (BCC) to green (SC) according to the value of the order parameter $\overline{Q}_4$ of the structures into which they self-assemble. Computed thermal averages (Fig. 3.9) of the order parameter $\overline{Q}_4$ in BCC and SC crystals show that BCC crystals have a peak near 0.08 and that SC has a peak near 0.17; however, our result also suggest the existence of structures

with intermediate $\overline{Q}_4$ for intermediate particle shapes, where their self-assembled structures are in between BCC and SC as shown in their $\overline{Q}_4$ distribution. Landau free energies computed via umbrella sampling are plotted in Fig. 3.9C, Fig. 3.10C and show no evidence of secondary local minima that would indicate a discontinuous (i.e., first-order) phase transition. Umbrella sampling computations were performed at a higher resolution of shape space below the putative transition ($\alpha \lesssim 0.6$) to extract the expected value of the order parameter $\overline{Q}_4$ (Fig. 3.9D) and are consistent with the self-assembled $\overline{Q}_4$ measurements (Fig. 3.11), suggesting that $\overline{Q}_4$ has a discontinuous derivative at the transition. Together, the $P(\alpha_a, \alpha_c)$ constitutive relation, the direct evaluation of the order parameter $\overline{Q}_4$, and the umbrella sampling results all indicate that the BCC↔SC solid–solid phase transition is a continuous (i.e., second- order higher-order) thermodynamic phase transition in Δ_{332}.

3.2.2 Dynamic Properties

FCC↔BCC Transitions

We investigated the dynamics of the FCC↔BCC solid–solid phase transition by modeling how the system responds to a sudden change in particle shape. Several experimental techniques exist for dynamically altering colloid shape [26, 45, 49, 94]. Here, we model a process in which particle shape reconfiguration occurs on a much shorter timescale than structural relaxation by initializing FCC-forming particles in BCC structure (and vice versa) and simulating at fixed particle shape and packing density for 1.5×10^7 MC sweeps. On these simulation timescales, which are long compared with typical structural relaxation times and much longer than needed for the solid–solid transition outside the metastable region, we did not observe structural transformation for any systems that our umbrella sampling simulation indicated as metastable. Homogeneous nucleation is inherently a rare event, and our MC

simulations in metastable regions of shape space suggest that the driving force for structural reconfiguration is not sufficient to overcome the free energy barrier to observe a first-order solid–solid phase transition on timescales that are typically sufficient to observe first-order fluid-solid phase transitions in systems of this type [1, 13, 14, 84]. However, we did observe a spontaneous solid–solid transition when systems were initialized with shapes beyond the metastable region, in which case we observed structural reconfiguration with no discernible intermediate fluid phase. The existence of metastability in shape space provides an additional confirmation that the solid–solid transition is first order. Moreover, by measuring the order parameter evolution in MC simulation, our results indicate that the transition pathway in MC simulation follows the order parameter that we chose in umbrella sampling, providing additional confirmation that it appropriately parametrizes the FCC↔BCC solid–solid transition.

BCC↔SC Transitions

Similarly, we investigated the dynamics of the BCC↔SC solid–solid phase transformation by modeling how the system responds to a sudden change in particle shape. We model a process in which particle shape reconfiguration occurs on a much shorter timescale than the structural relaxation by initializing BCC-forming particles in SC structure (and vice versa) and simulating at fixed particle shape and packing density for 1.5×10^7 MC sweeps. On these simulation timescales, in all cases, we observed dynamic solid–solid phase transformations via a transition pathway through intermediate structures that follow the order parameter that we used for umbrella sampling. Moreover, we observe that, for α above the transition, any shape perturbation induces a structural change with no evidence of metastability. We also observe that the dynamics of the solid–solid transformation occurs on typical timescales of 2×10^6

MC sweeps. Taken together, these results provide additional corroboration of our observation that BCC↔SC is a continuous thermodynamic phase transition in Δ_{332} at fixed packing fraction $\eta = 0.55$, and the timescale under which the solid–solid transition occurs dynamically is shorter by nearly an order of magnitude than in the case of FCC↔BCC.

3.2.3 Error Analysis

All error bars in the free energy plots are generated using jackknife resampling. We selected ten different subsets of all the data from the replica runs and stitched together the resulting free energy curves from the subsets. The error from WHAM [43] is negligible. However, jackknife resampling can only compute the statistical error; due to the large sample size ($50000 \times 5 = 250000$), the statistical error is still small. The largest and most difficult error to calculate is the systematic error of umbrella sampling. This systematic error can come from multiple sources. First, due to the equilibration routine of the umbrella sampling simulation, for each individual window, the final distribution can be shifted slightly to the left or right of the target $\overline{Q}_4$ value for each independent run. Second, the initial state of the system can also affect the end result slightly. Because of this, we conducted simulations from the two extreme cases, initializing the system with the two solid phases we wish to study, and compared the free energy of the end result. In Fig. 3.12 and 3.13, we can see that the free energy curves shifted slightly with different initialization, but the macroscopic behavior of the phase transitions stay the same.

3.3 Discussion

Motivated by (i) the need for minimal models to study solid–solid transitions [61], (ii) the observation that, in these transitions, coordination polyhedra [55] change

shape , (iii) the connection between anisotropic colloid shape and valence [84, 85], (iv) the large body of work on entropy-driven ordering in systems of colloids with anisotropic shape [17, 13, 56, 1, 66, 14, 34, 2, 27, 85, 84, 53], and (v) recently developed techniques for treating particle shape thermodynamically [86], we studied a class of minimal model systems exhibiting solid–solid phase transitions driven by changes in particle shape. We showed via MC simulation and umbrella sampling techniques, that particle shape change gives rise to several distinct solid–solid transitions in a single family of shapes. We investigated FCC↔BCC and BCC↔SC transitions. Both FCC↔BCC and BCC↔SC are solid–solid transitions that are related by linear transformations of the positions of the particle centers. BCC and FCC are related by elongation in one direction [6]; BCC and SC are related by a shear transformation within the unit cell [46]. Both transitions are expected to be diffusionless. Surprisingly, despite both being diffusionless transitions and the common point group symmetry of the particle shape, we find that the FCC↔BCC transition is thermodynamically discontinuous (i.e., first order) and that BCC↔SC is thermodynamically continuous (i.e., second or higher order). Our results suggest several directions for additional investigation, which will be discussed in the next section.

Our results can help guide the synthesis of reconfigurable colloidal material (Fig. 3.14). Experiments have shown systems with changeable building block shape either directly [26, 45, 70, 97, 49] or effectively via depletion [67, 38, 15]. Here, we show that, for colloidal particles that can be synthesized in the laboratory [66, 34], changing particle shape can be used to induce transformations between FCC↔BCC and BCC↔SC. What implications are there for the rational design of reconfigurable colloidal materials? To answer this question, it is important to understand how struc-

tural reconfiguration compares with self-assembly in terms of typical timescales. We obtain "timescales" via MC simulations involving local translations and rotations of individual particles to approximate the Brownian dynamics [24] of physical colloids [80]. In the case of FCC↔BCC, for shapes near the discontinuous transition ($|\alpha - \alpha^*| \lesssim 0.05$), we did not observe spontaneous structural reconfiguration in systems of $N \sim 2,000$ particles on timescales of $\tau \lesssim 10^7$ MC sweeps. This timescale is much longer than the typical time that it takes to observe spontaneous crystallization or melting in MC simulations of the self-assembly of $N \sim 2 \times 10^3$ particles, for which $\tau \sim 10^7$. The contrasting timescales for self-assembly vs. solid–solid reconfiguration suggest that, for small shape deformations of $|\alpha - \alpha^*| \lesssim 0.05$, spontaneous, shape change-driven, dynamic FCC↔BCC reconfiguration in Δ_{332} can be achieved on shorter timescales by completely melting and then recrystallizing the system. However, for larger shape changes $|\alpha - \alpha^*| \gtrsim 0.05$, we observed spontaneous FCC↔BCC reconfiguration on timescales of $\tau \sim 10^6$ MC sweeps. The relatively short timescales observed for reconfiguration suggests that, for sufficiently large shape deformations, although the phase transition is first order, direct solid–solid reconfiguration without an intermediate fluid can occur on comparable physical timescales to self-assembly and therefore, is a viable means of designing reconfigurable colloidal materials. In the BCC↔SC case, the continuous nature of the transition implies that there is no nucleation barrier, and indeed, we observed structural reconfiguration in MC simulations of $N \sim 2 \times 10^3$ particles on typical timescales of $\tau \sim 10^6$, which is less than what is typically observed for self-assembly of comparably sized systems of hard anisotropic colloids. The relatively fast speed at which structural reconfiguration occurs in this case of a continuous solid–solid transition suggests that a broader search for other systems of anisotropic colloids that exhibit continuous solid–solid

phase transitions could yield candidate systems for developing rapidly switchable reconfigurable colloidal materials.

3.4 Outlook

The physics of FCC$\leftrightarrow$BCC solid–solid phase transitions is of longstanding interest in metallurgy [e.g., in the transition between the so-called γ (FCC) and α (BCC) forms of iron [6]]. We found that, for several distinct regions of shape space, the FCC$\leftrightarrow$BCC solid–solid phase transition is discontinuous. It is possible that, for particles with other paths of shape shifting, there could be less/no thermal activation; we will address this question in Ch. IV. Additionally, although our focus here was on solid–solid transitions between cubic crystals with four or fewer particles per cubic unit cell, studies of noncubic crystals or crystals with more complicated unit cells require only straightforward generalizations of our approach. We expect that the approach that we have developed here will provide a powerful framework for the study of the basic physics of solid–solid phase transitions between a wide array of technologically relevant structures.

Constructing shape-driven solid–solid transitions furthers the aim of developing minimal models of these transitions because it allows the direct manipulation of co-ordination polyhedra. As we noted above, coordination polyhedra also reconfigure in solid–solid transitions in metallurgy with changes in pressure, density, or temperature. An additional complicating factor in those transitions is that both enthalpy and entropy play a role, and decoupling their effects is difficult [25]. A side benefit of our approach is that, in the hard particle systems we present here, the behavior is entirely driven by entropy. Future studies of systems with controllable shape and enthalpic interactions [84] could allow enthalpic and entropic contributions to be dis-

entangled. An important question for additional investigation is whether the physics of solid–solid transitions is determined by the structures, the particle shapes, or an interplay between the two.

Another fundamental question that calls for additional investigation is the study of the kinetics of colloidal solid–solid phase transformations through nonclassical nucleation and growth. It is expected that the nucleation and growth of solid–solid transitions will be rich because crystals break the rotational symmetry required by classical nucleation theory, and recent experimental evidence [61, 73] shows evidence for two-step nucleation in quasi-2D systems. Minimal models of the type constructed here provide an avenue for the study of full 3D transformations.
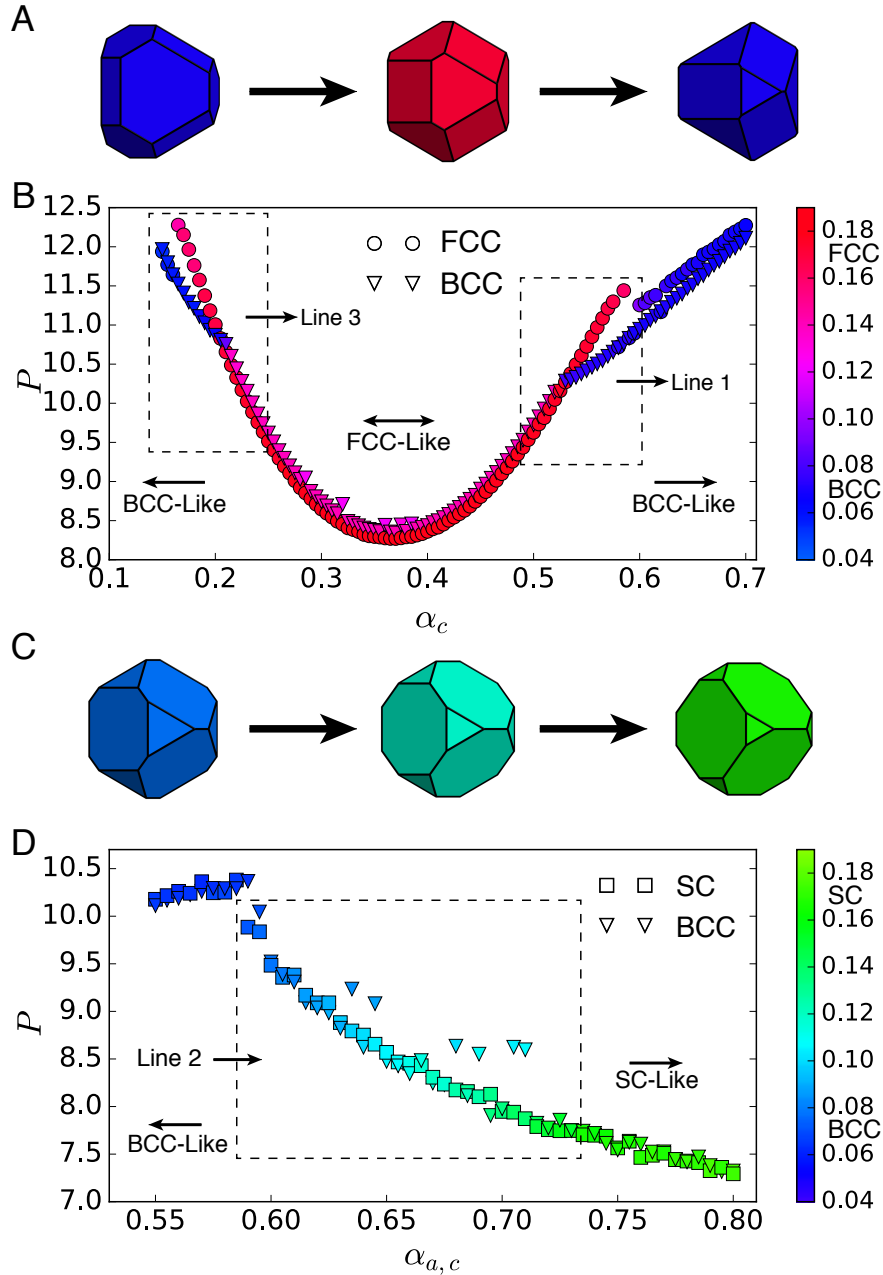
Figure 3.3: Pressure-shape constitutive relation for $\alpha_a = 0.4$ and $\alpha_a = \alpha_c$. (A) Shape evolution in α_c at fixed $\alpha_a = 0.4$. Shapes vary from self-assemble into BCC (blue) to FCC (red) and then back to BCC (blue). (B) Pressure-shape constitutive relation for fixed $\alpha_a = 0.4$. Circles indicate FCC system initialization, and triangles indicate BCC system initialization. Marker colors indicate the value of the order parameter $\overline{Q}_4$ computed in the final structure of the system after equilibration. Boxed regions show the BCC↔FCC boundaries corresponding to lines 1 and 3 in Fig. 3.1. Errors are smaller than marker size. (C) Shape evolution for $\alpha_a = \alpha_c$. Shapes vary from self-assemble into BCC (blue) to SC (green). (D) Pressure-shape constitutive relation for $\alpha_a = \alpha_c$. Squares indicate SC system initialization; triangles indicate BCC initialization. Marker colors indicate the value of the order parameter $\overline{Q}_4$ computed in the final structure of the system after equilibration. Boxed regions show BCC↔SC boundaries corresponding to line 2 in Fig. 3.1. Errors are smaller than marker size. Outliers are systems that did not equilibrate in 2×10^7 MC steps. Reproduced from publication [21].
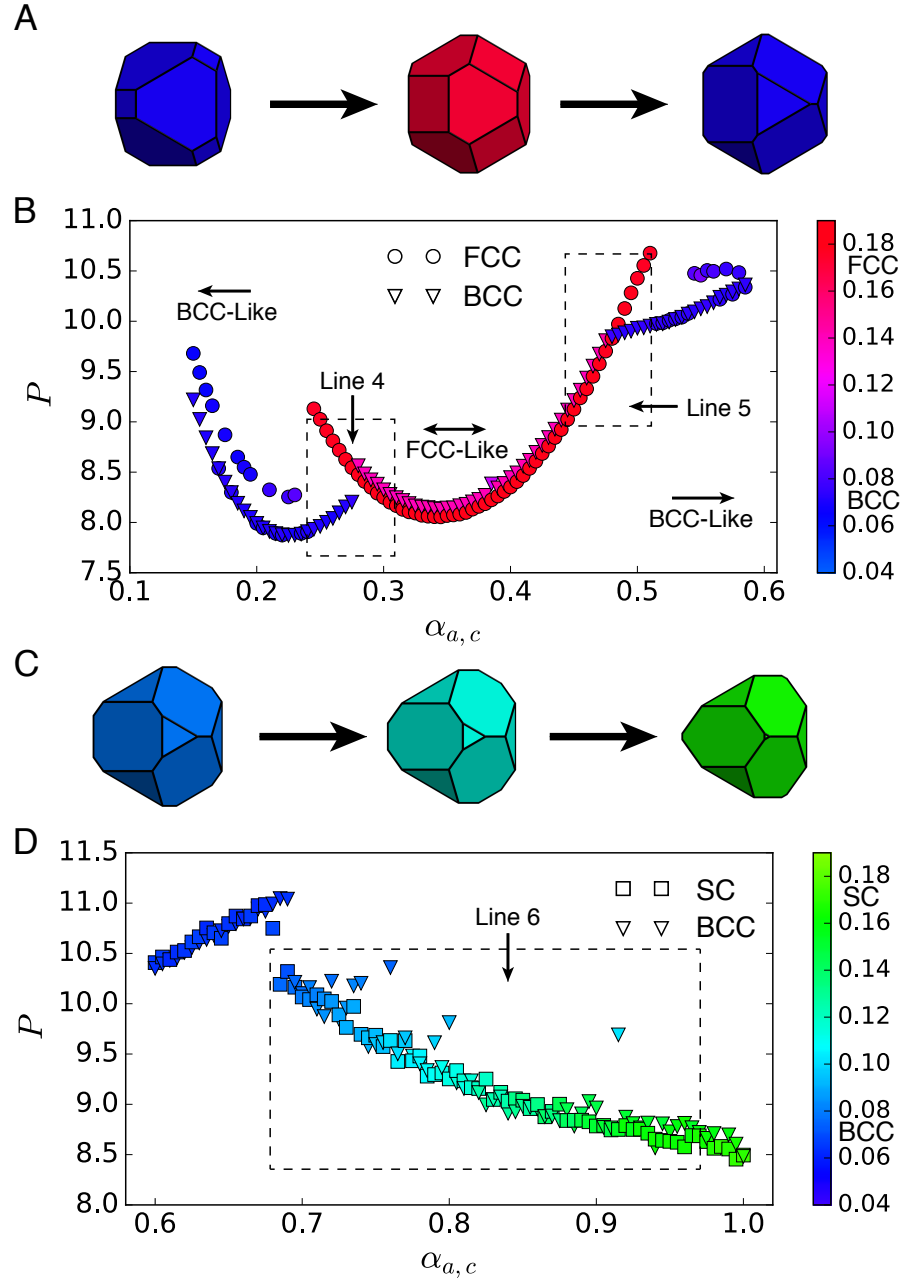
Figure 3.4: Pressure-shape constitutive relation for $\alpha_a = 0.5$ and $\alpha_a = \alpha_c$. (A) Shape evolution for $\alpha_a = \alpha_c$. Shapes vary from self-assemble into BCC (blue) to FCC (red) and then back to BCC (blue). (B) Pressure-shape constitutive relation for $\alpha_a = \alpha_c$. Circles indicate FCC system initialization, and triangles indicate BCC system initialization. Marker colors indicate the value of the order parameter $\overline{Q}_4$ computed in the final structure of the system after equilibration. Boxed regions show the BCC↔FCC boundaries corresponding to lines 4 and 5 in Fig. 3.1. Errors are smaller than marker size. (C) Shape evolution in α_c at fixed $\alpha_a = 0.5$. Shapes vary from self-assemble into BCC (blue) to SC (green). (D) Pressure-shape constitutive relation for fixed $\alpha_a = 0.4$. Squares indicate SC system initialization; triangles indicate BCC initialization. Marker colors indicate the value of the order parameter $\overline{Q}_4$ computed in the final structure of the system after equilibration. Boxed regions show BCC↔SC boundaries corresponding to line 6 in Fig. 3.1. Errors are smaller than marker size. Outliers are systems that did not equilibrate in 2×10^7 MC steps. Reproduced from publication [21].
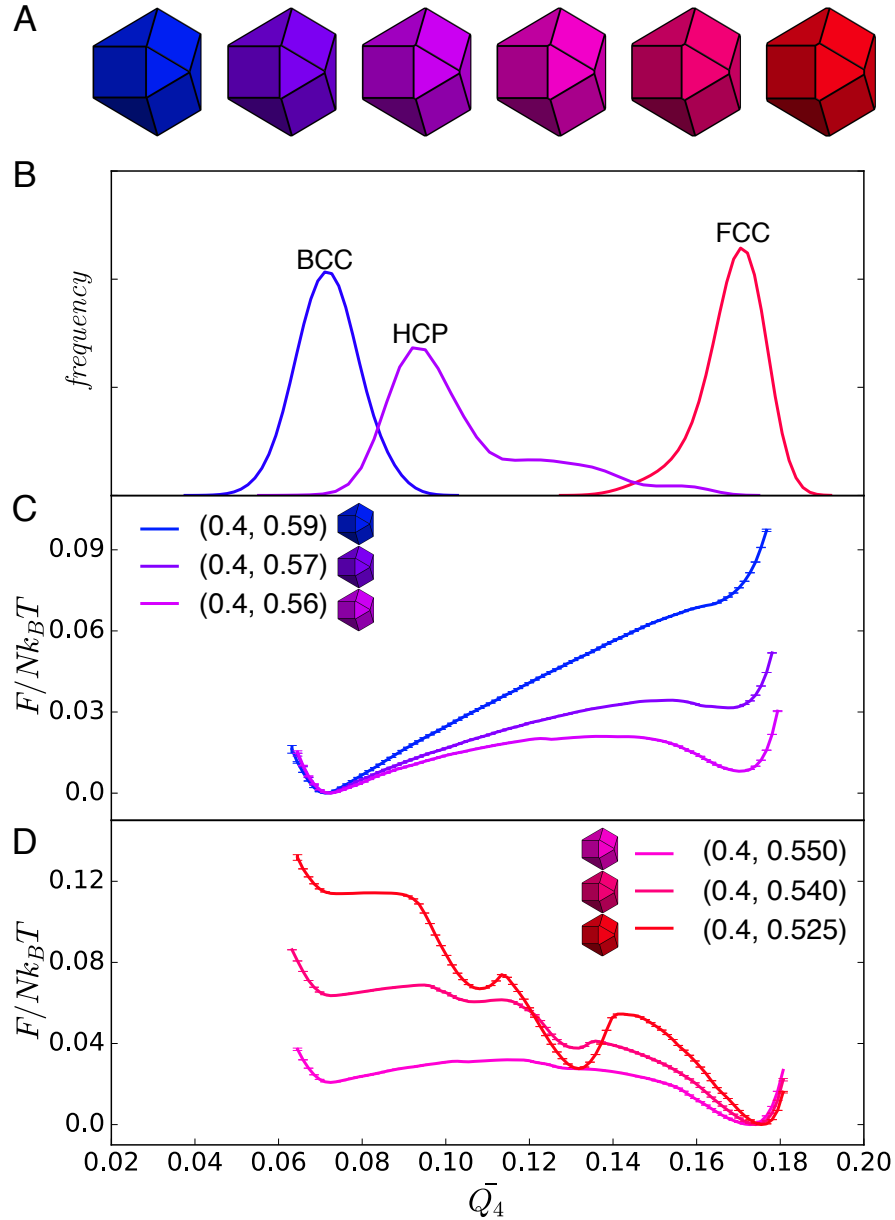
Figure 3.5: Shape-induced structural FCC↔BCC reconfiguration is accompanied by a first-order thermodynamic phase transition in spheric triangle invariant hard polyhedra. (A) Shapes used in umbrella sampling simulations. (B) Second neighbor-averaged $l = 4$ spherical harmonic order parameter $\overline{Q}_4$ distinguishes BCC, FCC, and HCP crystal structures in thermal systems of spheric triangle invariant polyhedra. (C) Above the transition ($\alpha_c > \alpha_c^*$), a metastable FCC free energy basin develops near $\alpha_c = 0.58$. (D) Below the transition ($\alpha_c < \alpha_c^*$), the FCC free energy basin becomes dominant ($\alpha_c = 0.55$), and well below the transition ($\alpha_c = 0.54$), the BCC free energy basin becomes unstable, and a second metastable HCP basin appears. Reproduced from publication [21].
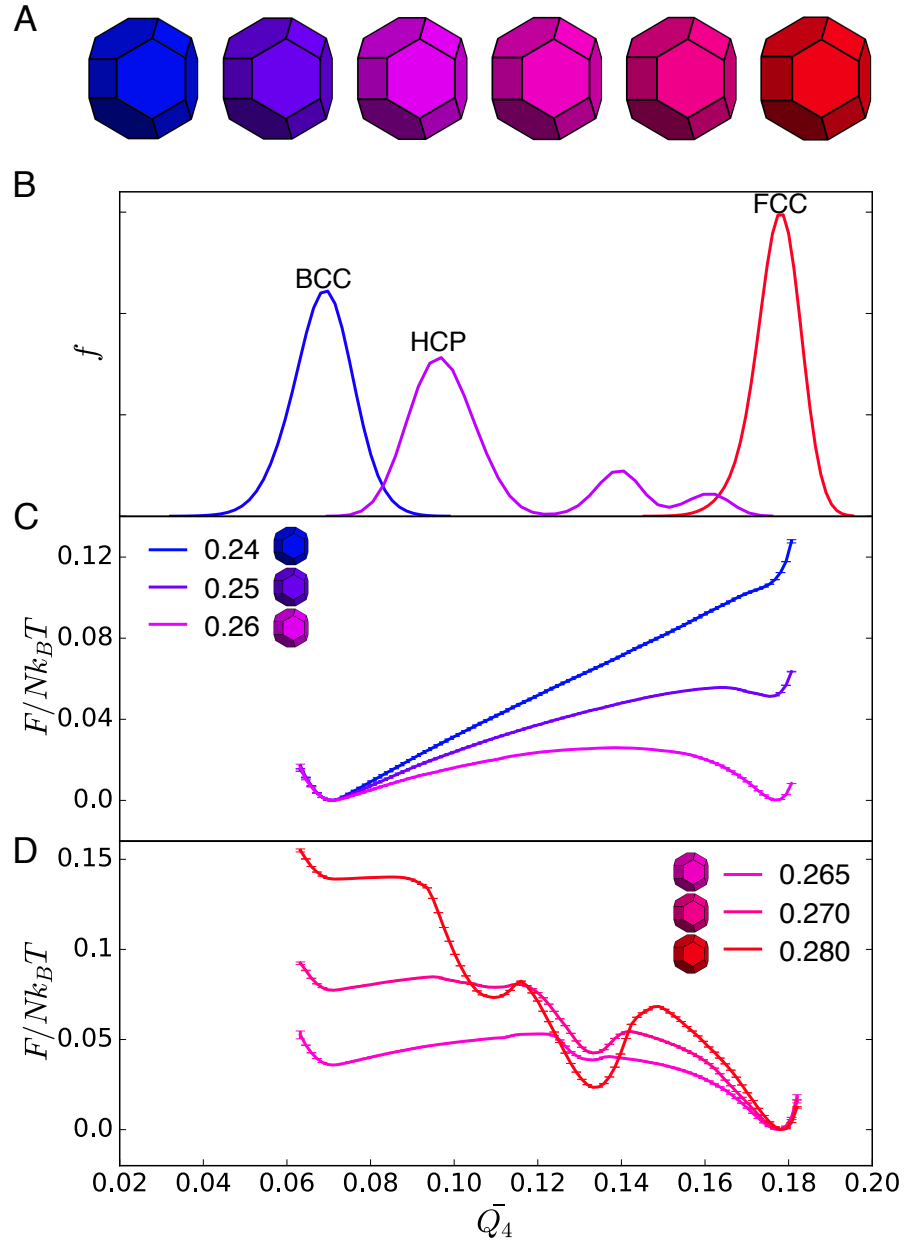
Figure 3.6: Shape-induced structural FCC↔BCC reconfiguration is accompanied by a first-order thermodynamic phase transition in spheric triangle invariant hard polyhedra. (A) Shapes used in umbrella sampling simulations. (B) Second neighbor-averaged $l = 4$ spherical harmonic order parameter $\overline{Q}_4$ distinguishes BCC, FCC, and HCP crystal structures in thermal systems of spheric triangle invariant polyhedra. (C) Below the transition ($\alpha_c < \alpha_c^*$), a metastable FCC free energy basin develops near $\alpha_{a,c} = 0.25$. (D) Above the transition ($\alpha_c > \alpha_c^*$), the FCC free energy basin becomes dominant ($\alpha_{a,c} = 0.265$), and well above the transition ($\alpha_c = 0.28$), the BCC free energy basin becomes unstable, and a second metastable HCP basin appears. Reproduced from publication [21].
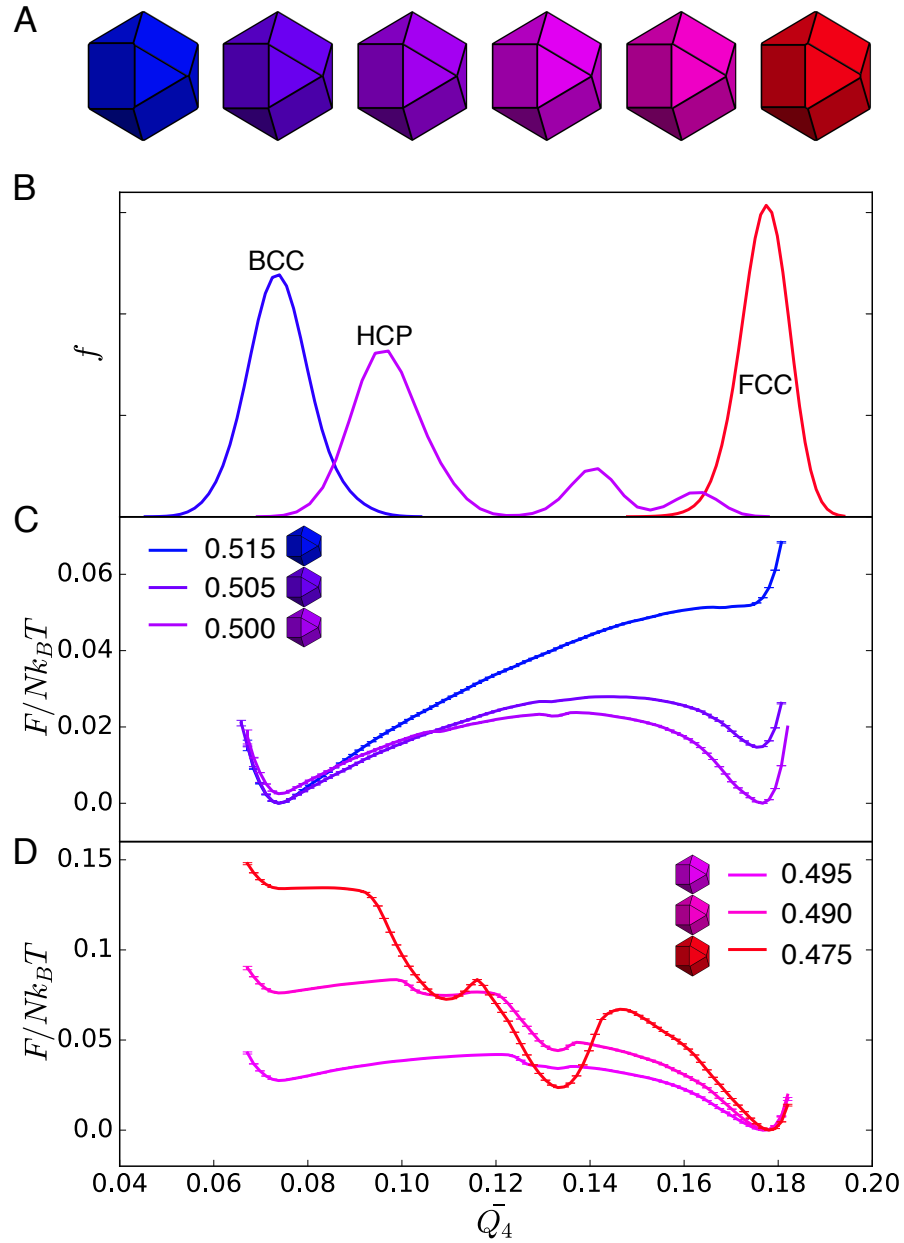
Figure 3.7: Shape-induced structural FCC↔BCC reconfiguration is accompanied by a first-order thermodynamic phase transition in spheric triangle invariant hard polyhedra. (A) Shapes used in umbrella sampling simulations. (B) Second neighbor-averaged $l = 4$ spherical harmonic order parameter $\overline{Q}_4$ distinguishes BCC, FCC, and HCP crystal structures in thermal systems of spheric triangle invariant polyhedra. (C) Above the transition ($\alpha_c > \alpha_c^*$), a metastable FCC free energy basin develops near $\alpha_{a,c} = 0.505$. (D) Below the transition ($\alpha_c < \alpha_c^*$), the FCC free energy basin becomes dominant ($\alpha_{a,c} = 0.495$), and well below the transition ($\alpha_c = 0.475$), the BCC free energy basin becomes unstable, and a second metastable HCP basin appears. Reproduced from publication [21].
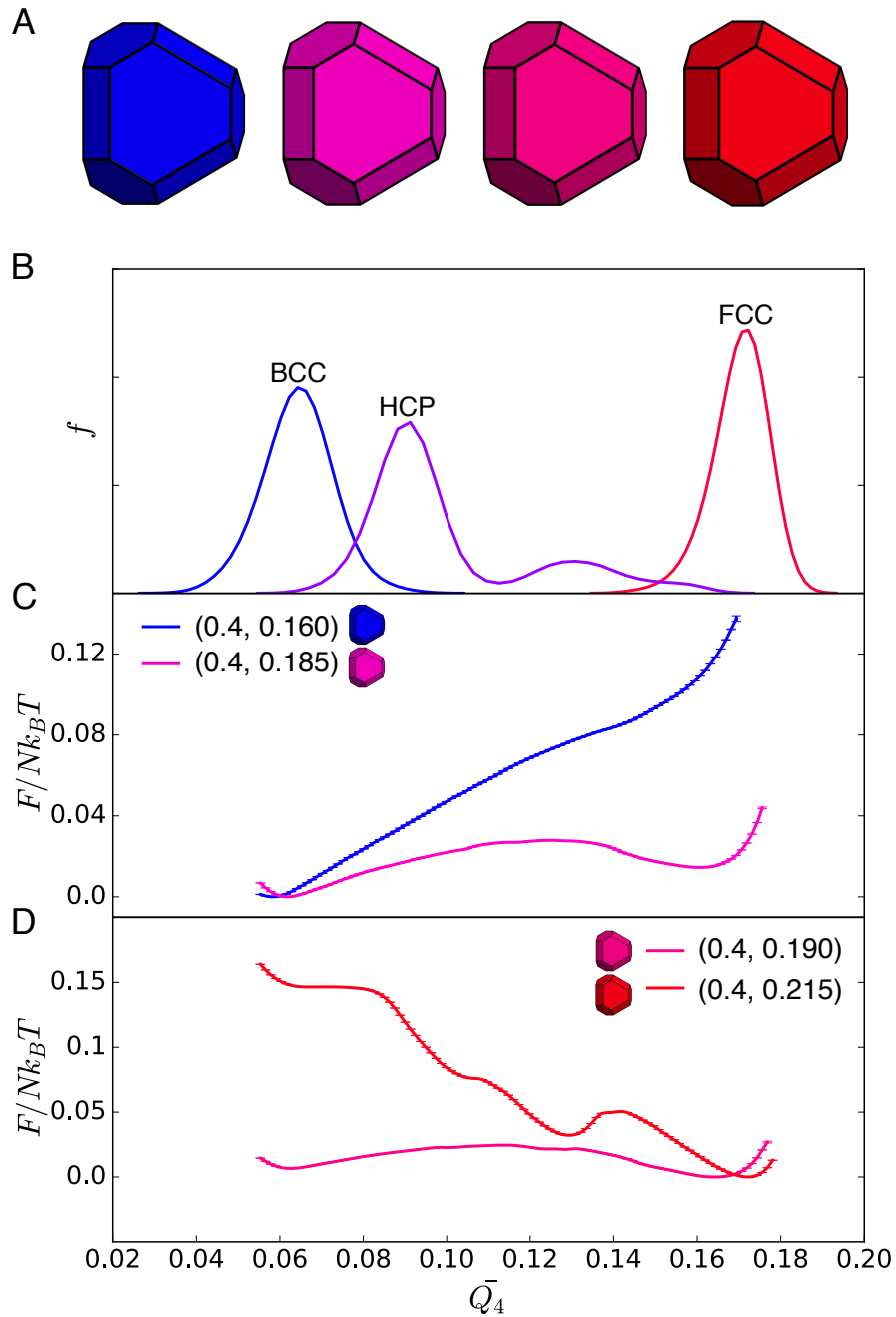
Figure 3.8: Shape-induced structural FCC↔BCC reconfiguration is accompanied by a first-order thermodynamic phase transition in spheric triangle invariant hard polyhedra. (A) Shapes used in umbrella sampling simulations. (B) Second neighbor-averaged $l = 4$ spherical harmonic order parameter $\overline{Q}_4$ distinguishes BCC, FCC, and HCP crystal structures in thermal systems of spheric triangle invariant polyhedra. (C) Below the transition $(\alpha_c < \alpha_c^*)$, a metastable FCC free energy basin develops near $\alpha_c = 0.185$. (D) Above the transition $(\alpha_c > \alpha_c^*)$, the FCC free energy basin becomes dominant $(\alpha_c = 0.19)$, and well above the transition $(\alpha_c = 0.215)$, the BCC free energy basin becomes unstable, and a second metastable HCP basin appears. Reproduced from publication [21].
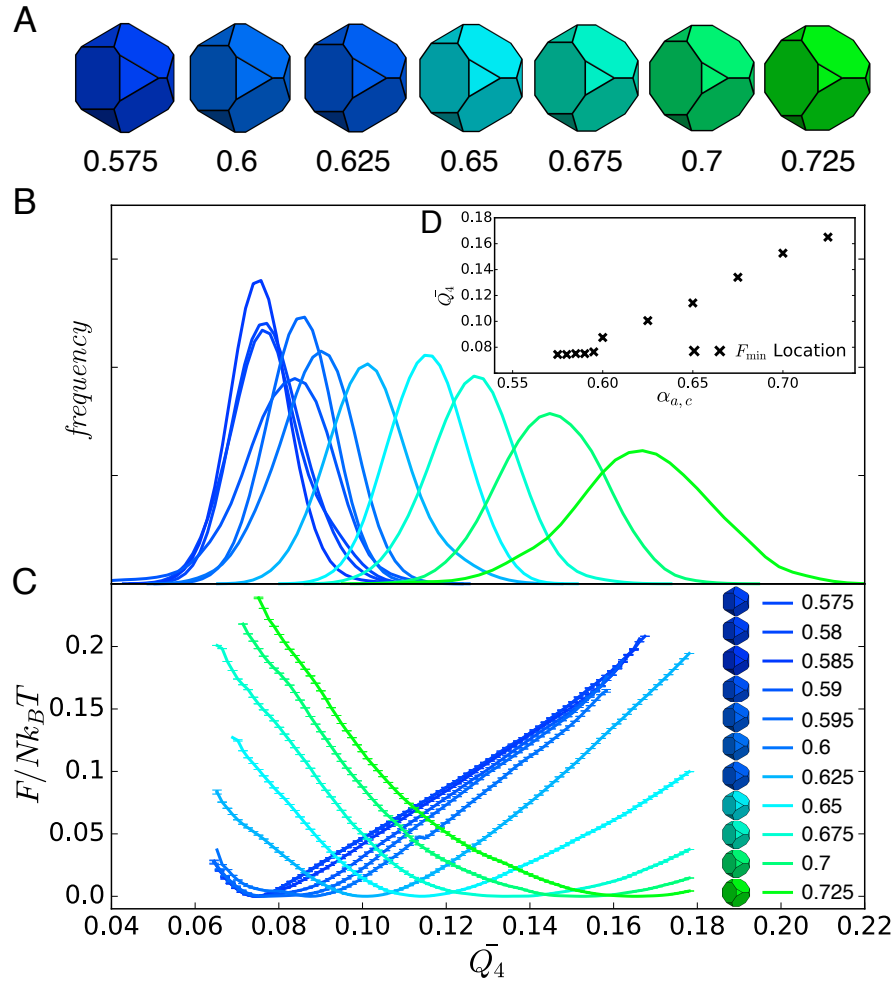
Figure 3.9: Shape-induced structural BCC↔SC reconfiguration occurs continuously in spheric triangle invariant hard polyhedra. (A) Sample shapes used in umbrella sampling simulation from the start to end in equal space. C shows all shapes. (B) Second neighbor-averaged $l = 4$ spherical harmonic order parameter $\overline{Q}_4$ shows a series of structures between BCC and SC. (C) Umbrella sampling shows a continuous phase transition. (D) Location of free energy minima extracted from umbrella sampling simulations as a function of $\alpha_{a,c}$. Reproduced from publication [21].
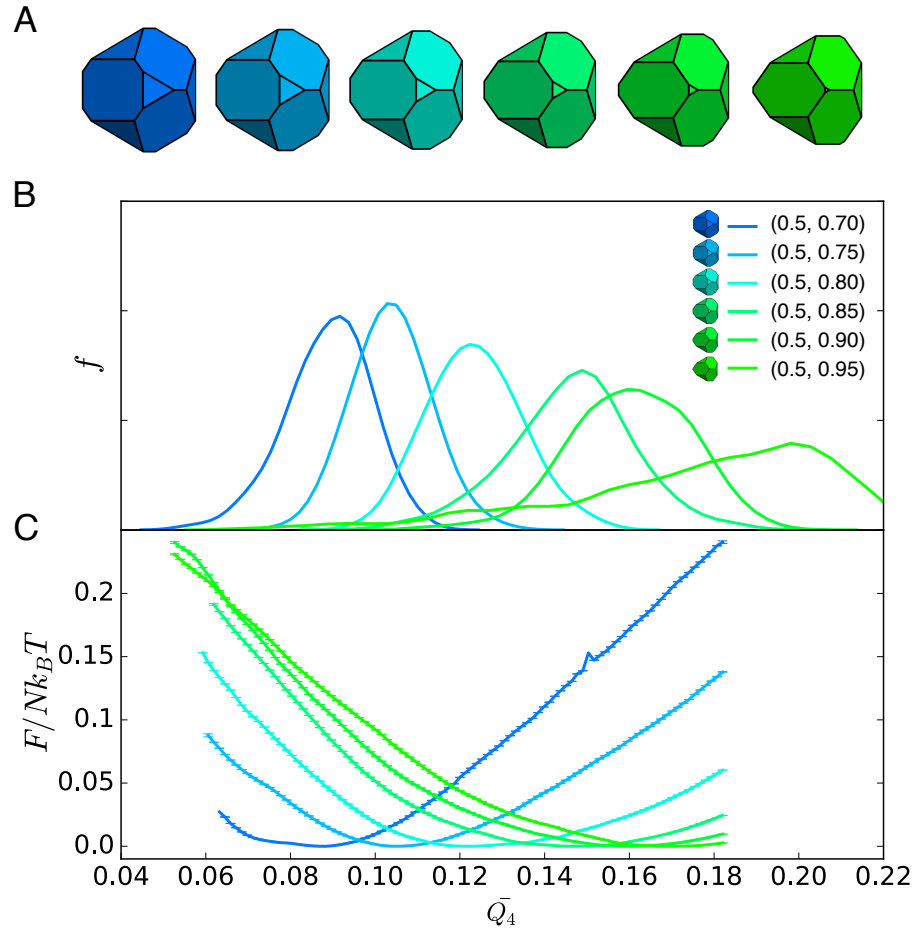
Figure 3.10: Shape-induced structural BCC↔SC reonfiguration occurs continuously in spheric tri-angle invariant hard polyhedra. (A) Sample shapes used in umbrella sampling simulation from the start to end in equal space. C shows all shapes. (B) Second neighbor-averaged $l = 4$ spherical harmonic order parameter $\overline{Q}_4$ shows a series of structures between BCC and SC. (C) Umbrella sampling shows a continuous phase transition. Reproduced from publication [21].
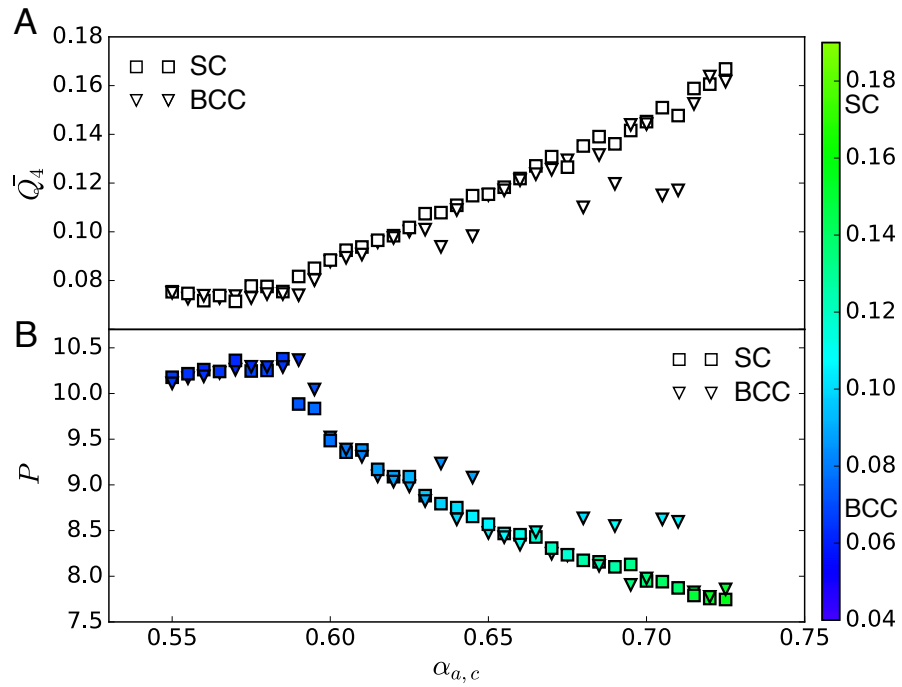
Figure 3.11: BCC↔SC phse transition is a continuous (i.e., second- or higher-order) thermodynamic phase transition. (A) Order parameter $\overline{Q}_4$ vs. shape suggests the derivative of the order parameter changes discontinuously near $\alpha_{a,c} = 0.6$. (B) $P(\alpha_a, \alpha_c)$ also indicates a discontinuous derivative near $\alpha_{a,c}$, which is consistent with a continuous phase transition. Reproduced from publication [21].
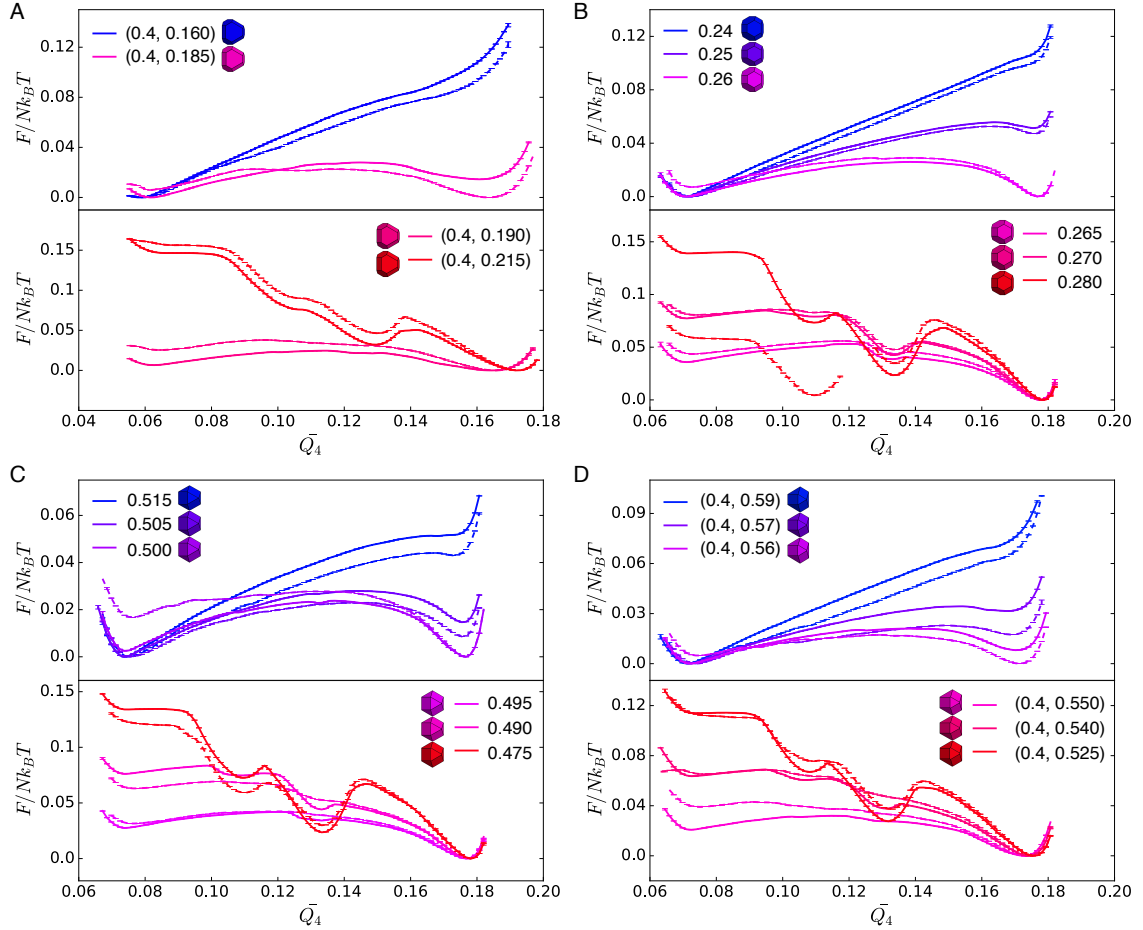
Figure 3.12: Shape-driven solid–solid FCC↔BCC reconfiguration is accompanied by a first-order thermodynamic phase transition in spheric-triangle invariant hard polyhedra, shown here with both BCC (solid line) and FCC (dashed line) initialization. Differences between curves indicate systematic errors in computing the location of the transition, but indicate that the thermodynamic nature of the transition is robust. (A): free energy curves of hard polyhedra as in Fig. 3.8. (B): free energy curves of hard polyhedra as in Fig. 3.6 (gap in red dotted line indicates insufficient statistics in one umbrella sampling window). (C): free energy curves of hard polyhedra as in Fig. 3.7. (D): free energy curves of hard polyhedra as in Fig. 3.5. Reproduced from publication [21].
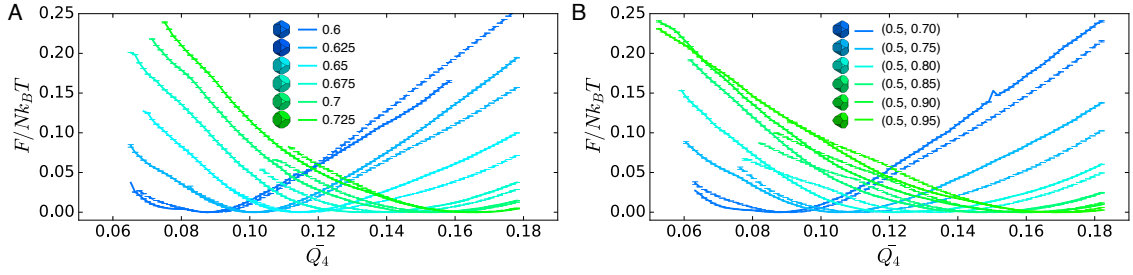
Figure 3.13: Shape-driven solid–solid BCC↔SC reconfiguration occurs continuously by continuous transition in spheric-triangle invariant hard polyhedra, shown here with both BCC (solid line) and SC (dashed line) system initialization. Differences between curves indicate systematic errors in the computing of the location of the transition, but indicate the thermodynamic is robust. (A): free energy curves of hard polyhedra as Fig. 3.9. (B): free energy curves of hard polyhedra as Fig. 3.10. Reproduced from publication [21].
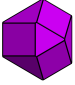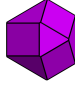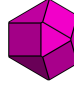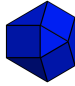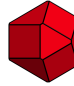
Figure 3.14: Shape-driven solid–solid reconfiguration and self-assembly timescales for BCC, FCC, and SC structures. Thermodynamically discontinuous FCC↔BCC solid–solid phase transitions occur dynamically in MC simulations on timescales ($\tau \lesssim 10^7$ MC sweeps) that are similar to self-assembly timescales ($\tau \approx 10^6$ MC sweeps) beyond the metastable region. In the metastable region, solid–solid reconfiguration does not occur on timescales ($\tau \gg 10^7$ MC sweeps) that are much longer than typical self-assembly times. Thermodynamically continuous BCC↔SC solid–solid phase transitions occur dynamically in MC simulations on timescales ($\tau \lesssim 10^6$ MC sweeps) that are comparable with or less than typical self-assembly times. Reproduced from publication [21].

CHAPTER IV

Thermodynamic Properties of BCC↔FCC Transitions in Hard Polyhedron Systems

In Ch. III we showed that for shape driven solid–solid phase transitions, both first and second order phase transitions can happen, despite the fact that the two final structures do not have a symmetry–sub-symmetry relationship. We found that the BCC↔SC transition actually consists of two second-order phase transitions, where the intermediate structures have sub-symmetry groups to both BCC and SC. A natural question to ask following that is can we find a second-order FCC↔BCC transition induced by changing particle shape? Since the sub-symmetry structure body-centered tetragonal (BCT) to both BCC and FCC is already known [6], we hypothesize there should exist a pathway where such transitions can be second order.

In this chapter we examine FCC↔BCC transitions in two different shape families, where one is the spheric triangle invariant 432 family ($\Delta_{4,3,2}$) [11] and the other one is concave, dimpled, "lock-and-key" particles [69, 35, 57, 58, 18, 68, 89, 3]. We found that in both shape families, the FCC↔BCC transitions are first order, where the intermediate BCT phase is never thermodynamically stable since these particles are spherical in the sense that they are not prolate or oblate. The contents of this chapter are taken from my co-first author paper, "FCC↔BCC phase transitions in colloidal crystals of convex and concave particles", Duanduan Wan, Chrisy Xiyu Du, Greg van

Anders, and Sharon C. Glotzer, in preparation [88]. I set up all the simulation and provided guidance on simulation details and which systems to include. Duanduan Wan performed the simulations. All authors contributed to the analysis of the data, discussion of the results and manuscript writing.
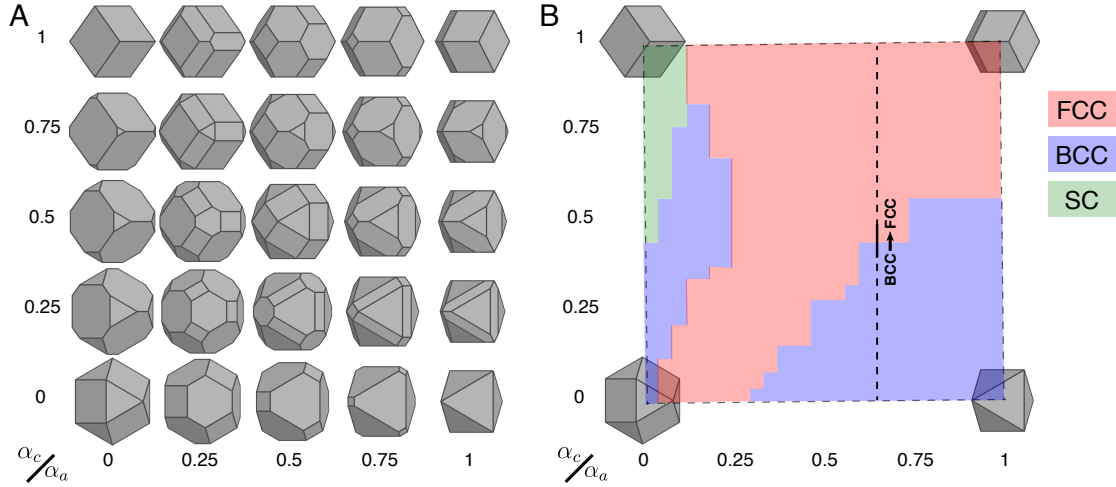
Figure 4.1: (A) Spheric triangle invariant (Δ_{432}) polyhedra form a continuous two-parameter (α_a, α_c) family of symmetric convex shapes that are bounded by the cubooctahedron [$(\alpha_a, \alpha_c) = (0, 0)$], octahedron $(0, 1)$, cube $(1, 0)$, and rhombic dodecahedron $(1, 1)$. (B) The colors indicate the self-assembled structures at $\eta = 0.55$, where FCC is red, BCC is blue, and SC is green. The self-assembled phases indicated are an approximated representation from the actual self-assembled phases. Reproduced from manuscript [88].
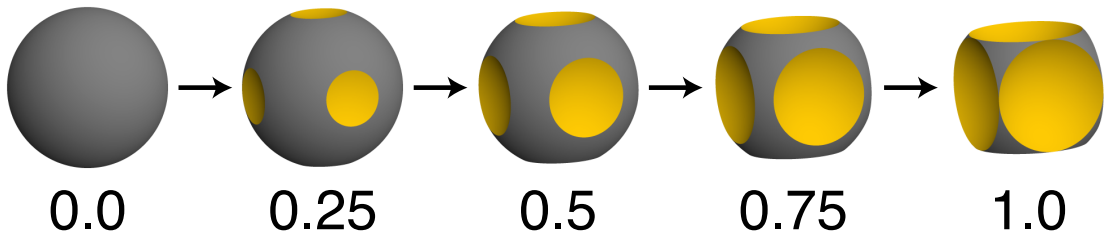
Figure 4.2: Dimpled particles with six valence "dimples" of different size. Figure shows shape change from a perfect sphere ($f = 0$) to the maximum dimple ($f = 1$). Reproduced from manuscript [88].

4.1 Model and Simulation Details

Using similar methods described in Ch. III, we use both the **Ehrenfest** and **Landau** approaches to study the phase transitions in shape family Δ_{432} (Fig. 4.1A shows shapes) and dimpled particles with six dimples of varying size (Fig. 4.2). For Δ_{432}, we use two shape parameters (α_a, α_c) to represent every shape in the shape family. Both parameters are within the range of $[0, 1]$. α_a represents the amount of vertex truncation and α_c represents the amount of edge truncation. $(\alpha_a, \alpha_c) = (1, 0)$ represents an octahedron; $(\alpha_a, \alpha_c) = (0, 1)$ represents a cube; $(\alpha_a, \alpha_c) = (0, 0)$ represents a cubooctahedron; $(\alpha_a, \alpha_c) = (1, 1)$ represents a rhombic dodecahedron.

For the dimpled particles, a dimple is a spherical cap bounded by the intersection of a central sphere with a valence sphere following [3]. Here we use shapes where the central sphere and valence spheres are of the same radius r, with six valence spheres in the $(\pm 1, 0, 0), (0, \pm 1, 0)$, and $(0, 0, \pm 1)$ directions. The dimple size is a function of the distance l between the central sphere and valence sphere, with $l = 2r$ when the two spheres just touch each other and the central sphere has no dimple and $l = \sqrt{2}r$ as the maximum dimple size, where the two neighboring dimples touch each other. We define scale free shape parameter $f = ((2r)^2 - l^2)/(\sqrt{2}r)^2$ for these dimpled particles, where $f = 0$ being a perfect sphere and $f = 1$ being a concave shape with maximum dimple size (see Fig. 4.2).

Some of the shapes in these two shape families have been synthesized at the colloidal scale and previous simulations have shown thermodynamic stability for a number of different bulk structures. Here, we study only the BCC and FCC regions that are adjacent to each other in shape space. All shapes are scaled to have unit volume. See Fig. 4.3 for examples of self assembled structures of both Δ_{432} and

dimpled spheres.

Since no direct method has been reported to compute pressure for hard concave particles, we only performed pressure analysis for shapes in Δ_{432}. We initialized systems using shapes with $\alpha_a = 0.65$, $\alpha_c \in [0, 1]$ in perfect BCC ($N = 2000$) and FCC ($N = 2048$) structures at packing fraction $\eta = 0.55$ and computed $P(\alpha_a, \alpha_c)$ (Fig. 4.4) after 1.5×10^7 MC steps to ensure that systems have reached equilibrium.

For both convex and concave shape families, we computed Landau free energies using umbrella sampling [82] and the weighted histogram analysis method (WHAM) [43] using $\overline{Q_4}$ as the order parameter. The spring constant of the biased potentials is set to $k = 3.5 \times 10^4$ and the window width of $\overline{Q_4}$ is set to 0.004 with 5×10^4 samples taken for each window. The free energy is computed as an average of five replicates.

4.2 Results

Δ_{432} Family of Hard Polyhedra

Fig. 4.4 shows the pressure shape constitutive relation $P(\alpha_a, \alpha_c)$ along the line of $\alpha_a = 0.65$ (Fig. 4.1B). At the FCC$\leftrightarrow$BCC cross-over, we find that $P(\alpha_a, \alpha_c)$ exhibits a discontinuous first derivative, indicating a phase transition that is either first or second order in the Ehrenfest classification [30]. Following the same procedure in Ch. III, we compute the Landau free energy near the transition boundary. From Fig. 4.5, it can be seen that at $\alpha_c = 0.32$, the system has the lowest free energy in the BCC basin. As α_c increases, the BCC basin rises while the FCC basin lowers, which indicates the system begins to prefer the FCC structure. The change in the location of the lowest free energy basin indicates this is a first order phase transition.

Dimpled Spheres

We then explore the FCC$\leftrightarrow$BCC transition in the system of dimpled spheres.

Based on the self-assembly behavior shown in Fig. 4.3, we know that when $f \lesssim 0.63$, particles tend to self-assemble into the FCC structure, and when $f \gtrsim 0.67$, particles tend to self-assemble into the BCC structure, which gradually changes into a SC structure as f increases beyond 0.7 (Fig. 4.3E, F). Similar to Fig. 4.5, Fig. 4.6 shows the Landau free energy curve of the dimpled sphere system. It has two basins corresponding to the BCC and FCC phases and demonstrates a first order phase transition in the Δ_{432} family. Additionally, we observe that the BCC basin shifts to the right of $\overline{Q}_4 = 0.07$ and shifts further as f increases due to the BCC↔SC transition. At $f = 0, 8$, the crystal that assembles is twinned SC (Fig. 4.3E, and as f further increases, the system gradually changes into a single domain SCphase (Fig. 4.3F).

4.3   Discussion

The existence of intermediate BCT structures between FCC and BCC [6] indicates that, according to Landau theory [8, 81] the FCC↔BCC transition could occur either *via* a pair of second order phase transitions or by a first order phase transition. In Ch. III, convex, 332-symmetric shapes indicated a first order phase transition. Here, we used the shape-dependent emergent valence of anisotropic colloids [84] in convex and concave 432-symmetric shapes in an attempt to manipulate the local structure of BCC and FCC to create intermediate BCT states following the so-called Bain path by elongating one of the three unit cell directions [6]. Instead, we found that the discontinuous nature of the transition persisted over all studied shape families. Despite the apparent insensitivity of the overall thermodynamics of the transition to particle valence modifications tested here, some discernible differences in the thermodynamics of the transitions were found. Whereas in the convex shape of both

332 and 432-symmetries show strong evidence of metastable mixed FCC-HCP stacking developing after the BCC$\rightarrow$FCC transition, this was not evident in our study of concave 432-symmetric shapes (dimpled spheres with 6 valence spheres). This finding indicates that choice of particle shape does afford some control over transition thermodynamics. Understanding the extent to which this is possible will be an important question for future work, given the growing number of examples of shape-shifting colloids that can now be synthesized [34, 93, 51, 31], the potential for the use of these colloids in developing materials, and the importance of the thermodynamics of solid–solid transitions in determining the viability of shape-shifting-driven structural reconfiguration.
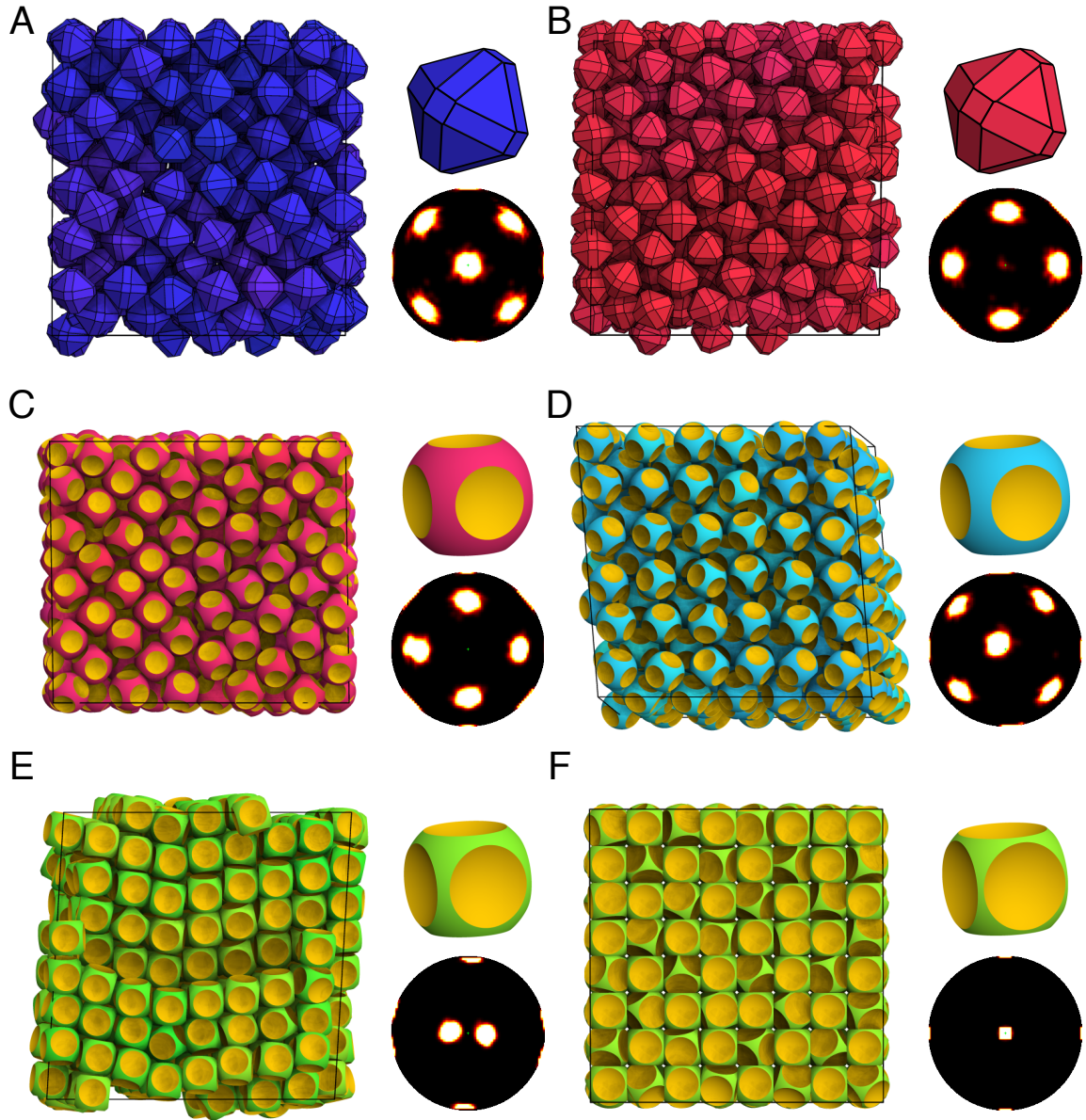
Figure 4.3: Sample self-assembled colloidal crystals formed by shapes in the Δ_{432} family of hard polyhedra and dimpled spheres, with images showing particle shape and bond order diagram. All systems are at density $\eta = 0.55$. (A) A BCC crystal self-assembled from shape $(\alpha_a, \alpha_c) = (0.65, 0.32)$. (B) An FCC crystal self-assembled from shape $(\alpha_a, \alpha_c) = (0.65, 0.40)$. (C) An FCC crystal self-assembled from dimpled sphere $f = 0.63$. (D) A sheared BCC crystal self-assembled from dimpled sphere $f = 0.67$. (E) A twin SC crystal self-assembled from dimpled sphere $f = 0.8$. (F) A SC crystal self-assembled from dimpled sphere $f = 0.9$. Note the similarity of shapes in A and B, and also in C and D; even small shape differences can affect the bulk self-assembly of hard polyhedra. Reproduced from manuscript [88].
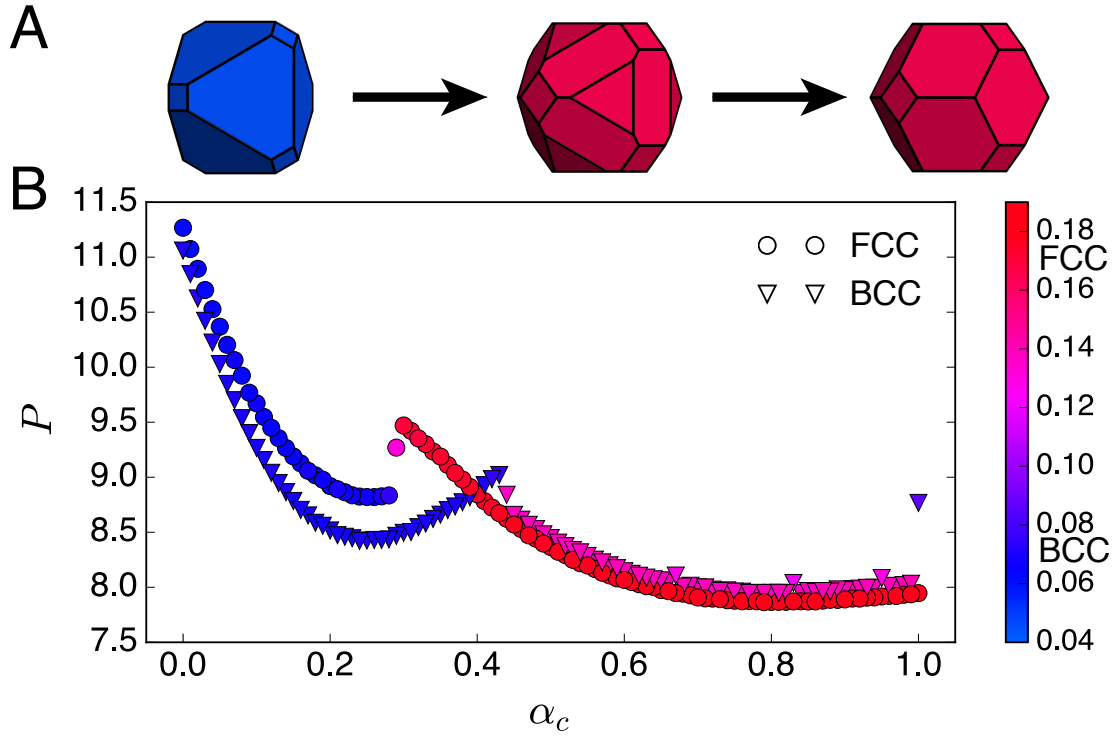
Figure 4.4: (A) Sample shapes studided along the line of constant $\alpha_a = 0.65$. Parameters for the three shapes are: $\alpha_c = 0.0$ (left), $\alpha_c = 0.5$ (middle), $\alpha_c = 1.0$ (right). (B) Pressure-shape constitutive relation at fixed $\alpha_a = 0.65$. Circles indicate FCC system initialization, and triangles indicate BCC system initialization. Marker colors indicate the value of the order parameter $\overline{Q_4}$ computed in the final structure of the system after equilibration. Errors are smaller than marker size. Reproduced from manuscript [88].
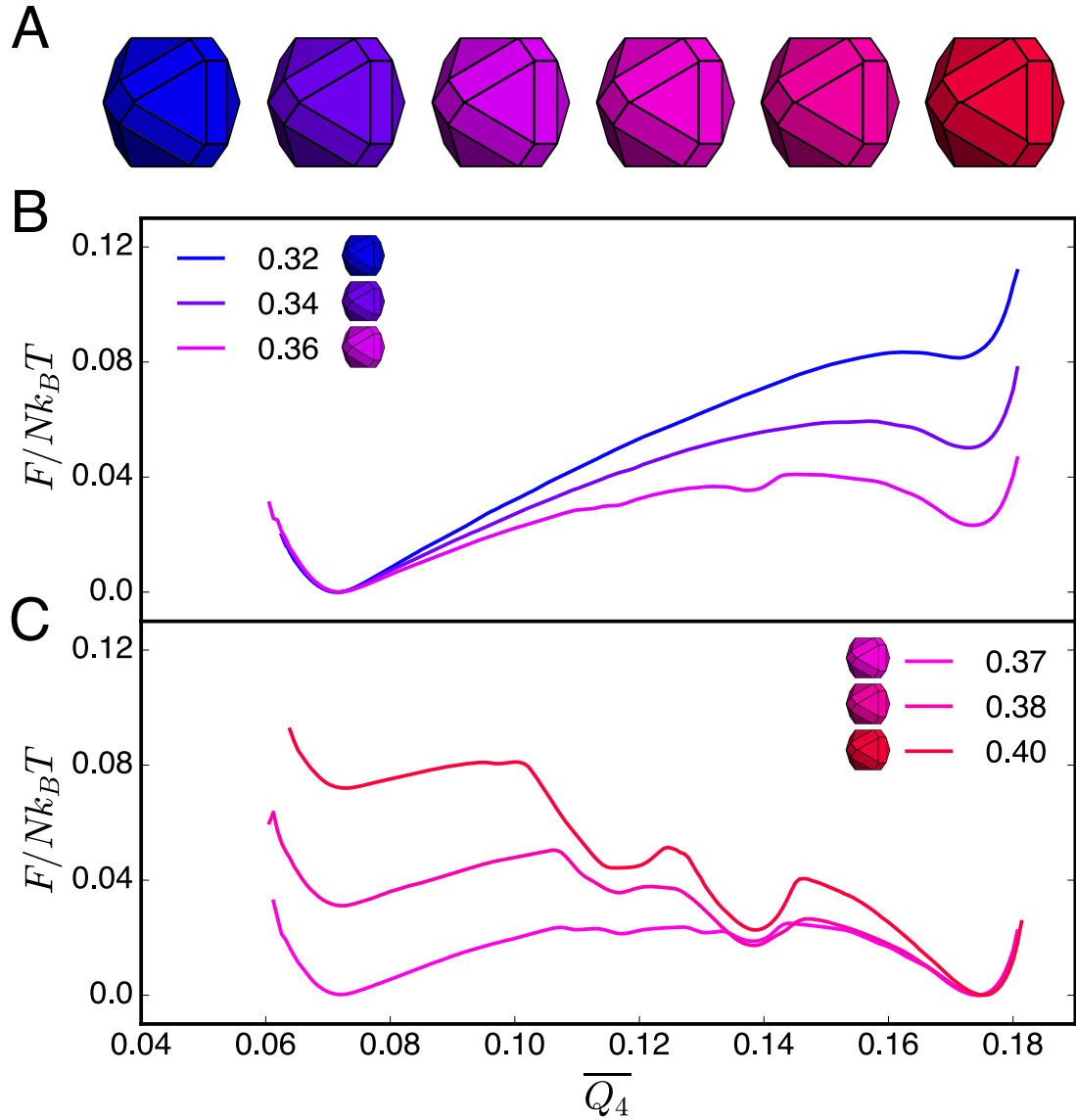
Figure 4.5: In Δ_{432} family of hard polyhedra, shape-induced structural FCC$\leftrightarrow$BCC reconfiguration is accompanied by a first-order thermodynamic phase transition. (A) Six shapes used to compute Landau free energy. (B) Landau free energy as a function of $\overline{Q_4}$ for left most three shapes that self assemble into BCC. (C) Landau free energy as a function of $\overline{Q_4}$ for right most three shapes that self assemble into FCC. Reproduced from manuscript [88].
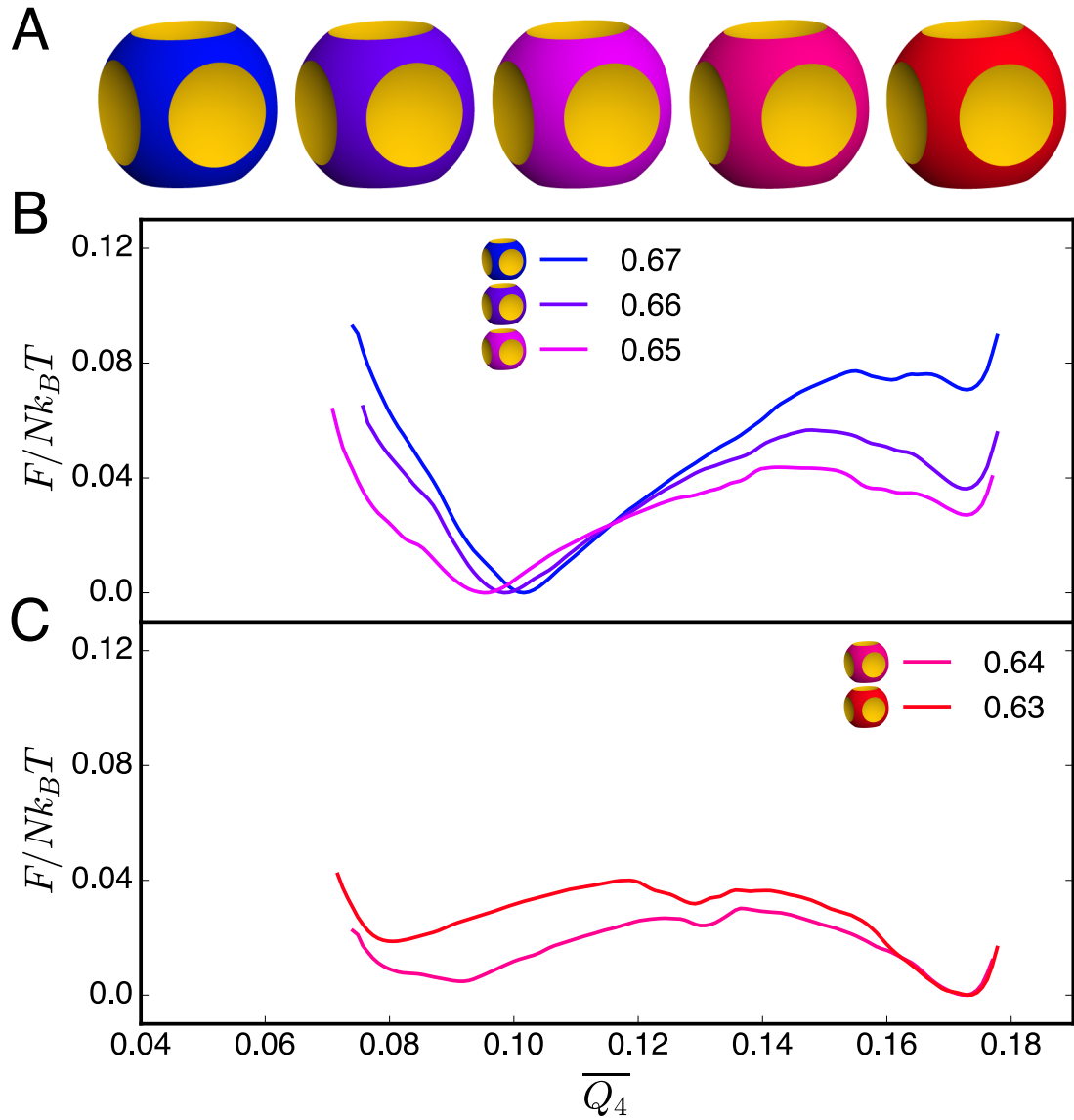
Figure 4.6: For dimpled spheres, shape-induced structural FCC↔BCC reconfiguration is accompanied by a first-order thermodynamic phase transition. (A) Five dimpled spheres used to compute Landau free energy. (B) Landau free energy as a function of $\overline{Q_4}$ for left most three dimpled spheres that self assemble into BCC. (C) Landau free energy as a function of $\overline{Q_4}$ for right most two shapes that self assemble into FCC. Reproduced from manuscript [88].

CHAPTER V

Transition Kinetics of Shape-Driven Solid–Solid Phase Transitions in Colloidal Crystals

In this work we study the kinetic behavior of shape-driven solid–solid phase transitions. Despite the wide range of applications of solid–solid transitions, some fundamental questions remain unanswered due to its nature, such as the kinetic pathways when structural transformation occurs. In general, kinetic pathways of solid–solid transitions are categorized into diffusional and diffusionless transformations [25]. In diffusional transformations, there is diffusive particle motion; in diffusionless transformations, there is cooperative displacement of all particles, such as the well known Martensitic transformation [25]. In the literature, "Martensitic" and "diffusionless" are used interchangeably in many cases. Past researchers have made many postulates about how Martensite grows [59, 39, 42, 7], but due to the length and time scales of such transformations, there is no definitive answer [62, 91, 87, 75].

Recent developments in colloidal materials synthesis have made colloidal systems viable models to investigate these kinetic questions. Using the same family of minimal model systems described in Ch. III, we investigate the kinetic pathway of two solid–solid transitionsL FCC↔BCC and BCC↔SC. We compare the similarity and differences of the kinetics of these two transitions, as they have different thermodynamic order [21]. In addition, we look at six different systems sized from 500 to

$1,000,000$ particles to understand the system-size dependence of the kinetic pathways.

The contents of this chapter are taken from my first author paper, "Kinetics of Shape-Driven Solid–Solid Transitions in Colloidal Crystals". Chrisy Xiyu Du, Greg van Anders, Joshua A. Anderson, and Sharon C. Glotzer, in preparation [19]. I performed all the simulation and analysis in this paper. All authors contributed to the discussion of results and manuscript writing.

5.1 Model and Simulation Details

In our study, we use shapes from the Δ_{332} (Fig. 3.1A) shape family, specifically particles near Line 4 (Fig. 3.1B) for FCC↔BCC transition and particles near Line 2 (Fig. 3.1B) for BCC↔SC transition. We took four different shapes ($\alpha_{a,c} = \{0.2, 0.225, 0.3, 0.325\}$) for FCC↔BCC transitions and two different shapes ($\alpha_{a,c} = \{0.6, 0.725\}$) for BCC↔SC transitions. We investigate more shapes for FCC↔BCC transitions to also compare the difference in transition time for shapes that are closer (further) away from the phase boundary.

For both FCC↔BCC and BCC↔SC transitions, we performed MC simulations for six different system sizes at packing fraction $\eta = 0.55$, which is chosen to be consistent with the studies reported in Ch. III. We set up the BCC (FCC)-forming particles in perfect FCC (BCC) structures, respectively, and perform NVT MC simulations with variation of box shape [16] until the system reaches equilibrium. We then analyze all the possible observables (pressure, mean square displacement, $\overline{Q_4}$, etc) as well as the transition rate and the transition pathway each simulation takes. All the simulations are done using HPMC [5] in HOOMD-blue [4], and we use units in which $k_{\mathrm{B}}T = 1$.

5.2 Results

FCC↔BCC The simplest pathway going from BCC to FCC and vice versa is provided by the Bain postulates [6]. Bain states that starting from either the cubic unit cell of BCC or FCC by elongating in one of the three unit vector directions continuously by $\sqrt{2}$, the unit cell will transform into FCC or BCC, respectively. For simplicity, here we define the system box aspect ratio to be c/a, where c represents the maximum box dimension and a represents the minimum box dimension upon checking that the middle box dimension $b \approx a$.

We first investigate the final box aspect ratio as a function of system size N (see Fig. 5.1). We note that as the system size increases, the simulation box is more likely to stay cubic during a transition from FCC to BCC or vice versa. In small system sizes, the aspect ratio of the box can be as high as $\sqrt{2}$, which is consistent with the Bain postulate. This indicates that in smaller systems, it is much more likely for all particles to have collective motion simultaneously towards one of the three possible elongation directions, while in a bigger system, collective motion is much harder.

This is further confirmed by analysis of $\overline{Q_4}$ as a function of box aspect ratio (Fig. 5.2, 5.3). We observe that for transition FCC→BCC, $\overline{Q_4}$ drops to around 0.12 before there is any change in the box aspect ratio for system size $N = 2048$ and $N = 4000$. This indicates that in the initial state, local structural rearrangement could occur without a global rearrangement in box shape; however, to complete the phase transition, some global rearrangement is needed. Unlike the smaller system size, for intermediate system sizes, $N = 6912$ and $N = 13500$, the simulation box dimensions do not change as much during the whole simulation while $\overline{Q_4}$ indicates that the phase transition is not complete. This behavior indicates that at intermediate system sizes,

while it is easier to make local rearrangements, it is still not enough to complete the whole phase transition, but due to the increase in system size, it becomes much harder to induce any global collective motion. At large system size, $N \approx 1,000,000$, the transition completes without any global collective motion (Fig. 5.4), which also indicates that the transformation between two phases of large system size and small system size follow different mechanism.

In the $N \approx 1,000,000$ simulation we compare the transition rate between two different shapes. We see that for transitions in both directions, the transition rate of the shape further away from the phase boundary is much faster than the one that is closer. This is consistent with phase transitions driven by other thermodynamic variables such as pressure. Here, too, transitions take longer from shape near structural boundaries than for shapes away from boundaries (Fig. 5.4).
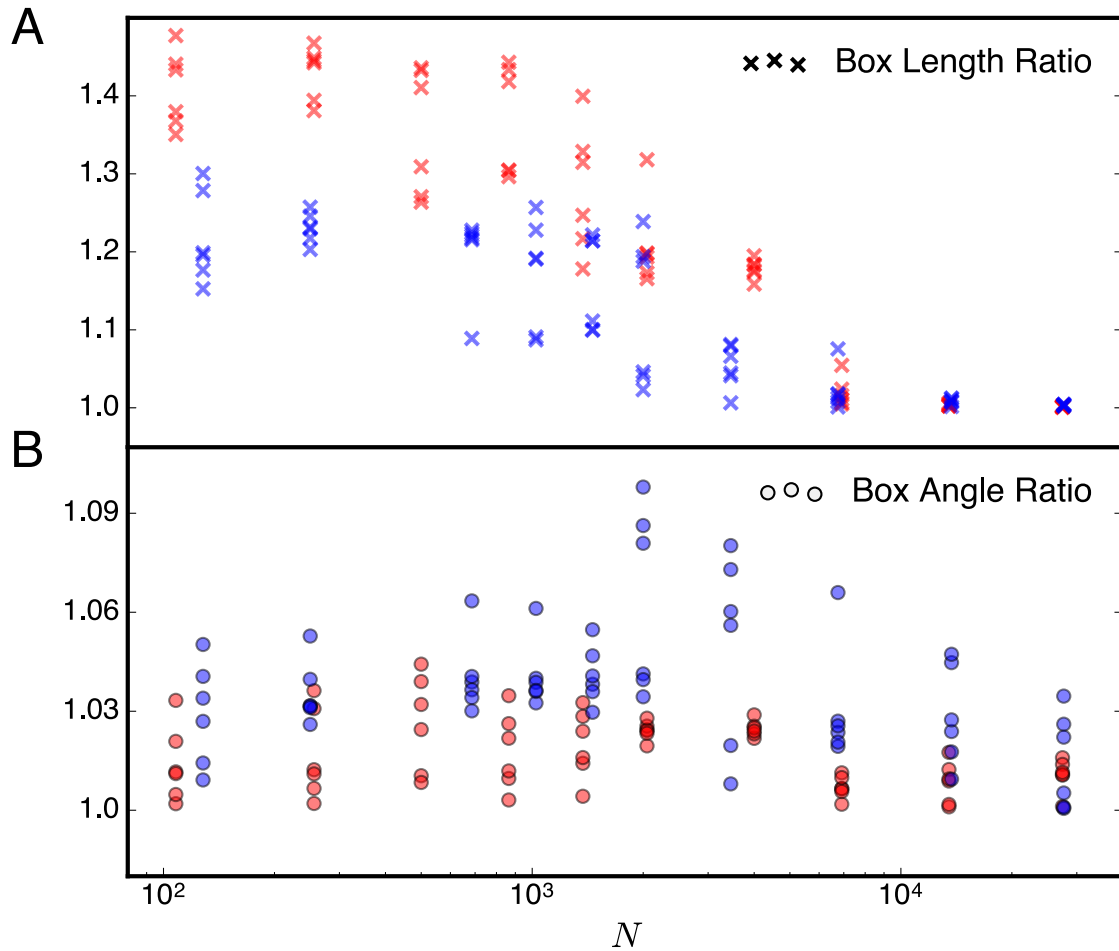
Figure 5.1: (A) Box aspect ratio as a function of system size N. All blue crosses indicate the initial structure of the system is BCC, while red crosses indicate the initial structure of the system is FCC. The plot shows a decreasing trend of the aspect ratio. For $N < 1000$, the final aspect ratio is very close to $\sqrt{2}$, while for $N > 10000$, the simulation box remains cubic. (B) Box angle ratio as a function of system size N. All blue circles indicate the initial structure of the system is BCC, while red circles indicate the initial structure of the system is FCC. The plot shows that despite system size, the simulation box remains orthrombic. Reproduced from manuscript [19].
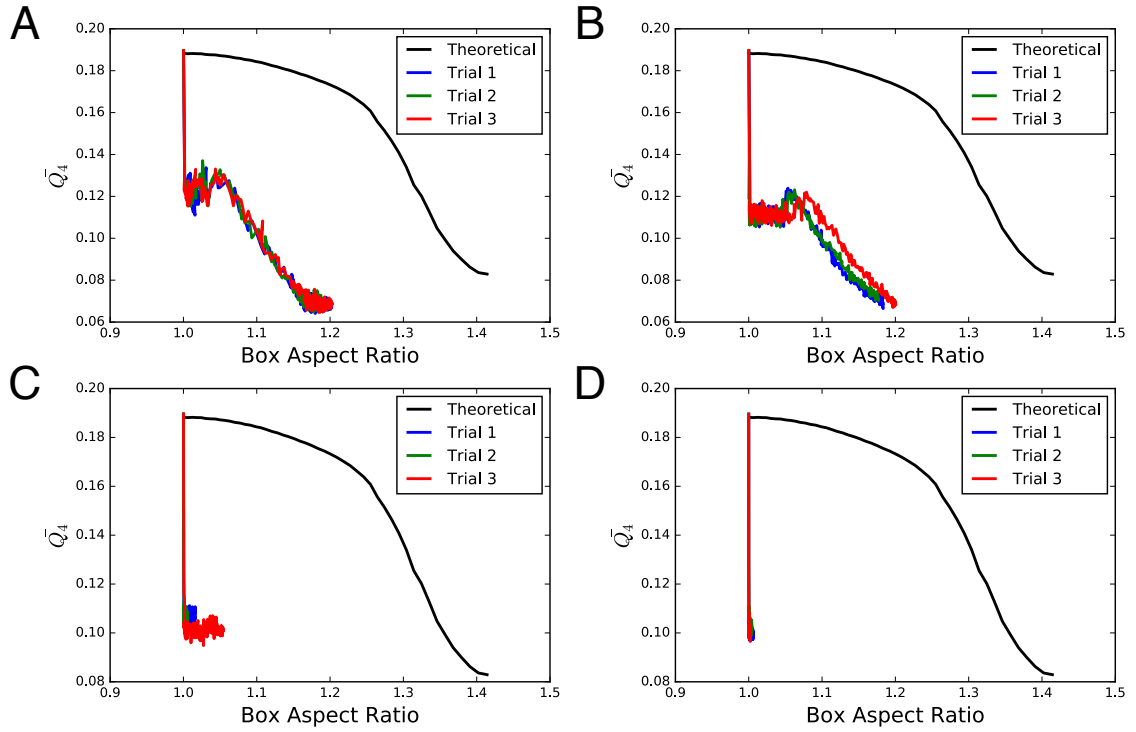
Figure 5.2: $\overline{Q_4}$ as a function of box aspect ratio for particle $\alpha_{a,c} = (0.2)$ going from FCC to BCC. All simulations have run 4×10^7 MC sweeps. Black line shows the $\overline{Q_4}$ evolution as a function of box aspect ratio if the system completely follows the Bain postulate. Blue, green and red lines show three independent replicates. (A) $N = 2048$, (B) $N = 4000$, (C) $N = 6912$, (D) $N = 13500$. Reproduced from manuscript [19].
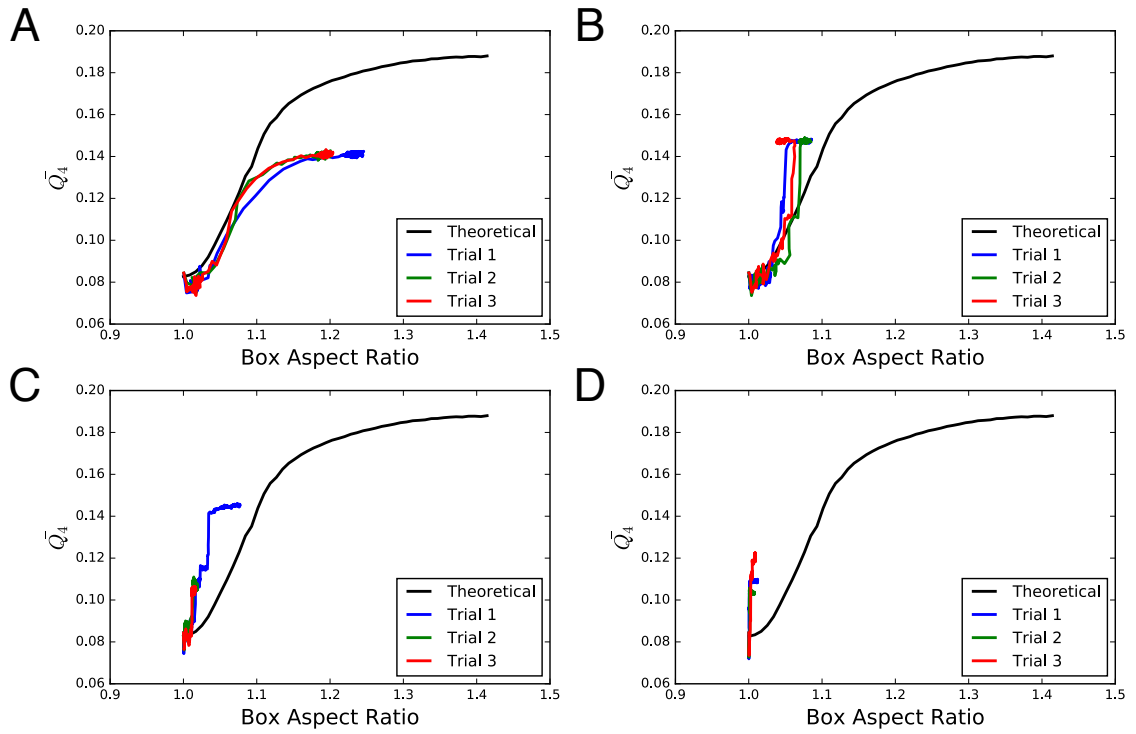
Figure 5.3: $\overline{Q_4}$ as a function of box aspect ratio for particle $\alpha_{a,c} = (0.3)$ going from BCC to FCC. All simulations have run 4×10^7 MC sweeps. Black line shows the $\overline{Q_4}$ evolution as a function of box aspect ratio if the system completely follows the Bain postulate. Blue, green and red lines show three independent replicates. (A) $N = 2000$, (B) $N = 3456$, (C) $N = 6750$, (D) $N = 13718$. Reproduced from manuscript [19].
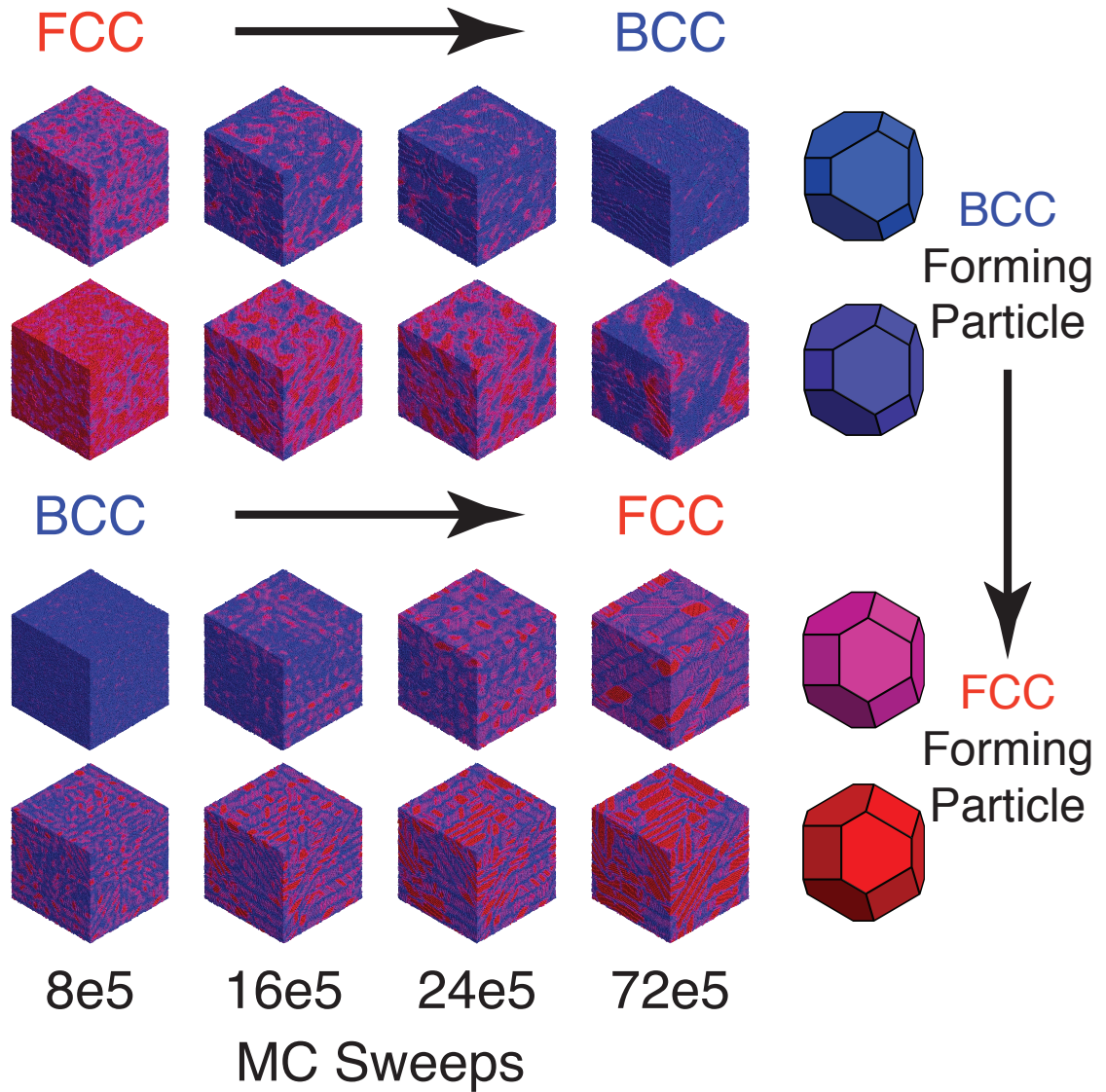
Figure 5.4: Snapshots of four simulations of particle shapes $\alpha_{a,c} = [0.2, 0.225, 0.3, 0.325]$ (top to bottom). The snapshots are taken at timestamps indicated at the bottom. It is notable that at big system sizes, the phase transitions occur on the order of 10^7 MC sweeps. Particles are colored by $\overline{Q_4}$ values. Reproduced from manuscript [19].

CHAPTER VI

Inverse Design of Pressure-Induced Solid–Solid Transitions in Colloids

In this work we introduce a coupled thermodynamic ensemble using the "digital alchemy" framework to design different pressure driven solid–solid phase transitions. The contents of this chapter are taken from, "Inverse Design of Pressure-Induced Solid–Solid Transitions in Colloid Crystals". Chrisy Xiyu Du, Greg van Anders, Julia Dshemuchadse, Paul M. Dodd, and Sharon C. Glotzer, in preparation [20]. I performed all the simulations and analysis in this paper. All authors contributed to the discussion of results and manuscript writing.

6.1 Introduction

In the previous chapters we discussed the potential of using shape shifting particles as building blocks for reconfigurable colloidal crystals. However, with current synthesis techniques, it is very hard to make particles with such precision. On the other hand, pressure is easily controlled in an experimental setting, but what building shape should we use? We seek to find a way to efficiently find targeted, pressure-induced solid–solid phase transitions for a single particle shape without having to map phase diagrams.

In order to design a phase transition behavior, we need to construct building blocks
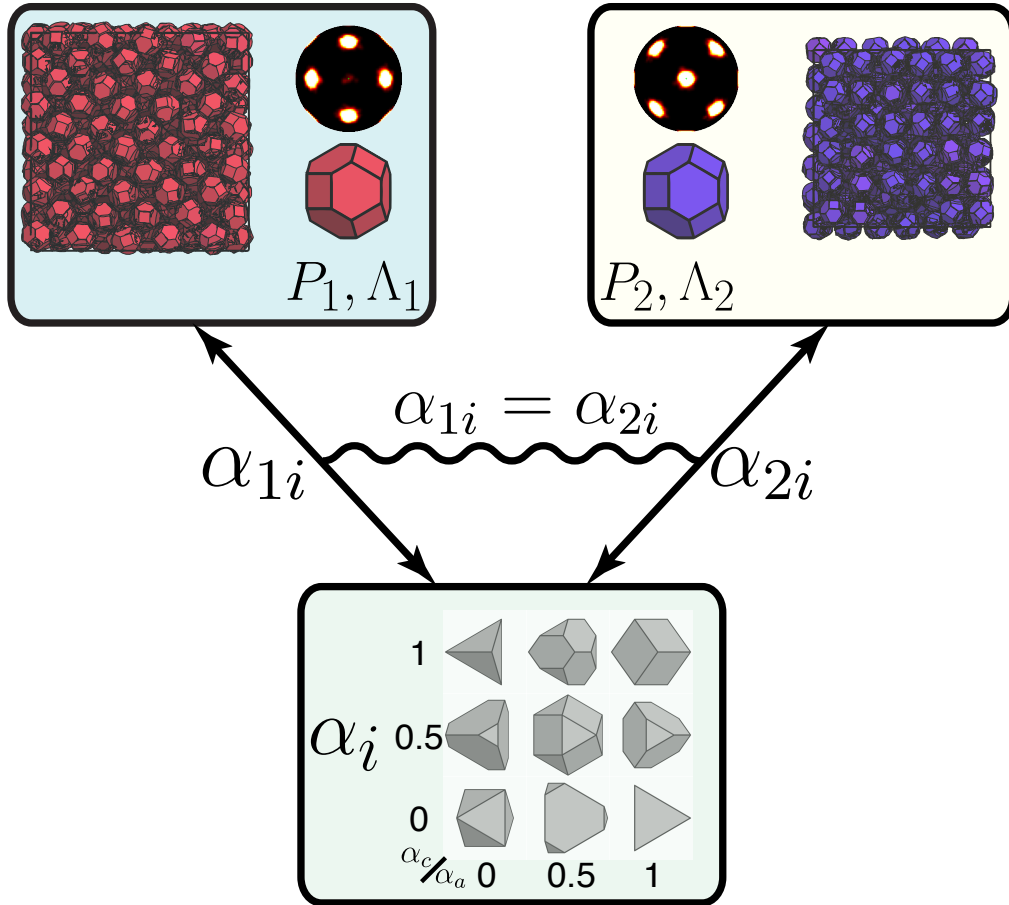
Figure 6.1: The simulation protocol, containing two simulation boxes with different crystal structures (Λ_1 and Λ_2) and different pressures (P_1 and P_2). Here, the two structures illustrated in the figure are FCC (red) and BCC (blue). Both simulation boxes are subjected to the same "shape bath" (shape attributes are denoted as α_i), where they can interact with each other and make synchronous moves in shape space with different constraints. Shape illustrated in the figure are subjected to spheric triangle group $\Delta_{3,3,2}$ (Fig. 3.1) [11]. Reproduced from manuscript [20].

that exhibit *multiple* target behaviors under a prescribed *set* of conditions. Here, we present an inverse design framework that couples multiple extended ensembles *via* the approach of "digital alchemy" [86] to design colloidal building blocks that exhibit multiple target behaviors under different thermodynamic conditions. Motivated by simulations [21, 65] and experiments [61, 54, 10, 96] demonstrating that solid–solid phase transitions (*e.g.,* FCC↔BCC, or BCC↔SC) can occur in colloidal systems under a range of circumstances, here we seek to *design* solid–solid transitions in

colloids. By performing computer simulations in which the shapes of anisotropic colloids are dictated by two distinct target structures at different pressures (Fig. 6.1), we design particles that undergo a solid–solid transition *in silico* between the two structures in a prescribed pressure range.

6.2 Model and Simulation Details

To design for a pressure-induced solid–solid phase transition, we aim to optimize the particle shape in two different system settings at the same time. As discussed in Ch. II, the general optimization framework is that of "Digital Alchemy" [86, 28], where the partition function was extended we extended to include the particle shape and design constraints:

$$(6.1) \qquad Z = \sum_{\sigma} e^{-\beta(H - \sum_i \mu_i N\alpha_i - \lambda\Lambda)}.$$

Here β is the inverse temperature, μ_i are so-called alchemical potentials that are thermodynamically conjugate to the alchemical parameters α_i, which describe particle shape, N is the number of particles in the system, Λ is the potential energy function for an Einstein crystal of the target structure, λ is the spring constant of the Einstein crystal, and the sum is taken over particle coordinates and orientations and over the space of particle shapes. Here we want to satisfy two different system constraints simultaneously. As derived in Ch. II, our combined partition function for the two systems is

$$(6.2) \qquad \mathcal{Z} = \int [d\alpha_i] Z(N, P_1, T, \alpha_i, \Lambda_1) Z(N, P_2, T, \alpha_i, \Lambda_2).$$

Using this formalism, we consider two systems held at different pressures P_1 and P_2, with different structural constraints Λ_1 and Λ_2. Similar to designing particle shape for one structure [28], we make MC moves in particle shape, but we attempt identical particle shape moves in both systems simultaneously.

We studied two solid–solid transitions:FCC↔BCC BCC↔SC, FCC↔β-Tungsten (β-W) and BCC↔High Pressure Lithium (Li). at two different pressure differences. For each transition, the design process consists of two steps. In the first step, we initialized the two systems ($N \sim 500$), using the candidate phases with a randomly generated shape, and compressed both systems at the same time with MC shape moves to the target density; then we relaxed the structural constraint over 2×10^7 MC moves and collected data over another 2×10^7 MC moves. In the second step, we took the particles generated from step one and validated our method by performing self-assembly runs ($N \sim 2000$) at the lower-pressure phase, and then slowly compressed the system and expanded it to see if the solid–solid phase transition actually occurred.

6.3   Results

FCC↔BCC

We used four different shape constraints and two different density differences to design FCC↔BCC transitions. We used the spheric triangle group $\Delta332$ (Fig. 6.3A) and $\Delta432$ (Fig. 6.5A) [11] and randomly generated convex polyhedra with 32 and 64 vertices (sample polyhedron can be found in Fig. 6.9), respectively. The two different density differences are simulated with FCC at $\phi = 0.55$, while BCC was set up at either $\phi = 0.60$ or $\phi = 0.65$. For each shape constraint and pressure difference, one optimal shape was determined for each pressure difference after averaging over five independent replicates. Result from $\Delta_{3,3,2}$ and the pressure difference $\phi = (0.55, 0.65)$ is shown in Fig. 6.2, and pressure difference $\phi = (0.55, 0.60)$ is shown in Fig. 6.3B. Result from $\Delta_{4,3,2}$ and the pressure difference $\phi = (0.55, 0.65)$ is shown in Fig. 6.5C, and pressure difference $\phi = (0.55, 0.60)$ is shown in Fig. 6.5D.

All five independent replicates converged to the same shapes, as quantified by the

two shape parameters α_a and α_c. We also obtained the optimal shape for FCC and BCC alone at their respective densities (Fig. 6.2B, 6.3B). The "combined" optimal shape is located between the optimal shapes of FCC and BCC, but notably is not equidistant from both optimal shapes. This demonstrates that finding the optimal shape for a coupled system is not a matter of simply averaging the two optimal shapes from the two different phases.

As validation of our predicted optimal combined shape, we checked that a system consisting of these shapes can indeed undergo the pressure-induced solid–solid phase transition. We initialized the system using the optimal shape arranged into the FCC structure, thermalized it, and then slowly compressed the simulation box. We observed the phase transition from FCC to BCC and *vice versa* (Fig. 6.2D). As demonstrated in Fig. 6.2D, the process is reversible.

BCC↔SC

We used three different shape constraints and two different density differences to design a BCC↔SC transition. We used spheric triangle group Δ_{432} (Fig. 6.5A) and randomly generated convex polyhedra with 32 and 64 vertices (sample polyhedra can be found in Fig. 6.9), respectively. The two different density differences were chosen with BCC at $\phi = 0.55$ and with SC at either $\phi = 0.65$ or $\phi = 0.70$. For each shape constraint and pressure difference, one optimal shape was determined for each pressure difference after averaging over five independent replicates. Results from $\Delta_{4,3,2}$ and the pressure difference $\phi = (0.55, 0.70)$ is shown in Fig. 6.4, and pressure difference $\phi = (0.55, 0.65)$ is shown in Fig. 6.5B.

All five independent replicates converged to the same shape, as quantified by the two shape parameters α_a and α_c. We also obtained the optimal shape for BCC and SC alone at their respective densities (Fig. 6.4B, 6.5B). The combined optimal shape

lies much closer in shape space to the optimal shape of SC, which is also closer to a region in shape space where BCC self-assembles, while not being the optimal shape for BCC.

We verified that the optimal shape can indeed undergo the pressure-induced solid–solid phase transition. We initialized the system using the optimal shape arranged into the BCC structure, thermalized it, and then slowly compressed the simulation box. We were able to observe the BCC↔SC phase transition in real time (Fig. 6.4D). As demonstrated in Fig. 6.4D, the process is reversible.

BCC↔Li

We used three different shape constraints and three different density differences to design a BCC↔Li transition. We used spheric triangle group Δ_{332} (Fig. 6.3A) and randomly generated convex polyhedra with 32 and 64 vertices, respectively. The three different density differences were chosen with BCC at either $\phi = 0.55$ or $\phi = 0.60$ and with Li at either $\phi = 0.65$ or $\phi = 0.70$. For each shape constraint and pressure difference, one optimal shape was determined after averaging over five independent replicas. Results from Δ_{332} and the pressure difference $\phi = (0.55, 0.70)$ are shown in Fig. 6.6.

All five independent replicas converged to the same shape, as quantified by the two shape parameters α_a and α_c. We also obtained the optimal shape for BCC and Li alone at their respective densities (Fig. 6.6B).

While verifying these results, we found that upon lowering the density, Li will indeed transition into BCC but the reverse cannot happen due to kinetic constraints. Instead, we developed another method to test the stability of the Li phase at high pressure. We initialized the system ($N \sim 4000$) using the optimal shape, arranged half of the particles in the Li structure and the other half in a dense liquid at four

different densities $\phi = 0.55, 0.60, 0.65, 0.70$. After equilibration, we observed that for $\phi = 0.55, 0.60$, all systems had transitioned into BCC, while for $\phi = 0.70$, all particles in the system had adopted the Li structure. For the intermediate density $\phi = 0.65$, we observed coexistence of BCC and Li. This result shows that, thermodynamically, Li is the more stable phase at higher pressure, which validates our method.

FCC↔β-W

Since the β-W phase was not reported for shapes in Δ_{332} and Δ_{432}, we only performed simulation using randomly generated convex polyhedra with 32 and 64 vertices, respectively. The two different density differences were chosen with FCC at $\phi = 0.55$ and with β-W at either $\phi = 0.60$ or $\phi = 0.65$. An example shape is presented in Fig. 6.7A for $\phi = (0.55, 0.65)$, while Fig. 6.7B shows the symmetry analysis of all ten shapes obtained from the independent runs with 32 and 64 vertices. Fig. 6.7B shows that all shapes have converged to similar symmetries, consistent with the behavior of shapes in Δ_{332} and Δ_{432}.

In verifying our findings, we observed that the kinetic pathways are prohibited for both lowering and increasing the pressure. Similar to BCC↔Li, we initialized the system ($N \sim 4000$) using the optimal shape with half of the particles arranged into the β-W structure and the other half in a dense liquid at three different densities $\phi = 0.55, 0.60, 0.65$. After equilibration, we observed that for $\phi = 0.55$, all systems had transitioned into FCC while for $\phi = 0.65$, all systems had fully adopted the β-W structure. For the intermediate density $\phi = 0.60$, we observed coexistence of the FCC and β-W. This result shows that, thermodynamically, β-W is the more stable phase at higher pressure, which validates our method.

Shape Symmetry Analysis

In order to compare the results from shape families and generalized convex shapes,

we developed a shape descriptor S_l inspired by the local bond order parameter Q_l [79]. The order parameter is calculated as follows:

(6.3)
$$S_{ilm} = Y_{lm}(\theta(\vec{n_i}), \phi(\vec{n_i})),$$

where i denotes the i-th face of the convex polyhedron, $\vec{n_i}$ denotes the normal vector of the i-th face, and Y_{lm} is the spherical harmonic special function.

(6.4)
$$\overline{S_{lm}} = \frac{1}{N} \sum_{i=1}^{N} A_i S_{ilm},$$

where N denotes the total number of faces of the convex polyhedron and A_i denotes the area of the i-th face. Since we want the order parameter to be rotationally invariant, we sum over all S_{lm} values and normalize the result:

(6.5)
$$S_l = \left[\frac{4\pi}{2l+1} \sum_{m=-l}^{l} |\overline{S_{lm}}|^2 \right]^{1/2}.$$

Using this order parameter, we are able to compare shapes across different constraints. Fig. 6.8 shows the order parameter distribution of the transitions FCC↔BCC and BCC↔SC. Fig. 6.7B shows the order parameter distribution of the transition FCC↔β-W. We see that, in general, shapes share the same order parameter distribution under the same pressure and structural constraints, which means that the design method not only works for special shapes, but is also functional for systems with fewer constraints.

6.4 Discussion

Here, we showed that extending the "digital alchemy" framework [86, 28] to multiple coupled ensembles enables the design of anisotropic colloidal building blocks that exhibit two distinct target behaviors under corresponding distinct, pre-specified external conditions. In doing so we determined particle shapes that undergo pressure-induced solid–solid transitions in a target pressure range.

We have designed four sets of transitions and we observed spontaneous reversible transitions between the two phases for two of them (FCC↔BCC, BCC↔SC), while we could not observe the same behavior for the other two transitions (BCC↔Li, FCC↔β-W) even though they are thermodynamically stable. This is not surprising since the method is based on finding thermodynamics equilibria: our method finds the desired particle feature for the constraints, but does not guarantee that a viable pathway between the two structures exists.

The example transitions we induced were engineered in Alch-MC simulations [28], in which the structural constraints were relaxed (*i.e.*, set to zero) after particle shapes converged to (at least meta-)stable free energy basins. We would not expect that, in general, one could engineer more complex behaviors without employing structural constraints.

For the cases we studied, we found that maintaining the structural constraints resulted in small differences in particle shape that did not affect the success of the design of the pressure-induced solid–solid transitions. We expect that, in general, designing for more complex behaviors will require retaining structural constraints.

Although our investigations here focused on designing particle shapes for pressure-induced reconfiguration in colloids, this approach generalizes straightforwardly to, *e.g.*, shape-change-induced transitions [21]. Shape-shifting colloids have been synthesized using a number of techniques such as asymmetric thermal expansion [45], stimulated dewetting [94], and "colloidal recycling" [49], and we expect that inverse design approaches will be useful in the rational design of functional materials that leverage those synthesis techniques.
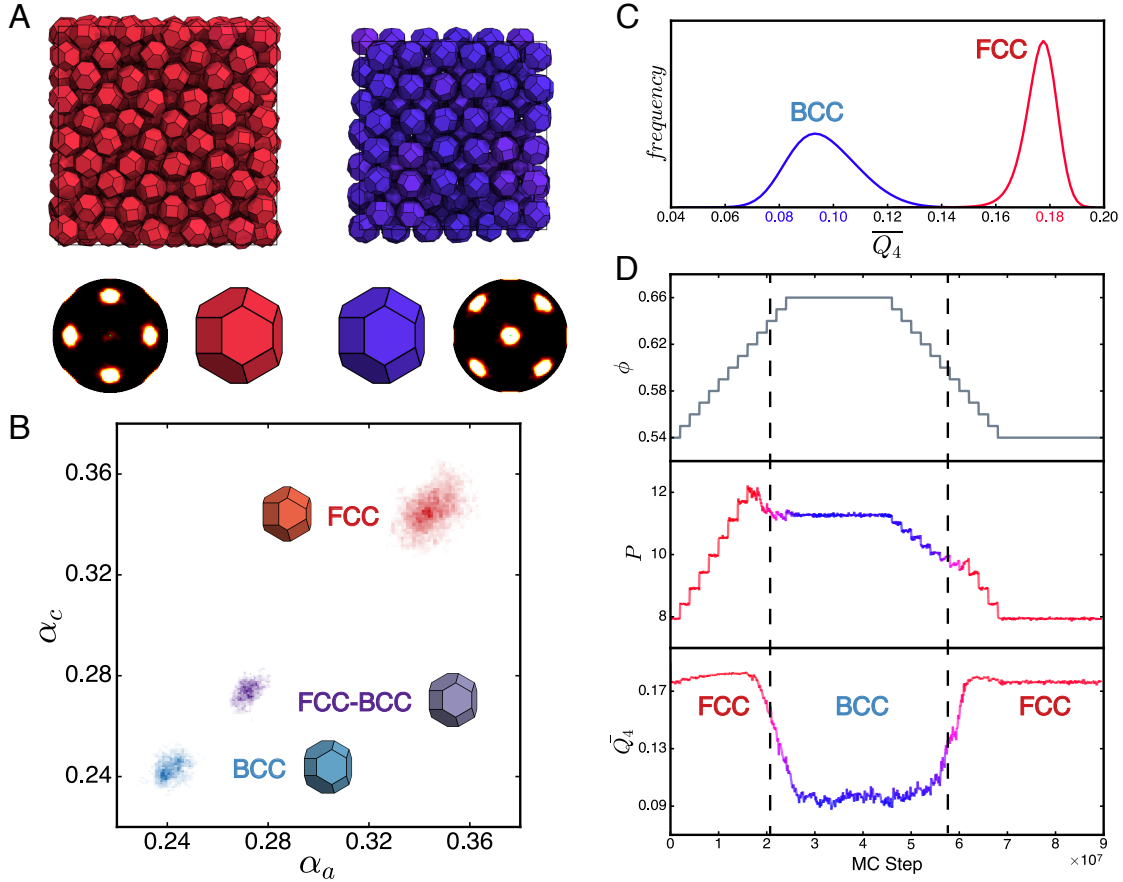
Figure 6.2: A Snapshots of the simulation setup: two simulation boxes of structure FCC (red, $\phi = 0.55$) and BCC (blue, $\phi = 0.65$), bond-orientational order diagrams indicating the structures, and magnified particles to depict their (identical) shape. B Heat map for the shape distribution for the optimal FCC shape (red, $\phi = 0.55$), BCC shape (blue, $\phi = 0.65$), and combined shape (purple, with FCC box at $\phi = 0.55$ and BCC box at $\phi = 0.65$). C Steinhardt order parameter distribution for FCC, BCC, and HCP. D Validation of the optimal shape reconfigurability. We initialize the system with FCC structure at $\phi = 0.54$ and slowly compress the system to $\phi = 0.66$. The top panel indicated the density of the system as a function of MC steps. The middle panel shows the measured pressure of the system. The color of the line indicates the structure of they system, where red is FCC and blue is BCC. The bottom panel shows the change in order parameter. Reproduced from manuscript [20].
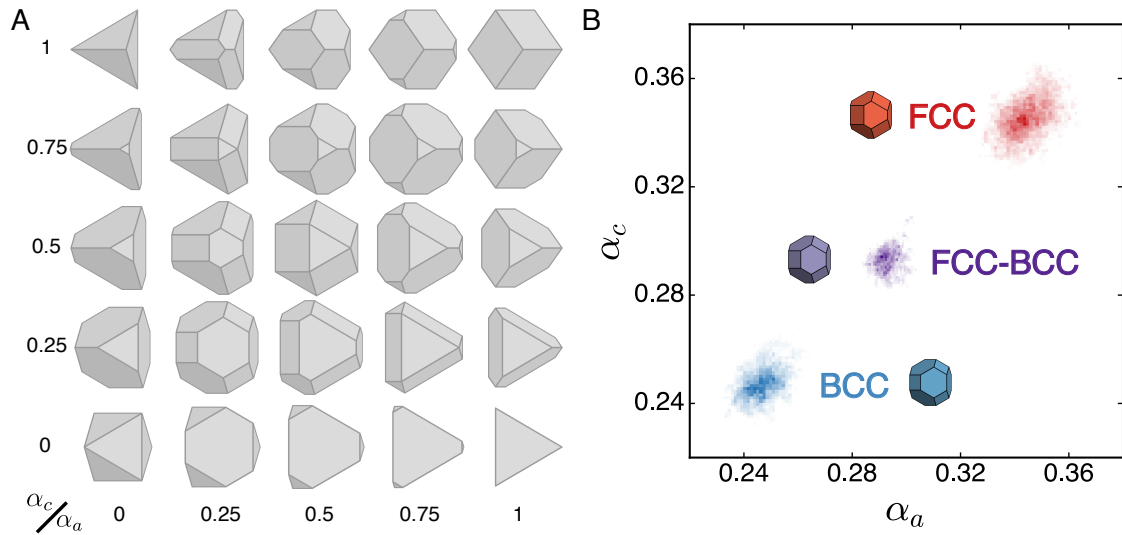
Figure 6.3: A Shape family Spheric-triangle invariant (Δ_{332}) polyhedra parametrized by a continuous two-parameter (α_a, α_c). This family of symmetric convex shapes are bounded by the octahedron ((α_a, α_c) = (0,0))), tetrahedron ((0, 1) and (1, 0)) and cube (1, 1). B Heat map for the shape distribution for the optimal FCC shape (red, $\phi = 0.55$), BCC shape (blue, $\phi = 0.60$), and combined shape (purple, with FCC box at $\phi = 0.55$ and BCC box at $\phi = 0.60$). Reproduced from manuscript [20]
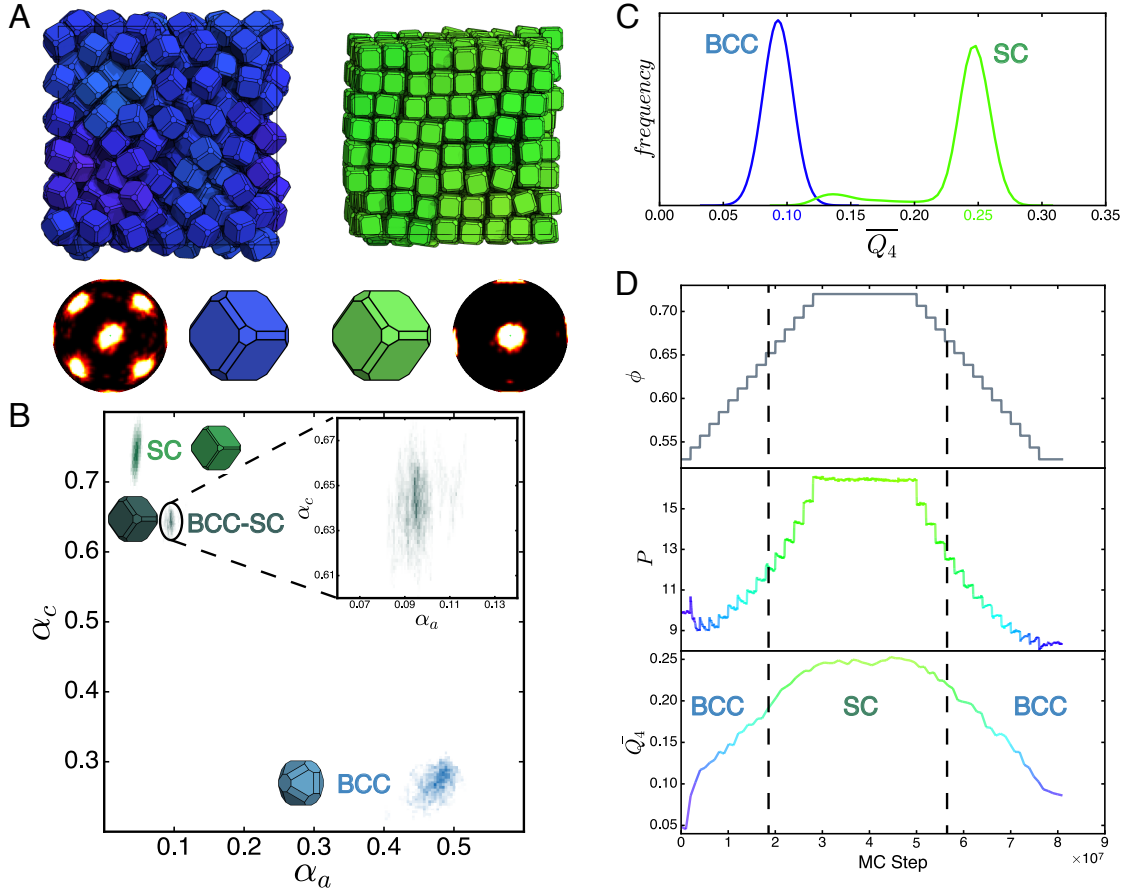
Figure 6.4: A snapshows of the simulation setup: two simulation boxes of structure BCC (blue, $\phi = 0.55$) and SC(green, $\phi = 0.70$), the bond-orientational order diagrams indicating the structures, and magnified particles to depict their (identical) shape. B Heat map for the shape distribution for the optimal BCC shape (blue, $\phi = 0.55$), SC shape (green, $\phi = 0.70$), and combined shape (dark green, with BCC box at $\phi = 0.55$ and SC box at $\phi = 0.70$). C Steinhardt order parameter distribution for BCC and SC. D Validation of the optimal shape reconfigurability. We initialize the system with BCC structure at $\phi = 0.54$ and slowly compress the system to $\phi = 0.72$. The top panel indicates the density of the system as a function of MC steps. The middle panel shows the measured pressure of the system. The color of the line indicates the structure of the system, where blue is BCC and green is SC. The bottom panel shows the change in order parameter. Reproduced from manuscript [20].
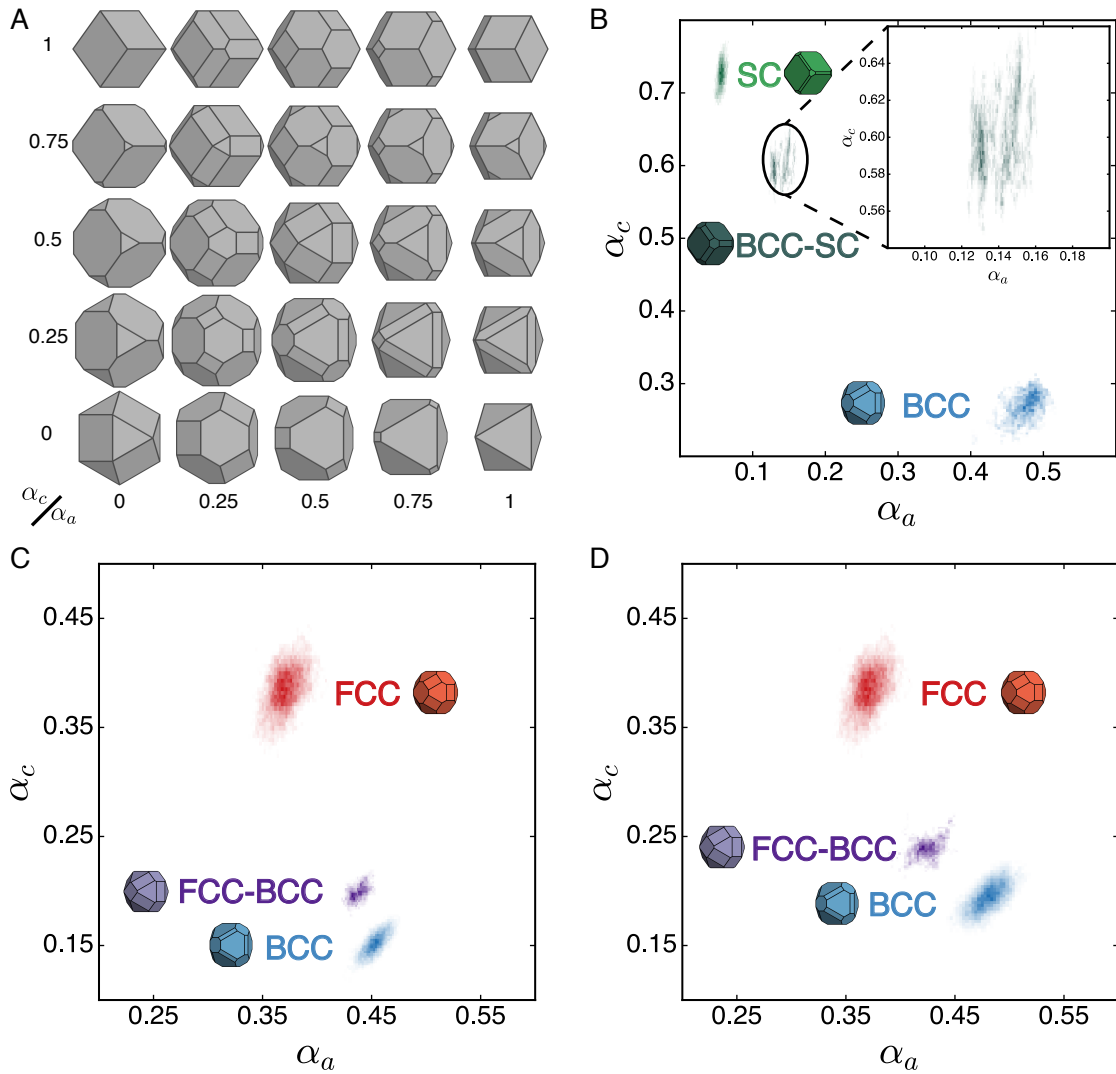
Figure 6.5: A Shape family Spheric-triangle invariant (Δ_{432}) polyhedra parametrized by a continuous two-parameter (α_a, α_c). This family of symmetric convex shapes are bounded by the cuboctahedron $((\alpha_a, \alpha_c) = (0,0))$, octahedron $(1, 0)$, cube $(0, 1)$ and rhombic dodecahedron $(1, 1)$. B Heat map for the shape distribution for the optimal BCC shape (blue, $\phi = 0.55$), SCshape (green, $\phi = 0.65$), and combined shape (purple, with BCC box at $\phi = 0.55$ and SC box at $\phi = 0.65$). C Heat map for the shape distribution for the optimal FCC shape (red, $\phi = 0.55$), BCC shape (blue, $\phi = 0.65$), and combined shape (purple, with FCC box at $\phi = 0.55$ and BCC box at $\phi = 0.65$). D Heat map for the shape distribution for the optimal FCC shape (red, $\phi = 0.55$), BCC shape (blue, $\phi = 0.60$), and combined shape (purple, with FCC box at $\phi = 0.55$) and BCC box at $\phi = 0.60$). Reproduced from manuscript [20].
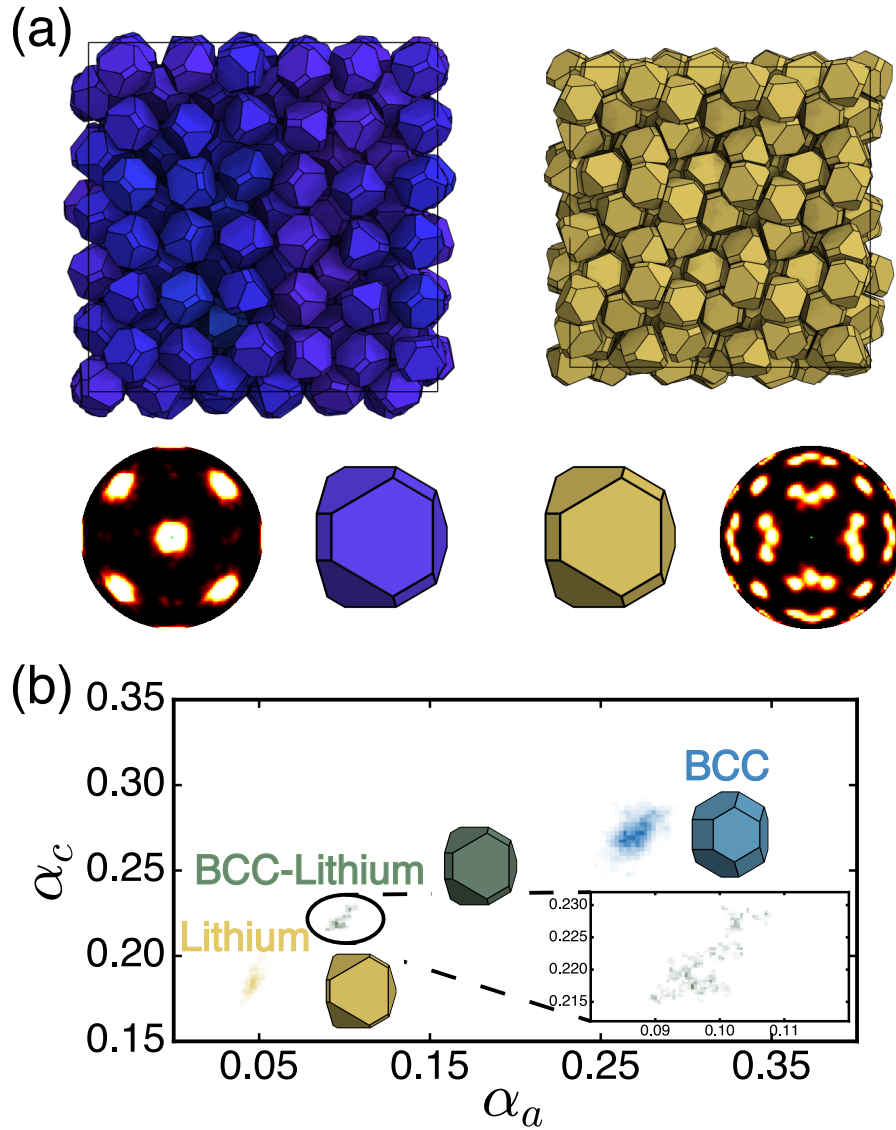
Figure 6.6: A Snapshots of the simulation setup: two simulation boxes of structure types BCC (blue, $\phi = 0.55$) and Li (yellow, $\phi = 0.70$), the bond-orientational order diagrams indicating the structures, and magnified particles to depict their (identical) shape. B Heat map for the shape distribution for the optimal BCC shape (blue, $\phi = 0.55$), Li shape (yellow, $\phi = 0.70$), and combined shape (teal, with BCC box at $\phi = 0.55$ and Li box at $\phi = 0.70$). Reproduced from manuscript [20].
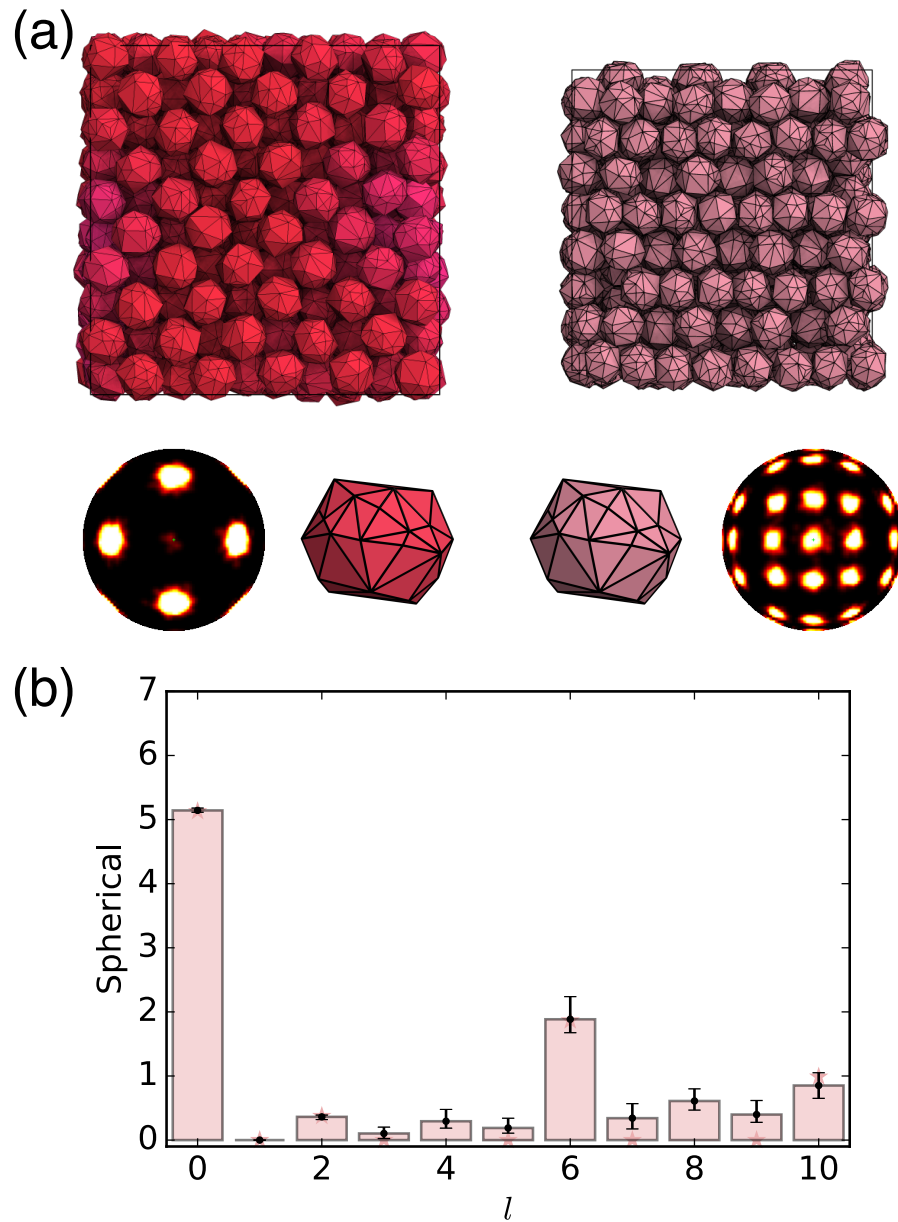
Figure 6.7: A Snapshots of the simulation setup: two simulation boxes of structure types FCC (red, $\phi = 0.55$) and β-W (pink, $\phi = 0.65$), the bond-orientational order diagrams indicating the structures, and magnified particles to depict their (identical) shape. B S_l analysis for optimal shapes of phase transition FCC$\leftrightarrow\beta$-W where the two densities are $\phi_1 = 0.65$ and $\phi_2 = 0.55$. Reproduced from manuscript [20].
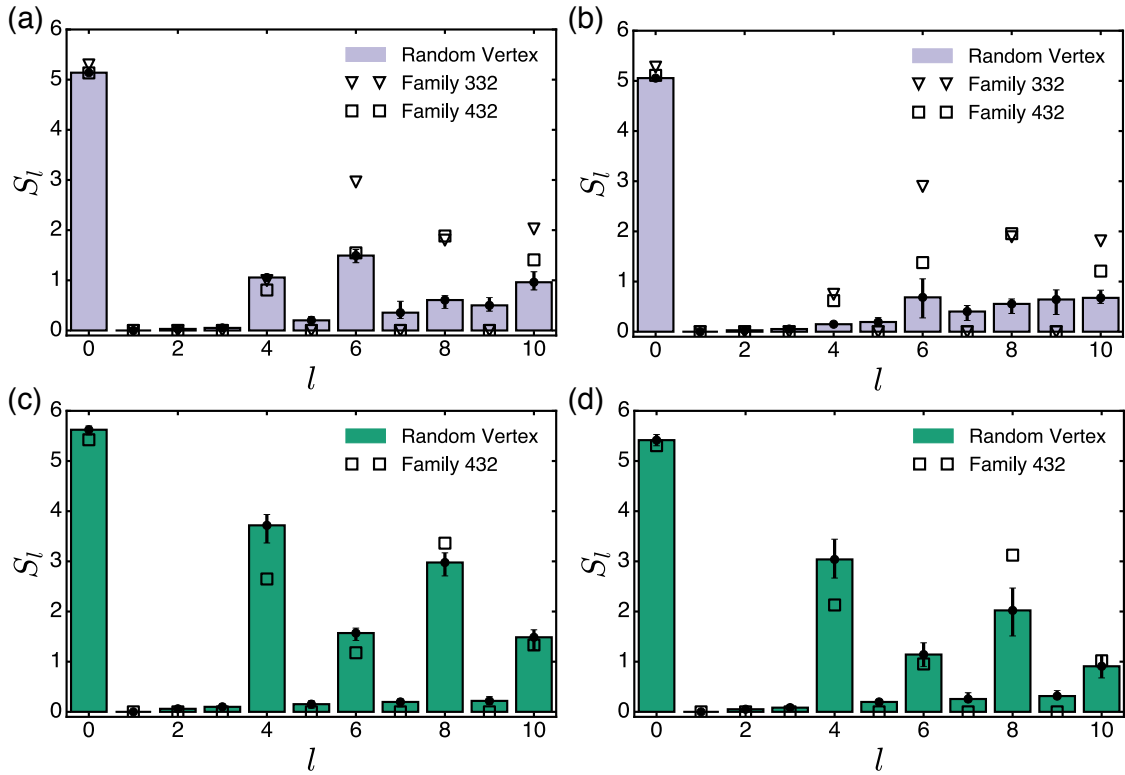
Figure 6.8: S_l analysis for optimal shapes of different phase transitions and at various densities ϕ_1 and ϕ_2: A FCC→BCC transition at $\phi_1 = 0.65$ and $\phi_2 = 0.55$; B FCC→BCC transition at $\phi_1 = 0.60$ and $\phi_2 = 0.55$; C BCC→SC transition at $\phi_1 = 0.70$ and $\phi_2 = 0.55$; D BCC→SC transition at $\phi_1 = 0.65$ and $\phi_2 = 0.55$. Reproduced from manuscript [20].
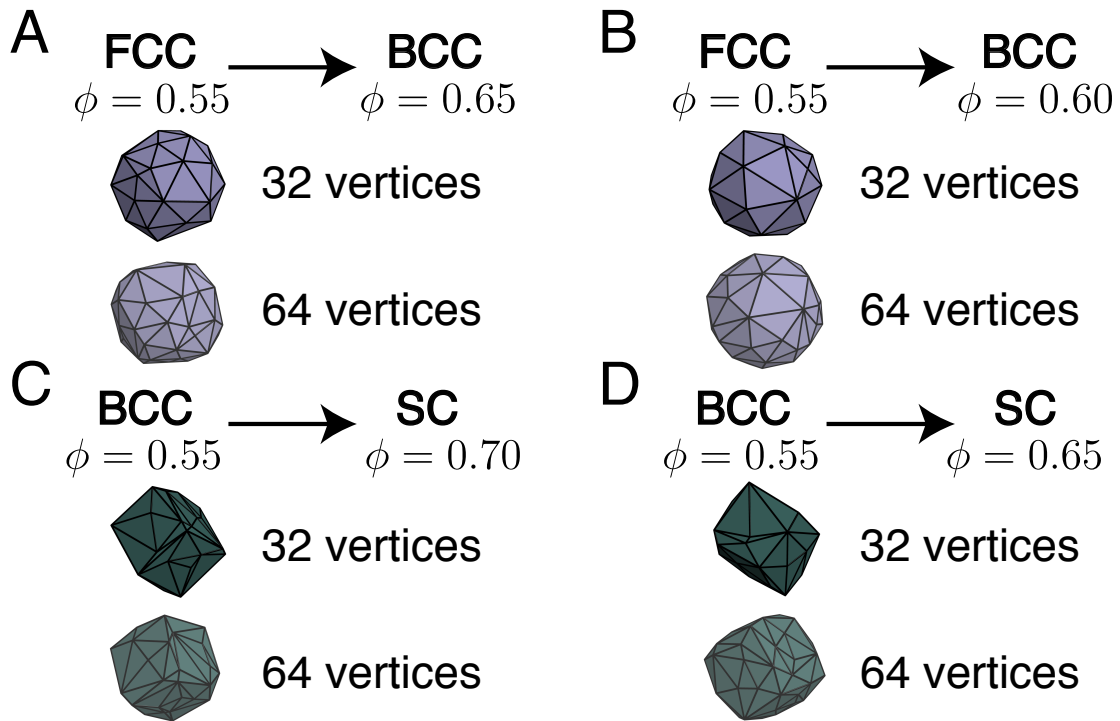
Figure 6.9: A Example shapes obtained from fixed vertex number simulations of phase transition FCC→BCC transition where the two densities are $\phi_1 = 0.65$ and $\phi_2 = 0.55$, up (32 vertices), down (64 vertices). B Example shapes obtained from fixed vertex number simulations of phase transition FCC→BCC transition where the two densities are $\phi_1 = 0.60$ and $\phi_2 = 0.55$, up (32 vertices), down(64 vertices). C Example shapes obtained from fixed vertex number simulations of phase transition BCC→SC transition where the two densities are $\phi_1 = 0.70$ and $\phi_2 = 0.55$, up (32 vertices), down (64 vertices). D Example shapes obtained from fixed vertex number simulations of phase transition BCC→SC transition where the two densities are $\phi_1 = 0.65$ and $\phi_2 = 0.55$, up (32 vertices), down (64 vertices). Reproduced from manuscript [20].

CHAPTER VII

Conclusion and Outlook

7.1   Summary of Results

In summary, with the four projects presented in Ch. III-VI, we have focused on different aspects of solid–solid phase transitions in colloidal crystals. These studies have shown us that there are many unexplored rich behaviors of solid–solid phase transitions that we can achieve via colloidal matter. Using these building blocks, we are able to construct minimal models to answer questions about the fundamental properties of these phase transitions and posing new questions regards to materials design in the next generation.

In the first study (Ch. III), we lay out the fundamental construct of using shape changing hard particles as a minimal model to study shape driven solid–solid phase transitions. Since our particles are hard, the system is purely entropic, which means we are able to separate out how entropy plays a role in solid–solid phase transitions. We investigate the thermodynamic order of two different phase transitions, FCC↔BCC, and BCC↔SC, within this minimal model and find that one phase transition is discontinuous (first-order) and the other phase transition is continuous (second-order). We also have done a proof of concept study of whether these building blocks can be used for next generation material design. Based on studies of the

transition rate between targeted crystals, these particles show big promise.

In the second study (Ch. IV), we further look into the FCC↔BCC phase transition. This is one of the most common solid–solid phase transitions in nature and is related to many different material manipulation. By the Landau free energy construct, the FCC↔BCC transition can in principle be second order given that there is a common sub-symmetry structure of FCC and BCC, so we want to know whether we could have a second order FCC↔BCC transition in a purely entropic system. We investigate both concave and convex shapes of different particle symmetries and find that all FCC↔BCC transitions are first-order. This study is our first to identify the uniqueness of entropic systems.

In the third study (Ch. V), we carry out $1,000,000$-particle simulations aiming to have detailed analysis of transitions pathways of FCC↔BCC and BCC↔SC transitions. We observe that first there is a qualitative difference between the two transitions, where the pathway of FCC↔BCC is highly system size dependent, while BCC↔SC is the same across different sizes.

In the fourth study (Ch. VI), we explore the possibilities of using inverse design tools to design the optimal building blocks for a target pressure induced solid–solid phase transition. We successfully designed two reversible transitions using four different particle constraints and demonstrated this can be a viable path for smart materials design. However, the method does not work for any given two crystal structures as it only considers the thermodynamics of the systems, not the kinetics.

7.2 Concluding Remarks

With the advancement of colloidal particle synthesis and high performance computation, researchers can probe fundamental properties of materials behaviors that

was not possible before. One theme with my dissertation is trying to see what the extent of purely entropic systems is. Many publications have demonstrated various complexities that a purely entropic system can achieve and many parallels have been drawn towards atomistic systems. But can we use the behaviors of entropic system to infer about the behavior of atomistic systems? This question is still up to debate on a case by case scenario.

With the studies listed above, we have shown that in our specific cases, we can use our systems to provide understandings of how certain phase transitions occur, from both thermodynamic and kinetic behaviors. However, in Ch. VI, we show the limitation of materials design with maximizing entropy in the sense that, for certain phase transitions, even though both phases are thermodynamically favorable at different pressures, there may or may not exist a viable pathway for the transition to happen without melting and recrystallizing.

At the same time, there are still much left to study in entropic systems. In most experimental work, researchers try very hard to reduce polydispersity, and while in simulation work, polydispersity is rarely considered. But interesting questions could arise, starting with what will happen if a system consists of many different shape particles that all self assemble into FCC? Or what will happen if a system consists of half particles that self assemble into BCC and half particles that self assemble into FCC? Will they phase separate or form some combined structures? These are all different dimensions of degree of freedom that have not been considered before.

BIBLIOGRAPHY

BIBLIOGRAPHY

[1] Umang Agarwal and Fernando A. Escobedo. Mesophase behaviour of polyhedral particles. *Nat. Mater.*, 10:230–235, 2011.

[2] Umang Agarwal and Fernando A. Escobedo. Effect of quenched size polydispersity on the ordering transitions of hard polyhedral particles. *J. Chem. Phys.*, 137(2):024905, 2012.

[3] N. Khalid Ahmed, Greg van Anders, Elizabeth R. Chen, and Sharon C. Glotzer. Crossover behavior in the packing and assembly of concave building blocks. *Submitted*, 2015.

[4] Joshua A. Anderson and Sharon C. Glotzer. The Development and Expansion of HOOMD-Blue Through Six Years of GPU Proliferation. 2013. http://codeblue.umich.edu/hoomd-blue.

[5] Joshua A. Anderson, M. Eric Irrgang, and Sharon C. Glotzer. Scalable metropolis monte carlo for simulation of hard shapes. *Computer Physics Communications*, 204:21 – 30, 2016.

[6] Edgar C. Bain and N. Y. Dunkirk. The Nature of Martensite. *Trans. AIME*, 70:25–47, 1924.

[7] A Bojack, L Zhao, PF Morris, and J Sietsma. In-situ determination of austenite and martensite formation in 13cr6ni2mo supermartensitic stainless steel. *Materials Characterization*, 71:77–86, 2012.

[8] MJ Buerger et al. Phase transformations in solids. *John Wiley*, page 183, 1951.

[9] P. C. Burnley and H. W. Green. Stress dependence of the mechanism of the olivine-spinel transformation. *Nature*, 338(6218):753–756, Apr 1989.

[10] Marie T. Casey, Raynaldo T. Scarlett, W. Benjamin Rogers, Ian Jenkins, Talid Sinno, and John C. Crocker. Driving diffusionless transformations in colloidal crystals using dna handshaking. *Nature Communications*, 3(1209), 2012.

[11] Elizabeth R. Chen, Daphne Klotsa, Michael Engel, Pablo F. Damasceno, and Sharon C. Glotzer. Complexity in surfaces of densest packings for families of polyhedra. *Phys. Rev. X*, 4:011024, Feb 2014.

[12] Janosch Cravillon, Roman Nayuk, Sergej Springer, Armin Feldhoff, Klaus Huber, and Michael Wiebcke. Controlling zeolitic imidazolate framework nano- and microcrystal formation: Insight into crystal growth by time-resolved in situ static light scattering. *Chemistry of Materials*, 23(8):2130–2141, 2011.

[13] Pablo F. Damasceno, Michael Engel, and Sharon C. Glotzer. Crystalline Assemblies and Densest Packings of a Family of Truncated Tetrahedra and the Role of Directional Entropic Forces. *ACS Nano*, 6(1):609–614, 2012.

[14] Pablo F. Damasceno, Michael Engel, and Sharon C. Glotzer. Predictive Self-Assembly of Polyhedra into Complex Structures. *Science*, 337(6093):453–457, 2012.

[15] Pablo F Damasceno, Andrew S Karas, Benjamin A Schultz, Michael Engel, and Sharon C Glotzer. Controlling chirality of entropic crystals. *Physical review letters*, 115(15):158303, 2015.

[16] Joost de Graaf, Laura Filion, Matthieu Marechal, René van Roij, and Marjolein Dijkstra. Crystal-structure prediction via the floppy-box monte carlo algorithm: Method and application to hard (non)convex particles. *J. Chem. Phys.*, 137(21), 2012.

[17] Joost de Graaf, René van Roij, and Marjolein Dijkstra. Dense regular packings of irregular nonconvex particles. *Phys. Rev. Lett.*, 107:155501, Oct 2011.

[18] Anthony Désert, Céline Hubert, Zheng Fu, Lucie Moulet, Jérôme Majimel, Philippe Barboteau, Antoine Thill, Muriel Lansalot, Elodie Bourgeat-Lami, Etienne Duguet, and Serge Ravaine. Synthesis and site-specific functionalization of tetravalent, hexavalent, and dodecavalent silica particles. *Angew. Chem., Int. Ed.*, 52:11068–11072, 2013.

[19] Chrisy Xiyu Du, Greg van Anders, Joshua A. Anderson, and Sharon C. Glotzer. Kinetics of shape driven colloidal solid–solid transitions. *in preparation*, 2018.

[20] Chrisy Xiyu Du, Greg van Anders, Julia Dshemuchadse, Paul M. Dodd, and Sharon C. Glotzer. Inverse design of pressure-induced solid–solid transitions in colloids. *in preparation*, 2018.

[21] Chrisy Xiyu Du, Greg van Anders, Richmond S. Newman, and Sharon C. Glotzer. Shape-driven colloidal crystal–crystal transitions. *Proc. Natl. Acad. Sci. U.S.A.*, 114:E3892–E3899, 2017.

[22] Bradley Efron. Nonparametric estimates of standard error: The jackknife, the bootstrap and other methods. *Biometrika*, 68(3):589–599, 1981.

[23] R. Eppenga and D. Frenkel. Monte carlo study of the isotropic and nematic phases of infinitely thin hard platelets. *Molecular Physics*, 52:1303–1334, 1984.

[24] Kristen A. Fichthorn and W. H. Weinberg. Theoretical foundations of dynamical monte carlo simulations. *J. Chem. Phys.*, 95(2):1090–1096, 1991.

[25] B. Fultz. *Phase Transitions in Materials*. Cambridge University Press, 2014.

[26] Oleg Gang and Yugang Zhang. Shaping phases by phasing shapes. *ACS Nano*, 5(11):8459–8465, 2011.

[27] Anjan P. Gantapara, Joost de Graaf, René van Roij, and Marjolein Dijkstra. Phase diagram and structural diversity of a family of truncated cubes: Degenerate close-packed structures and vacancy-rich states. *Phys. Rev. Lett.*, 111:015501, Jul 2013.

[28] Yina Geng, Greg van Anders, Paul M. Dodd, Julia Dshemuchadse, and Sharon C. Glotzer. Engineering entropy for the inverse design of colloidal crystals from hard shapes. 2017.

[29] Sharon C. Glotzer and Michael J. Solomon. Anisotropy of building blocks and their assembly into complex structures. *Nat. Mater.*, 6(8):557–562, 2007.

[30] Nigel Goldenfeld. *Lectures on phase transitions and the renormalization group*. Addison-Wesley, Reading MA, 1992.

[31] Jianxiao Gong, Richmond S. Newman, Michael Engel, Man Zhao, Fenggang Bian, Sharon C. Glotzer, and Zhiyong Tang. Shape-dependent ordering of gold nanocrystals into large-scale superlattices. *Nat. Commun.*, 8:14038, 2017.

[32] Alan H Guth. Inflationary universe: A possible solution to the horizon and flatness problems. *Physical Review D*, 23(2):347, 1981.

[33] Amir Haji-Akbari, Michael Engel, Aaron S. Keys, Xiaoyu Zheng, Rolfe G. Petschek, Peter Palffy-Muhoray, and Sharon C. Glotzer. Disordered, Quasicrystalline and Crystalline Phases of Densely Packed Tetrahedra. *Nature*, 462:773–777, 2009.

[34] Joel Henzie, Michael Grünwald, Asaph Widmer-Cooper, Phillip L. Geissler, and Peidong Yang. Self-assembly of uniform polyhedral silver nanocrystals into densest packings and exotic superlattices. *Nat. Mater.*, 11:131–137, 2012.

[35] Samantha J. Ivell, Roel P. A. Dullens, Stefano Sacanna, and Dirk G. A. L. Aarts. Emerging structural disorder in a suspension of uniformly dimpled colloidal particles. *Soft Matter*, 9:9361–9365, 2013.

[36] E. T. Jaynes. Information theory and statistical mechanics. *Phys. Rev.*, 106:620–630, May 1957.

[37] Leo P Kadanoff. Scaling and universality in statistical physics. *Physica A: Statistical Mechanics and its Applications*, 163(1):1–14, 1990.

[38] Andrew S Karas, Jens Glaser, and Sharon C Glotzer. Using depletion to control colloidal crystal assemblies of hard cuboctahedra. *Soft matter*, 12(23):5199–5204, 2016.

[39] Larry Kaufman and Morris Cohen. Thermodynamics and kinetics of martensitic transformations. *Progress in Metal Physics*, 7:165–246, 1958.

[40] Stephen H. Kirby, William B. Durham, and Laura A. Stern. Mantle phase changes and deep-earthquake faulting in subducting lithosphere. *Science*, 252(5003):216–225, 1991.

[41] Daphne Klotsa, Elizabeth R. Chen, Michael Engel, Pablo F. Damasceno, and Sharon C. Glotzer. To appear. *In preparation*, 2018.

[42] DP Koistinen and RE Marburger. A general equation prescribing the extent of the austenite-martensite transformation in pure iron-carbon alloys and plain carbon steels. *acta metallurgica*, 7(1):59–60, 1959.

[43] Shankar Kumar, John M Rosenberg, Djamal Bouzida, Robert H Swendsen, and Peter A Kollman. The weighted histogram analysis method for free-energy calculations on biomolecules. i. the method. *J. Comput. Chem.*, 13(8):1011–1021, 1992.

[44] Wolfgang Lechner and Christoph Dellago. Accurate determination of crystal structures based on averaged local bond order parameters. *J. Chem. Phys.*, 129(11), 2008.

[45] Kyung Jin Lee, Jaewon Yoon, Sahar Rahmani, Sangyeul Hwang, Srijanani Bhaskar, Samir Mitragotri, and Joerg Lahann. Spontaneous shape reconfigurations in multicompartmental microcylinders. *Proc. Natl. Acad. Sci. U.S.A.*, 109(40):16057–16062, 2012.

[46] Ruipeng Li, Kaifu Bian, Yuxuan Wang, Hongwu Xu, Jennifer A. Hollingsworth, Tobias Hanrath, Jiye Fang, and Zhongwu Wang. An obtuse rhombohedral superlattice assembled by pt nanocubes. *Nano Letters*, 15(9):6254–6260, 2015.

[47] Andrei D Linde. A new inflationary universe scenario: a possible solution of the horizon, flatness, homogeneity, isotropy and primordial monopole problems. *Physics Letters B*, 108(6):389–393, 1982.

[48] Peter J. Lu and David A. Weitz. Colloidal particles: Crystals, glasses, and gels. *Annual Review of Condensed Matter Physics*, 4(1):217–233, 2013.

[49] Vera Meester, Ruben W. Verweij, Casper van der Wel, and Daniela J. Kraft. Colloidal recycling: Reconfiguration of random aggregates into patchy particles. *ACS Nano*, 10(4):4322–4329, 2016.

[50] Janne-Mieke Meijer, Antara Pal, Samia Ouhajji, Henk N. W. Lekkerkerker, Albert P. Philipse, and Andrei V. Petukhov. Observation of solid-solid transitions in 3d crystals of colloidal superballs. *Nature Communications*, 8(14352), 2017.

[51] Janne-Mieke Meijer, Antara Pal, Samia Ouhajji, Henk N.W. Lekkerkerker, Albert P. Philipse, and Andrei V. Petukhov. Observation of solidsolid transitions in 3d crystals of colloidal superballs. *Nat. Commun.*, 8:14352, 2017.

[52] N. Metropolis, A. W. Rosenbluth, M. N. Rosenbluth, A. H. Teller, and E. Teller. Equation of State Calculations by Fast Computing Machines. *J. Chem. Phys.*, 21:1087–1092, 1953.

[53] Jaime A. Millan, Daniel Ortiz, Greg van Anders, and Sharon C. Glotzer. Self-assembly of archimedean tilings with enthalpically and entropically patchy polygons. *ACS Nano*, 8(3):2918–2928, 2014.

[54] Priti S. Mohanty, Payam Bagheri, Sofi Nöjd, Anand Yethiraj, and Peter Schurtenberger. Multiple path-dependent routes for phase-transition kinetics in thermoresponsive and field-responsive ultrasoft colloids. *Phys. Rev. X*, 5:011030, Mar 2015.

[55] Motohiko Murakami, Kei Hirose, Katsuyuki Kawamura, Nagayoshi Sata, and Yasuo Ohishi. Post-perovskite phase transition in mgsio3. *Science*, 304(5672):855–858, 2004.

[56] Ran Ni, Anjan Prasad Gantapara, Joost de Graaf, Rene van Roij, and Marjolein Dijkstra. Phase diagram of colloidal hard superballs: from cubes via spheres to octahedra. *Soft Matter*, 8:8826–8834, 2012.

[57] G. Odriozola, F. Jimenez-Angeles, and M. Lozada-Cassou. Entropy driven key-lock assembly. *J. Chem. Phys.*, 129(11):111101, 2008.

[58] Gerardo Odriozola and Marcelo Lozada-Cassou. Statistical mechanics approach to lock-key supramolecular chemistry interactions. *Phys. Rev. Lett.*, 110:105701, Mar 2013.

[59] GB Olson and Morris Cohen. Kinetics of strain-induced martensitic nucleation. *Metallurgical transactions A*, 6(4):791, 1975.

[60] Maolin Pang, Amy J. Cairns, Yunling Liu, Youssef Belmabkhout, Hua Chun Zeng, and Mohamed Eddaoudi. Highly monodisperse miii-based soc-mofs (m = in and ga) with cubic and truncated cubic morphologies. *Journal of the American Chemical Society*, 134(32):13176–13179, 2012. PMID: 22812681.

[61] Yi Peng, Feng Wang, Ziren Wang, Ahmed M. Alsayed, Zexin Zhang, Arjun G. Yodh, and Yilong Han. Two-step nucleation mechanism in solid–solid phase transitions. *Nat Mater*, 14:101–108, 2015.

[62] Francisco-José Pérez-Reche, Marcelo Stipcich, Eduard Vives, Lluís Mañõsa, Antoni Planes, and Michel Morin. Kinetics of martensitic transitions in cu-al-mn under thermal cycling: Analysis at multiple length scales. *Physical Review B*, 69(6):064101, 2004.

[63] David A. Porter. *Phase Transformations in Metals and Alloys*. CRC Press, Florida, 3rd edition, 2009.

[64] Weikai Qi, Yi Peng, Yilong Han, Richard K. Bowles, and Marjolein Dijkstra. Nonclassical nucleation in a solid-solid transition of confined hard spheres. *Phys. Rev. Lett.*, 115:185701, Oct 2015.

[65] Weikai Qi, Yi Peng, Yilong Han, Richard K. Bowles, and Marjolein Dijkstra. Nonclassical nucleation in a solid-solid transition of confined hard spheres. *Phys. Rev. Lett.*, 115:185701, Oct 2015.

[66] Laura Rossi, Stefano Sacanna, William T. M. Irvine, Paul M. Chaikin, David J. Pine, and Albert P. Philipse. Cubic crystals from cubic colloids. *Soft Matter*, 7:4139–4142, 2011.

[67] Laura Rossi, Vishal Soni, Douglas J. Ashton, David J. Pine, Albert P. Philipse, Paul M. Chaikin, Marjolein Dijkstra, Stefano Sacanna, and William T. M. Irvine. Shape-sensitive crystallization in colloidal superball fluids. *Proc. Natl. Acad. Sci. U.S.A.*, 112(17):5286–5290, 2015.

[68] S. Sacanna, W. T. M. Irvine, P. M. Chaikin, and D.J. Pine. Lock and key colloids. *Nature*, 464:575–578, 2010.

[69] Stefano Sacanna, Mark Korpics, Kelvin Rodriguez, Laura Colon-Melendez, Seung-Hyun Kim, David J. Pine, and Gi-Ra Yi. Shaping colloids for self-assembly. *Nat. Commun.*, 4:1688, 2013.

[70] Sampa Saha, Davor Copic, Srijanani Bhaskar, Nicholas Clay, Alessandro Donini, A. John Hart, and Joerg Lahann. Chemically controlled bending of compositionally anisotropic microcylinders. *Angew. Chem., Int. Ed.*, 51(3):660–665, 2012.

[71] Luis Sandoval and Herbert M. Urbassek. Transformation pathways in the solid-solid phase transitions of iron nanowires. *Applied Physics Letters*, 95(19):191909, 2009.

[72] Luis Sandoval, Herbert M Urbassek, and Peter Entel. The bain versus nishiyamawassermann path in the martensitic transformation of fe. *New Journal of Physics*, 11(10):103027, 2009.

[73] Eduardo Sanz and Chantal Valeriani. Crystal-crystal transitions: Mediated by a liquid. *Nat Mater*, 14:15–16, 2015.

[74] C.E. Shannon. A mathematical theory of communication. *Bell Syst. Tech. J.*, 27:379–423, 623–656, 1948.

[75] SR Shenoy, T Lookman, A Saxena, and AR Bishop. Martensitic textures: Multiscale consequences of elastic compatibility. *Physical Review B*, 60(18):R12537, 1999.

[76] Melinda Sindoro, Nobuhiro Yanai, Ah-Young Jee, and Steve Granick. Colloidal-sized metalorganic frameworks: Synthesis and applications. *Accounts of Chemical Research*, 47(2):459–469, 2014. PMID: 24328052.

[77] William F. Smith. *Principles of materials science and engineering*. McGraw Hill, New York, 3rd edition, 1996.

[78] Alexei A Starobinsky. Dynamics of phase transition in the new inflationary universe scenario and generation of perturbations. *Physics Letters B*, 117(3-4):175–178, 1982.

[79] Paul J. Steinhardt, David R. Nelson, and Marco Ronchetti. Bond-orientational order in liquids and glasses. *Phys. Rev. B*, 28:784–805, Jul 1983.

[80] Nikos Tasios, Anjan Prasad Gantapara, and Marjolein Dijkstra. Glassy dynamics of convex polyhedra. *J. Chem. Phys.*, 141(22), 2014.

[81] Jean-Claude Toledano and Pierre Toledano. *The Landau theory of phase transitions: application to structural, incommensurate, magnetic and liquid crystal systems*, volume 3. World Scientific Publishing Company, 1987.

[82] G.M. Torrie and J.P. Valleau. Nonphysical sampling distributions in monte carlo free-energy estimation: Umbrella sampling. *J. Comp. Phys.*, 23(2):187 – 199, 1977.

[83] Ayako Umemura, Stphane Diring, Shuhei Furukawa, Hiromitsu Uehara, Takaaki Tsuruoka, and Susumu Kitagawa. Morphology design of porous coordination polymer crystals by coordination modulation. *Journal of the American Chemical Society*, 133(39):15506–15513, 2011. PMID: 21861521.

[84] Greg van Anders, N. Khalid Ahmed, Ross Smith, Michael Engel, and Sharon C. Glotzer. Entropically patchy particles: Engineering valence through shape entropy. *ACS Nano*, 8:931–940, 2014.

[85] Greg van Anders, Daphne Klotsa, N. Khalid Ahmed, Michael Engel, and Sharon C. Glotzer. Understanding shape entropy through local dense packing. *Proc. Natl. Acad. Sci. U.S.A.*, 111:E4812–E4821, 2014.

[86] Greg van Anders, Daphne Klotsa, Andrew S. Karas, Paul M. Dodd, and Sharon C. Glotzer. Digital Alchemy for Materials Design: Colloids and Beyond. *ACS Nano*, 9:9542–9553, 2015.

[87] Eduard Vives, Jordi Ortín, Lluís Mañosa, Ismael Ràfols, Ramon Pérez-Magrané, and Antoni Planes. Distributions of avalanches in martensitic transformations. *Physical review letters*, 72(11):1694, 1994.

[88] Duanduan Wan, Chrisy Xiyu Du, Greg van Anders, and Sharon C. Glotzer. FCC↔BCC phase transitions of convex and concave particles. *in preparation*, 2018.

[89] Wei Wang, Mao-Jie Zhang, Rui Xie, Xiao-Jie Ju, Chao Yang, Chuan-Lin Mou, David A. Weitz, and Liang-Yin Chu. Hole–shell microparticles from controllably evolved double emulsions. *Angew. Chem. Int. Ed.*, 52(31):8084–8087, 2013.

[90] Nobuhiro Yanai, Melinda Sindoro, Jing Yan, and Steve Granick. Electric field-induced assembly of monodisperse polyhedral metalorganic framework crystals. *Journal of the American Chemical Society*, 135(1):34–37, 2013. PMID: 23240678.

[91] Hemantha Kumar Yeddu, Vsevolod I Razumovskiy, Annika Borgenstam, Pavel A Korzhavyi, Andrei V Ruban, and John gren. Multi-length scale modeling of martensitic transformations in stainless steels. *Acta Materialia*, 60(19):6508–6517, 2012.

[92] Anand Yethiraj, Alan Wouterse, Benito Groh, and Alfons van Blaaderen. Nature of an electric-field-induced colloidal martensitic transition. *Phys. Rev. Lett.*, 92:058301, Feb 2004.

[93] Kaylie L. Young, Michelle L. Personick, Michael Engel, Pablo F. Damasceno, Stacey N. Barnaby, Reiner Bleher, Tao Li, Sharon C. Glotzer, Byeongdu Lee, and Chad A. Mirkin. A directional entropic force approach to assemble anisotropic nanoparticles into superlattices. *Angew. Chem., Int. Ed.*, 52:13980–13984, 2013.

[94] Mena Youssef, Theodore Hueckel, Gi-Ra Yi, and Stefano Sacanna. Shape-shifting colloids via stimulated dewetting. *Nat Commun*, 7:12216, Jul 2016.

[95] Yugang Zhang, Fang Lu, Daniel van der Lelie, and Oleg Gang. Continuous phase transformation in nanocube assemblies. *Phys. Rev. Lett.*, 107:135701, Sep 2011.

[96] Yugang Zhang, Suchetan Pal, Babji Srinivasan, Thi Vo, Sanat Kumar, and Oleg Gang. Selective transformations between nanoparticle superlattices via the reprogramming of dna-mediated interactions. *Nature Materials*, 14:840–847, 2015.

[97] Jing Zhou, Sara A. Turner, Sarah M. Brosnan, Qiaoxi Li, Jan-Michael Y. Carrillo, Dmytro Nykypanchuk, Oleg Gang, Valerie S. Ashby, Andrey V. Dobrynin, and Sergei S. Sheiko. Shapeshifting: Reversible shape memory in semicrystalline elastomers. *Macromolecules*, 47(5):1768–1776, 2014.